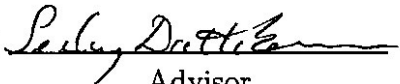# DATA ASSIMILATION FOR IONOSPHERE-THERMOSPHERE STORM-TIME STATE ESTIMATION

BY

DANIEL SVETA MILADINOVICH

Submitted in partial fulfillment of the
requirements for the degree of
Doctor of Philosophy in Mechanical and Aerospace Engineering
in the Graduate College of the
Illinois Institute of Technology

Approved _____
Advisor

Chicago, Illinois
July 2018

# ACKNOWLEDGMENT

# TABLE OF CONTENTS

LIST OF TABLES

LIST OF FIGURES

LIST OF SYMBOLS

| Symbol | Definition |
|---|---|
| $\mathbf{B}_{\text{state}}$ | storm-time state basis function array |
| $\vec{B}$ | basis function mapping matrix |
| $\vec{B}$ | magnetic field |
| $B^2$ | norm-squared of $\vec{B}$ |
| $B^2$ | norm-squared of $\vec{B}$ |
| $D$ | declination angle |
| $\vec{E}$ | electric field |
| $E$ | expectation |
| $\mathbf{H}$ | mapping matrix |
| $\mathbf{H}_N$ | plasma density rate mapping matrix |
| $\mathbf{H}_u$ | neutral wind mapping matrix |
| $\mathbf{H}_{uE}$ | eastward neutral wind mapping matrix |
| $\mathbf{H}_{uN}$ | northward neutral wind mapping matrix |
| $\mathbf{H}_V$ | electric potential mapping matrix |
| $\mathbf{H}_{Vr}$ | radial ion drift to electric potential mapping matrix |
| $\mathbf{H}_{V\theta}$ | colatitudinal ion drift to electric potential mapping matrix |
| $\mathbf{H}_{V\phi}$ | longitudinal potential mapping matrix |
| $I$ | inclination angle |
| $\mathbf{I}$ | identity matrix |
| $J$ | cost functional |
| $\mathbf{K}$ | Kalman gain |

| | |
|---|---|
| $L$ | geomagnetic L-shell |
| $N$ | plasma density |
| $N_l^m$ | Legendre normalization constant |
| $\mathbf{P}$ | state estimate covariance matrix |
| $\mathbf{P}^-$ | forecast state estimate covariance matrix |
| $\mathbf{P}_{l(\cdot)}^m$ | derivative of Legendre polynomial wrt $(\cdot)$ |
| $\mathbf{Q}$ | process covariance matrix |
| $\mathbf{R}$ | observation covariance matrix |
| $\mathbf{R}_N$ | plasma density rate observation covariance matrix |
| $\mathbf{R}_a$ | model covariance matrix |
| $\mathbf{R}_{a\vec{v}}$ | ion drift model covariance matrix |
| $\mathbf{R}_{a\mathbf{x}_V}$ | electric potential coefficient model covariance matrix |
| $\mathbf{R}_u$ | FPI LOS neutral wind observation covariance matrix |
| $\mathbf{R}_{a,u_E}$ | eastern neutral wind model covariance matrix |
| $\mathbf{R}_{a,u_N}$ | northern neutral wind model covariance matrix |
| $\mathbf{R}_{a,x_{uE}}$ | eastern neutral wind coefficient model covariance matrix |
| $\mathbf{R}_{a,x_{uN}}$ | eastern neutral wind coefficient model covariance matrix |
| $R$ | distance to the center of Earth |
| $R_e$ | Earth's average radius |
| $R_{eq}$ | Earth's equatorial radius |
| $V$ | electric potential |
| $V_{(\cdot)}$ | derivative electric potential with respect to a variable $(\cdot)$ |

| | |
|---|---|
| $a$ | model |
| $az$ | azimuth |
| $a_L$ | loss model |
| $a_N$ | plasma density rate model |
| $a_P$ | production model |
| $a_\phi$ | longitudinal driver mapping term |
| $a_R$ | radial driver mapping term |
| $a_\theta$ | colatitudinal driver mapping term |
| $a_{exb}$ | perpendicular transport model |
| $a_\parallel$ | parallel transport model |
| $a_\phi$ | longitudinal driver mapping term |
| $\mathbf{a}_{\text{state}}$ | state estimate array |
| $b_\phi$ | longitudinal driver basis function mapping term |
| $b_R$ | radial electric driver basis function mapping term |
| $b_\theta$ | colatitudinal driver basis function mapping term |
| $\hat{b}$ | magnetic field direction unit vector |
| $c$ | scaling constant |
| $e^-$ | Kalman filter error |
| $\hat{e}_g$ | geodetic east unit vector |
| $\hat{e}_{gm}$ | geomagnetic east unit vector |
| $el$ | elevation |
| $k$ | power series degree for the radial direction |

| | |
|---|---|
| $\hat{k}$ | FPI LOS direction unit vector |
| $l$ | Legendre polynomial band class or power series degree for colatitudinal direction |
| $\ell$ | Legendre polynomial independent variable |
| $m$ | Legendre polynomial degree |
| $\hat{n}_g$ | geodetic east unit vector |
| $\hat{n}_{gm}$ | geomagnetic east unit vector |
| $p$ | power series degree for the longitudinal direction |
| $r$ | altitude above Earth's surface |
| $s_P$ | production source term |
| $s_L$ | loss source term |
| $t$ | time |
| $\vec{u}$ | neutral wind |
| $u_{LOS}$ | line of sight neutral wind |
| $\mathbf{v}$ | measurement bias |
| $\mathbf{v}_u$ | neutral wind measurement bias |
| $\vec{v}$ | ion drift |
| $\vec{v}_D$ | magnetic field parallel diffusion drift |
| $\vec{v}_g$ | magnetic field parallel gravity drift |
| $\vec{v}_\perp$ | perpendicular ion drift |
| $\vec{v}_\parallel$ | perpendicular ion drift |
| $\mathbf{w}$ | process noise |
| $\mathbf{x}$ | true state vector |

| | |
|---|---|
| $\hat{\mathbf{x}}$ | state vector |
| $\hat{\mathbf{x}}^-$ | forecast state vector |
| $\hat{\mathbf{x}}_c^{lm}$ | scalar spherical harmonic cosine coefficient array |
| $\hat{\mathbf{x}}_s^{lm}$ | scalar spherical harmonic sine coefficient array |
| $\hat{\mathbf{x}}_{\text{storm}}$ | storm-time state estimate array |
| $\hat{\mathbf{x}}_{\text{state}}$ | state estimate array |
| $\mathbf{x}_{uN}$ | northward neutral wind state vector |
| $\mathbf{x}_{uE}$ | eastward neutral wind state vector |
| $\mathbf{x}_V$ | electric potential basis function coefficients |
| $\mathbf{x}_{\parallel}$ | parallel neutral wind state vector |
| $y$ | measurement |
| $y_u$ | FPI LOS measurement |
| $\mathbf{z}$ | observations |
| $\mathbf{\Phi}_l^m$ | harmonic function |
| $\mathbf{\Phi}_{l(\cdot)}^m$ | derivative of a harmonic function with respect to a variable |
| $\delta a$ | model correction |
| $\delta a_{uE}$ | geodetic eastward neutral wind transport correction |
| $\delta a_{uN}$ | geodetic northward neutral wind transport correction |
| $\delta a_{exb}$ | perpendicular transport correction |
| $\delta u_E$ | geodetic eastward neutral wind correction |
| $\delta u_N$ | geodetic northward neutral wind correction |
| $\delta\vec{E}$ | electric field correction |

| | |
|---|---|
| $\delta V$ | electric potential correction |
| $\vec{\nabla}$ | gradient operator |
| $\phi$ | longitude |
| $\sigma$ | standard deviation |
| $\tau$ | relaxation time constant |
| $\theta$ | colatitude |
| $\dagger$ | Moore-Penrose pseudoinverse |
| CTIP | Coupled Thermosphere/Ionosphere Plasmasphere |
| EMPIRE | Estimating Model Parameters from Ionospheric Reverse Engineering |
| FPI | Fabry-Perot Interferometer |
| HWM14 | Horizontal Wind Model 2014 |
| IDA4D | Ionospheric Data Assimilation 4 Dimensional |
| IGRF-11 | International Geomagnetic Reference Field-11th Generation |
| IRI | International Reference Ionosphere |
| NRLMSIS | Naval Research Laboratory Mass Spectrometer Incoherent Scatter |
| LOS | Line of Sight |
| MHO | Millstone Hill Observatory |
| TEC | Total Electron Content |
| wrt | with respect to |

# ABSTRACT

This dissertation presents a data assimilation method for estimating the physical drivers of the Earth's ionosphere layer through the combination of Global Navigation Satellite System based (GNSS) ionospheric density measurements, Fabry-Perot interferometer (FPI) neutral wind measurements and several empirical models. The main contributions include 1) Kalman filtering for multi-observation ingestion and multi-state estimation, 2) Ingestion of FPI neutral wind measurements, 3) Spherical harmonic basis functions for global electric potential estimation and 4) a study of storm-time ion drifts using globally ingested data.

The thermosphere is a region of Earth's atmosphere (80-1000km) that contains a balance of and solar ionizing radiation such that an ionosphere can form. During geomagnetic storm events, the ionosphere can be disturbed causing abrupt redistribution of the ionospheric plasma. These disruptions can cause blackouts for radio wave and navigation systems. Understanding what causes the ionosphere to change is therefore necessary as society becomes more dependent on navigation and communication technologies.

The first step in understanding the ionosphere is to quantify its physical drivers. Measurements of the ionosphere are limited both spatially and temporally because the region is so vast. Models, on the other hand, provide our best understanding and capability to simulate the ionosphere and its drivers but often fall short in capturing certain phenomena during severe geomagnetic storms. In this work, a data assimilation algorithm called Estimating Model Parameters for Ionospheric Reverse Engineering (EMPIRE) is further developed to combine both measurements and simulation data sets for estimating ionospheric drivers globally. EMPIRE ingests ionosphere plasma density rate measurements and subtracts model simulation results to produce an observation of the difference between measurements and simulation.

EMPIRE then fits basis functions which represent physical drivers by estimating the function's coefficients. The mapping from observation to physical driver happens using the ion continuity governing equation as a model.

The EMPIRE algorithm was originally developed in 2009 to do regional data assimilation and used only plasma density measurements. In this work, EMPIRE is modified to use a Kalman filter so measurements and models can be ingested in an efficient and systematic manner. Then using the new Kalman filtering method, FPI neutral wind measurements are ingested to provide direct information of an ionospheric driver. This thesis demonstrates the first ever use of FPIs and plasma density measurements in a data assimilative environment. Next, EMPIRE is modified to estimate coefficients to spherical harmonic basis functions rather than power series basis functions. Spherical harmonic functions allow EMPIRE to provide global estimates because they are continuous and orthogonal on a spherical domain (such as Earth). A study is then conducted to ingest global plasma density rate measurements and neutral winds to estimate ion drifts across the globe.

CHAPTER 1

INTRODUCTION

Civilization today depends on technology that operates within the space environment. Since 1983 the Space Foundation has shown that the world is investing in space technology at an increasing rate [6]. Infrastructure such as the International Space Station [7], Global Navigation Satellite Systems (GNSS), and electrical power grids which supply power to cities are just a few of the government and commercial technologies which must be engineered to withstand space weather. The U.S. government has recognized space weather as a national safety threat and formed the Space Weather Operations, Research, and Mitigation (SWORM) Subcommittee of the Committee on Environment, Natural Resources, and Sustainability (CENRS). SWORM is responsible for coordinating between various federal agencies to meet the goals laid out in the National Space Weather Action Plan (SWAP) and National Space Weather Strategy (SWS) [8, 9]. These two documents outline the U.S. government's plan to understand and manage the risks associated with space weather. Goal 5 of that document highlights the need to be able to understand and forecast space weather on which this dissertation focuses its efforts.

Space weather is dominated by our solar system's star, the Sun. The Sun's output includes intermittent coronal mass ejections (CME) and flares which can disturb space from the surface of the Sun to Earth and beyond. At the altitudes from 80 to 1000 km above Earth's surface is a region called the ionosphere-thermosphere (IT). This region of the near-Earth space environment is dominated by the combination of low density atmosphere, electromagnetic radiation, the solar wind and Earth's magnetic field. Low-Earth-orbit satellites occupy the IT region and therefore must be designed to withstand temperatures, radiation and drag present there. Also, nat-

ural and artificial signals can be reflected, attenuated or produced by the IT region, thereby establishing design criteria for communication systems that interact with this region. Particularly, with high precision applications such as GNSS, a knowledge of the IT's state is crucial. This dissertation makes contributions to both the capability of estimating the IT state during geomagnetic storm-time, and to the understanding of the natural processes that belong to the IT region.

## 1.1 Observing and Studying the Ionosphere-Thermosphere Region

The IT region is vast and spans the entire globe making observations for model validation and engineering decisions a challenge. Energy, mass and momentum are transferred into and out of the IT region through its lower and upper boundaries. The lower boundary (80km) is known as the top of the mesosphere and the upper boundary (1000km) is the plasmasphere. The most common way of measuring the IT region is with remote sensing methods (e.g., active and passive)[10, 11, 12] because in situ measurements are very expensive due to the high altitude and coverage required. This dissertation seeks to further enhance observability of the IT region by leveraging data assimilation methods to make the most out of the measured data sets available.

The challenges with obtaining observables of the IT region creates a unique demand for modelers and applied mathematicians to make the most of the data sets that are available. Models of the IT region fall under two different categories, first principle models and empirical techniques. First principle models define the governing equations of the IT region, numerical methods used to solve them, a grid, and the boundary conditions. The solution is then propagated from the boundary conditions throughout the entire IT region, making global simulations time-consuming and resource- intensive. First principle models are, however, necessary demonstrations of scientific understanding of the physics that govern a region as well as the

numerical methods that allow the implementation of governing equation. Conversely, empirical models define a set of basis functions which will be 'fit' to a data set using a minimization technique. Empirical models may contain basis functions which can be solutions to the governing equations (i.e., spherical harmonics for electrostatic potential), thereby more accurately representing the property of interest, or simply be an easy-to-use series. The advantage here is that the solution need not be solved at every location but rather the coefficients to a function which spans the space and time. The disadvantage is that the empirical model's solution is only as good as the data to which it is being fit. With the IT region having sparse data sets, obtaining enough high quality data can be challenging. This dissertation proposes a method that combines first principle physics with empirical modeling to produce global data sets for the first time.

Data assimilation techniques have been in development for the last few decades but typically do not self-consistently estimate external drivers such as neutral winds, electric fields, temperatures as well as the electron densities. Algorithms have been developed with the goal to both image and forecast the Earth's upper atmosphere during geomagnetic storms (solar active, Sa) and quiet time (solar quiet, Sq). The Utah State University (USU) has been developing the Global Assimilation of the Ionospheric Measurements (USU-GAIM) model, the University of Southern California (USC) and the Jet Propulsion Laboratory (JPL) have been developing the Global Assimilative Ionospheric Model (USC/JPL-GAIM) [13, and references therein]. These algorithms assimilate measurements from instrumentation that provides plasma specification (i.e., density, composition and altitude), and they also assimilate climate models that provide other physical drivers of the system. While these algorithms do significantly improve the imaging of ionospheric plasma they fall short in capturing the other IT states that are important for forecasting it. Estimating Model Parameters from Ionospheric Reverse Engineering (EMPIRE) is an algorithm that focuses on

improving storm time estimates of the physical drivers of the plasma and, by doing so, provides important next steps toward a forecastable IT system.

Previously, EMPIRE was derived using a weighted least squares solution with the weighting based on the square distance and the maximum values [14]. Modeling errors, grid interpolation errors and numerical differencing errors were reduced by adding the maximum value weights. Later, a singular value decomposition step was added and the weighting matrix instead based on covariances specified by IDA4D [15]. Prior to this work, EMPIRE was then modified to take in high resolution electron density specification from IDA4D to study high density gradients [16]. While EMPIRE did use covariances in its estimates, it left each time step very different from the next and left the solutions without the ability to propagate error through the estimate. A way to solve this is the use of Kalman filtering methods (see Section 2.2.1) and is one key motivation of my doctoral dissertation.

This dissertation describes the continued development of the EMPIRE algorithm for improved geomagnetic storm-time state estimation of physical drivers of Earth's IT region. The EMPIRE algorithm falls under a category of data assimilation algorithms that combines climate models with instrument measurements. In order to blend the model outputs (aka simulation results) and measurements, the EMPIRE algorithm uses the ion continuity equation as the governing equation. The ion continuity equation is a model of the drivers which determine the rate of ionization of the atmosphere between 80-1000km. The rate of change of ionization is represented by the change in the number density of electrons, which is modeled as having two distinct terms: source terms and divergence terms. Source terms describe a rate of change occurring at a location due to creation or loss of the substance (e.g., plasma). In the case of the ionosphere, source terms can be recombination (a negative density change) or photoionization (a positive density change) due to the Sun's

electromagnetic radiation. The second part of the ion continuity equation is the divergence term that drives the rate of change of density due to flow into and out of a region. A velocity field describing flow in and out of a region is a 3-D vector field. If the coordinate system is chosen to be aligned with a magnetic field, plasma motion perpendicular to the field is dominated by the electric and magnetic field, and motion parallel to the magnetic field is driven by collisional drag, gravity and diffusion. With the ion continuity equation it is possible to relate observable measurement of one parameter of the ion continuity equation to another parameter such as the the electric field or electric potential. More details on the physics within the ionosphere and the ion continuity equation will be described in Sections 2.1.2 to 2.1.3. EMPIRE accomplishes storm-time estimation by prescribing a basis function to a given parameter and rather than estimating the parameter directly at a given location, it estimates a basis function that described that parameter over all space. All of these methods are necessary to be able to make the best possible use of a limited dataset to study the IT region of Earth's near space environment. Details on the the EMPIRE algorithm will be described in Section 2.2.2.

## 1.2 Contributions

This dissertation demonstrates the use of an algorithm for assimilating measurements and models for studying the Ionosphere-Thermosphere (IT) region of Earth. Particularly, the algorithm makes use of Global Navigation Satellite System (GNSS) ionospheric plasma density measurements and Fabry-Perot interferometer measurements for updating background models of the IT region. Chapter 2 contains two background sections that will introduce the material necessary to understand the contributions this dissertation provides. The first Section 2.1 introduces the ionosphere-thermosphere by defining both of them and describing physics present in each 'sphere' (Subsections 2.1.2 and 2.1.1, respectively), and how the two are coupled (Subsection

2.1.3). The second background section, Section 2.2, describes what is meant by data assimilation in the context of this work, Subsection 2.1.2 introduces basic Kalman filter theory and the final subsection, 2.2.2, describes the philosophy behind the EMPIRE algorithm. There are a total of four contributions that are described in the subsequent Chapters:

**1.2.1 Kalman Filtering for Regional IT Storm-Time Estimation.** Chapter 3 describes how a Kalman filter was adapted for use within the EMPIRE algorithm. All relevant components to a Kalman filter are established in background subsection 2.1.2 and then adapted for the EMPIRE assimilative environment in this chapter.

**1.2.2 Inclusion of Fabry-Perot Interferometer Neutral Wind Observations.** Chapter 4 augments the EMPIRE algorithm for ingestion of thermospheric neutral wind measurements. A study showing the effects that these measurements have on IT state estimation using the Kalman filter derived in Chapter 3 is conducted for the 24 October 2011 geomagnetic storm. The analysis region is the south western United States. Results show the successful assimilation of both ionospheric and thermospheric data sets for studying a geomagnetic storm, as well as the identification of a physical phenomenon present in neutral wind thermospheric signals.

**1.2.3 Global Storm-Time Electric Potential State Estimation.** Chapter 5 modifies the EMPIRE algorithm for use with spherical harmonic basis functions for global state estimation of the IT region's electric potential. It describes how spherical harmonic basis functions must be modified to fit to electric potential states and the ion continuity equation

**1.2.4 Application of Global Electric Potential State Estimation for the March, 17th 2015 St. Patrick's Day Geomagnetic Storm.** This contribution builds from the work done in contribution three and applies it to study the 17 March

2015 St. Patrick's Day geomagnetic storm. This geomagnetic storm is one of the most well studied recent geomagnetic storms, making it useful to understand how well GNSS plasma density measurements can be used to estimate global ion drifts. In this chapter I present the EMPIRE configuration used to generate results for this geomagnetic storm and compare the results to ISR data provided in literature.

CHAPTER 2

TECHNICAL BACKGROUND

## 2.1 The Ionosphere and Thermosphere

The Earth's atmosphere is divided into layers that are defined by a unique feature or set of features specific to each layer. The Earth's atmosphere layers include the troposphere (0 to 12km), stratosphere (12 to 50 km), mesosphere (50 to 80 km), thermosphere (80 to 600 km) and lastly the exosphere (700 to 10,000 km). The region this study focuses on is the thermosphere, which is characterized by its sharp rise in temperature. More than 99% of the gas in this layer is 'neutral'. The ionized component is referred to as the ionosphere. These two different names (the thermosphere and ionosphere) are used as if two layers exist, however, really the I-T layers occupy the same space. The final defining feature of the thermosphere layer is its significant composition and density change with altitude. Molecular oxygen (i.e., '**O**') exists almost exclusively within the thermosphere and is the dominant species at higher altitudes. Atomic oxygen is a significant contributor to the state of the IT region.

**2.1.1  The Thermosphere.**  The thermosphere is a fluid medium governed by frequent collisions between individual particles of gas. When fluid density and scale sizes are appropriate, a researcher may invoke the use of bulk fluid property governing equations such as the Navier-Stokes equations, continuity and energy. In the terms of the IT system and atmospheric science the validity of these equations are usable up until the 'exobase', where the fluid approximation is not possible. Below the exobase the distance traveled between collisions is short compared to the scale sizes of interest, and above this the mean free path between collisions can exceed tens of kilometers [17]. For Earth, the exobase is around 600 km. The altitudes between 80 km to 600
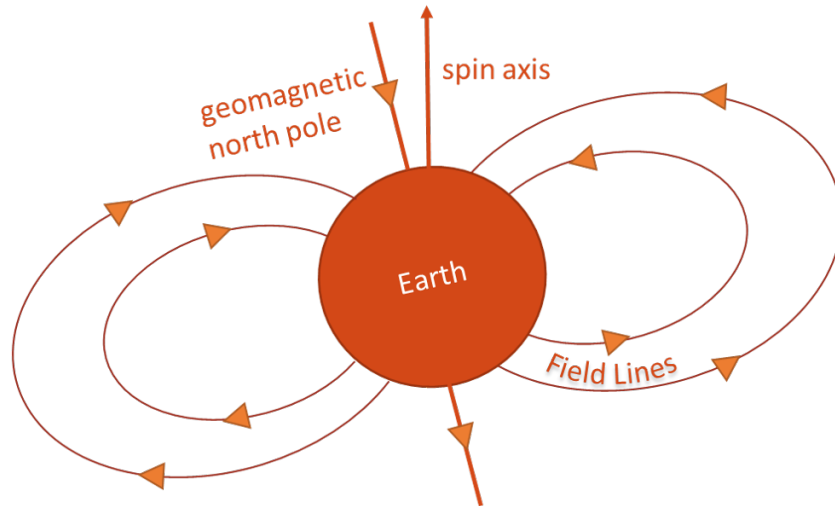
Figure 2.1. A schematic drawing of the Earth's magnetic field with the geomagnetic north pole, spin axis and field lines labeled.

km constitute the last layer of Earth which may be considered a fluid and as such many properties change along this distance.

Earth has an internally-generated magnetic field that interacts heavily with the thermosphere. The Earth's magnetic field may be simplified as a dipole with its axis offset by approximately 11 degrees from Earth's spin axis. It is created by currents generated by the molten and electrically conducting interior of Earth. Figure 2.1 shows a few dipole field lines with arrows indicating the direction of Earth's magnetic field. It is useful to produce a geomagnetic grid that projects the Earth's magnetic field onto its geographic surface. This is accomplished by defining the magnetic equator as the latitudinal zone at which the magnetic field lies in the plane of Earth's surface. The orientation of the magnetic field with the local horizontal is quantified by the inclination angle (i.e., dip angle). At the magnetic equator the inclination angle is zero and at the north pole it is -90 degrees. Convention states that north of the magnetic equator the inclination angle is positive and south it is negative. Modeling methods typically use geomagnetic field coordinates instead of geographic because of the interaction between the Earth's magnetic field and atmosphere.
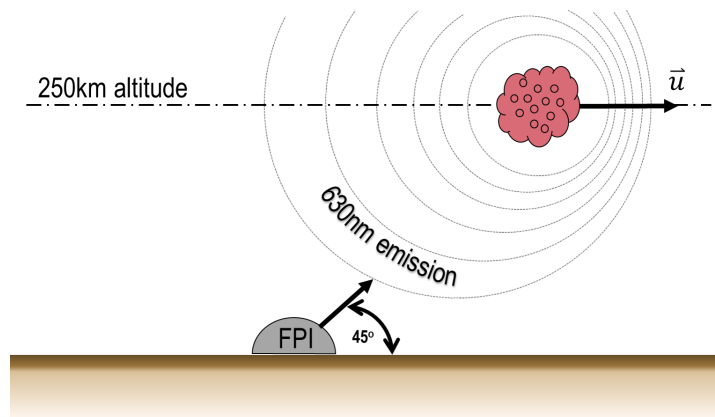
Figure 2.2. An FPI measuring the Doppler shifted emission emitted from the relaxation of a recombined $O_2^+$ ion.

The day to day variability of the thermosphere is well known [18, 19]. Above 200 km, many measurement techniques exist that allow researchers to validate first principle models or create empirical models that are fits to data. Below this altitude, particularly from 120-200 km a lot is unknown due to lack of measurements [20]. For the regions above 200 km the thermospheric winds are eastward during the night (1600-0400 local time) and switch to westward during day (04-16) local time [20]. This zonal behavior is true for all latitudes on Earth. Conversely, the meridional winds (i.e., north/southward) depend on latitude. The winds in the northern and southern hemispheres will blow equatorward during the night and poleward during the day. The relationship of the thermospheric winds to the geomagnetic equator is a consequence of the interaction between the neutral and ionized portions of the ionosphere-thermosphere system.

The thermosphere can be measured in several ways. One source is from Fabry-Perot interferometry (FPI). This method is a passive radio technique which measures the Doppler shift of recombination electromagnetic emissions being emitted by formerly ionized species [12]. Figure 2.2 shows a schematic diagram of an FPI instrument. FPI instruments measure line-of-sight (LOS) winds only. In the case of this

image, the FPI is located on the ground and looking up at a 45 degree angle. The formerly ionized species emits energy in the form of light and is traveling at some unknown velocity and direction. The signals received by the FPI are a Doppler shifted signal specific to a given species. The most commonly measured signal is the 630 nm 'red line' recombination emission from ionized molecular oxygen, $O_2^+$. Once $O_2^+$ encounters a free electron it relaxes after approximately 110 seconds and traveling distances much greater than the mean-free-path of particles at these altitudes. 630 nm is an optical emission just below the 700 nm cut off in the visible range and produces a red visible glow. Different species also emit different spectra.

Empirical models of thermospheric winds depend almost entirely on available data. One such model is the Horizontal Wind Model 2014 (HWM14) which uses ground-based FPI data but also incoherent scatter radar (ISR), satellite, and rocket datasets [20].

**2.1.2 The Ionosphere.** The ionosphere is diffuse and permeates the entire thermosphere from 80-600 km as well as extending into the exosphere 600-1000 km. Unlike the thermosphere, the ionosphere is broken up into distinct layers based on altitude (Figure 2.3). The climatology of the Ionosphere is well understood. Figure 2.3 shows how the ionosphere grows during the day from photoionization of neutral species due to extreme ultra-violet and X-rays and then, through recombination, shrinks at night. As the ionizing photons enter into the atmosphere, the plasma density increases up to a point where the balance between increasing neutral density and a reduction in solar flux due to absorption. The ionosphere also varies with solar cycle. The Sun undergoes a cycle where the net output of ionizing radiation peaks and weakens every 11 years. This effect is shown in Figure 2.3 with the dotted lines representing solar minimum and the solid lines representing solar maximum. Without these atmospheric layers, the ionizing radiation that reaches the ground would substantially increase.
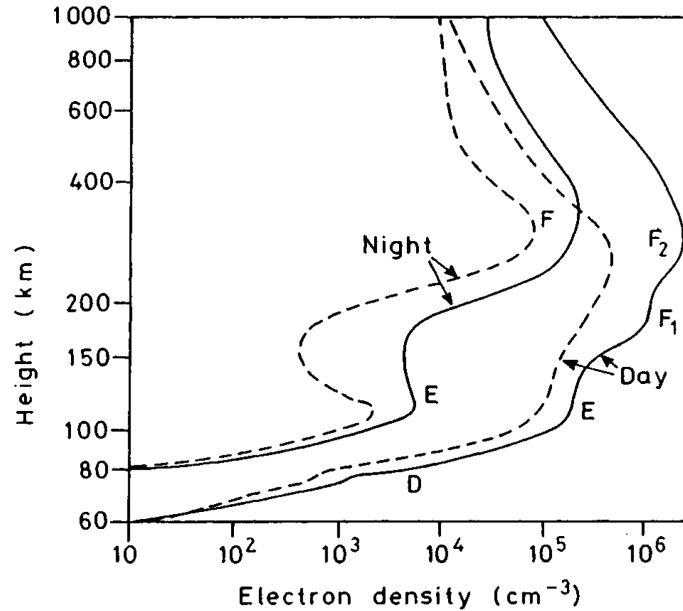
Figure 2.3. The layers of the ionosphere. Solid lines correspond to solar maximum and dashed are for solar minimum. [1]

The evolution of the ionosphere can be mathematically modeled by using the ion continuity equation:

$$\frac{dN}{dt} = \underbrace{s_P + s_L}_{\text{source terms}} + \underbrace{\vec{\nabla} \cdot (N\vec{v})}_{\text{convective terms}} \qquad (2.1)$$

Where $N$ is the number density, $t$ is the time, $s_P$ and $s_L$ are two source terms that represent production and loss, and the convective term contains the divergence of $\vec{\nabla}$ dotted with $N$ and $\vec{v}$ (ion velocity). The production and loss terms to first order may be represented by an atmosphere of only atomic oxygen ($O$) as this ionized species primarily dominates the ionosphere. Higher order models typically begin to add in more species. Convection is the transport of plasma throughout a region. Before describing the convective term, it is necessary to discuss ion transport in the presence of electric and magnetic fields.

When an ion encounters a magnetic field such as the Earth's, depending on
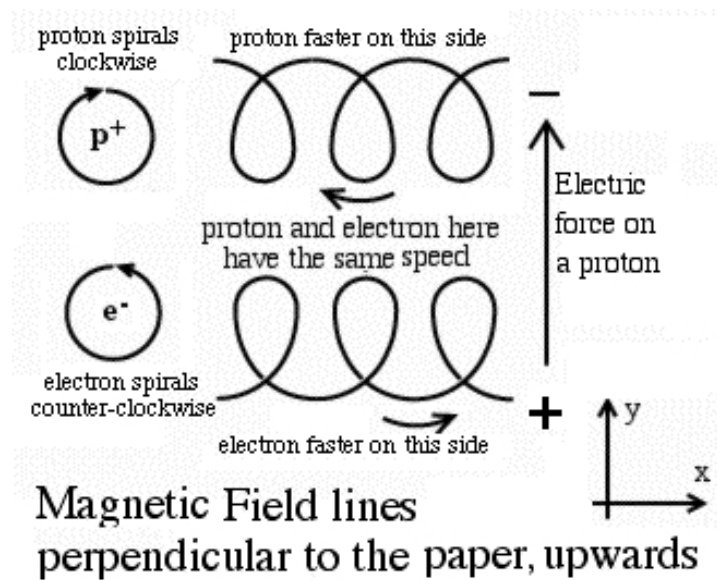
Figure 2.4. Ion drift due to electric and magnetic fields [2].

its charge, it will begin to gyrate in a circular motion as shown in Figure 2.4. If a charged particle is in the presence of a magnetic and electric field (as is the case with the ionosphere) then a particle will begin to drift. Equation (2.2) shows the mathematical representation of charged particle drift (often called 'E cross B' drift).

$$\vec{\mathbf{v}}_{\perp} = \frac{\vec{E} \times \vec{B}}{||\vec{\mathbf{B}}||^2} = \frac{-\vec{\nabla}V \times \vec{B}}{B^2} \tag{2.2}$$

where $\vec{E}$ is the electric field vector, $\vec{B}$ is the magnetic field vector, $V$ is the electric potential and $||\vec{\mathbf{x}}||$ is the norm operator. From here on $B^2$ will simply refer to the norm squared of $\vec{\mathbf{B}}$. The electric and magnetic fields are not the only drivers of ion convection; the neutral wind also plays a very important role.

**2.1.3 Ionosphere-Thermosphere Coupling.** The ionized and neutral species interact through collisions which is often called ion drag when discussed in a thermosphere centered frame. As the neutrals move, the collisions with ions must be taken into account and act to reduce the effect of other thermospheric drivers. The inverse is also true if studying ion motion where, if neutral winds are accelerated by different

drivers, then they can accelerate or decelerate the ions. This interaction is called the neutral wind dynamo.

If the electric field were absent as a driver and there were only magnetic fields and a mixed ionized and neutral atmosphere, then the motion would be governed solely by a ratio of ion-neutral collisions to gyro frequency, $\rho_+$. The motion of ions due to neutral winds is described in Equation (2.3) [21].

$$\vec{v} = \frac{1}{1 + \rho_+^2} \left[ \rho_+^2 \vec{u} + \rho_+ \vec{u} \times \hat{b} + (\vec{u} \cdot \hat{b})\hat{b} \right] \tag{2.3}$$

Where $\vec{v}$ is the ion drift, $\vec{u}$ is the neutral wind and $\hat{b}$ is the magnetic field direction. At higher altitudes (F-region) where $\rho_+ << 1$, the expression above simplifies to just the last term and we have:

$$\vec{v} = (\vec{u} \cdot \hat{b})\hat{b} \tag{2.4}$$

This shows that the motion of ions is oriented with respect to the magnetic and electric fields of Earth, and so it is common that to orient a coordinate system with the magnetic field.

Not only do neutral winds drive motion along field lines, but also gravity and diffusion play a role. Equation (2.1) can be rewritten now with all this new information as:

$$\frac{dN}{dt} = \underbrace{s_P - s_L}_{\text{source terms}} - \underbrace{\vec{\nabla} \cdot (N\vec{v}_\perp)}_{\hat{b}_\perp \text{transport terms}} - \underbrace{\vec{\nabla} \cdot (N\left[\vec{u} + \vec{v}_g + \vec{v}_D\right] \cdot \hat{b})}_{\hat{b}_\parallel \text{ transport terms}} \tag{2.5}$$

Where $\vec{v}_g$ represents the gravity term and $\vec{v}_D$ represents the diffusion term. Equation 2.5 is one of several governing equations of the ionosphere; others include the magnetohydrodynamic equations (i.e., modified Navier-Stokes). The interested reader should consult resources such as [22, 1, 23].

Measuring the terms in Equation 2.5 can be accomplished using ground-based, space-based or in situ measurements. One of the largest data sets available is provided by Global Navigation Satellite Systems (GNSS) for indirectly measuring the electron density $N$. GNSS satellites, originally designed for navigation positioning, transmit signals that penetrate the ionosphere from satellite to receiver. As the trans-ionospheric signal passes through the ionized gas, it is slowed. The amount by which the signal is slowed depends on the frequency of the signal because the ionosphere is dispersive. Just as a prism can separate white light into different colors, the ionosphere delays different frequencies by different amounts. This dispersive property of the ionosphere is what allows dual frequency measurements to measure the electron density [1]. The total integrated electron density along a ray path is called the slant total electron content (sTEC). Techniques for extracting the electron density $N$ at a given grid point from sTEC include Ionospheric Data Assimilation 4 Dimensional (IDA4D) [24], the Utah State University Global Assimilation of Ionospheric Measurements (USU GAIM) , the University of Southern California and Jet Propulsion Laboratory Global Assimilative Ionospheric Model (USC-JPL GAIM). Each of these algorithms is a class of data assimilation methods that combine model simulations and measurement data sets to provide estimates of $N$ on a 3 or 4 dimensional grid (space and time). This dissertation makes use of the IDA4D method outputs of $N$ to produce estimates of $dN/dt$. For more techniques in measuring the ionospheric state, please refer to [1].

## 2.2  Optimal Data Assimilation

The verb assimilate is defined by the Merriam-Webster Dictionary as, 'to take into the mind and thoroughly understand' [25]. In data assimilation, the 'mind' is the model, the process of 'taking in' data is the algorithm, and 'understanding' is the subsequent output (or model adjustment, if that is the goal). For studying

the ionosphere-thermosphere region, there are many ways to assimilate data. This dissertation presents the use of Kalman filtering to estimate basis function coefficients for interpolation or extrapolation between spatially distributed data.

Kalman filtering is a linear optimal estimator that seeks to minimize the mean-squared error during inversion. Originally, a method was developed by N. Weimer's work in the 1940's [26] and later redefined by R.E. Kalman in the 1960's paper [27]. Other linear estimators exist for inversion (i.e., least-squares estimation) however, when data is stochastic and includes mean and standard deviations, a Kalman filter is very useful for reducing error in the final estimation. The next subsection describes the components that make up a Kalman filter, and then the last subsection will describe the EMPIRE algorithm.

**2.2.1 Kalman Filtering Theory.** For this section, I describe the terms used in basic Kalman filters. The variables and symbols used here are the same symbols present in the text book, "Introduction to Random Signals and Applied Kalman Filtering" by R.G. Brown and P.Y.C. Hwang [28]. This section provides the minimum components needed to describe a full Kalman filter.

A Kalman filter consists of a recursive dynamic model and a measurement model. The dynamic model describes a dynamic process over time and the measurement model is used to update a state estimate given observations at discrete points in time. Equations (2.6) and (2.7) shown below are the dynamic model and measurement , respectively:

$$\mathbf{x}_{k+1} = \mathbf{\Phi}_k \mathbf{x}_k + \mathbf{w}_k \tag{2.6}$$

$$\mathbf{z}_k = \mathbf{H}_k \mathbf{x}_k + \mathbf{v}_k \tag{2.7}$$

where

$\mathbf{x}_k = (n \times 1)$ process state vector at time $t_k$

$\boldsymbol{\Phi}_k = (n \times n)$ matrix relating $\mathbf{x}_k$ to $\mathbf{x}_{k+1}$.

$\mathbf{w}_k = (n \times 1)$ process noise vector assuming a Gaussian sequence with a known covariance structure.

$\mathbf{z}_k = (m \times 1)$ observation vector at time $t_k$

$\mathbf{H}_k = (m \times m)$ matrix giving the noiseless connection between the measurement and the state vector at time $t_k$

$\mathbf{v}_k = (m \times 1)$ observation error vector that is assumed to be a white sequence with known covariance and having zero cross-correlation with $\mathbf{w}_k$

The covariance matrices for the process noise $\mathbf{w}_k$ and measurement noise $\mathbf{v}_k$ are defined as:

$$E\left\{\mathbf{w}_k \mathbf{w}_i^\top\right\} = \begin{cases} \mathbf{Q}_k, & i = k \\ \\ \mathbf{0}, & i = k \end{cases} \tag{2.8}$$

$$E\left\{\mathbf{v}_k \mathbf{v}_i^\top\right\} = \begin{cases} \mathbf{P}_k, & i = k \\ \\ 0, & i = k \end{cases} \tag{2.9}$$

where the $E$ denotes the expectation of the quantity in braces, $\mathbf{Q}$ is the forecast covariance and $\mathbf{P}$ is the observation covariance. Specifying an error of the filter's state estimate as the true value $\mathbf{x}_k$ and subtracting off it the new filter's estimated value $\hat{\mathbf{x}}_k^-$, we have an expression for the error of the filter as:

$$\mathbf{e}_k^- = \mathbf{x}_k - \hat{\mathbf{x}}_k^- \tag{2.10}$$

and its associated error covariance matrix as:

$$\mathbf{P}_k^- = E\left\{\mathbf{e}_k^- \mathbf{e}_k^{-\top}\right\} = E\left\{(\mathbf{x}_k - \hat{\mathbf{x}}_k^-)(\mathbf{x}_k - \hat{\mathbf{x}}_k^-)^\top\right\} \qquad (2.11)$$

R.G. Brown then creates an expression that mixes the noisy measurement, $\mathbf{z}_k$ and the prior estimate (i.e., the forecasted estimate $\hat{\mathbf{x}}_k^-$) thereby defining what is called the measurement update estimate, $\hat{\mathbf{x}}_k^-$:

$$\hat{\mathbf{x}}_k = \hat{\mathbf{x}}_k^- + \mathbf{K}_k(\mathbf{z}_k - \mathbf{H}_k \hat{\mathbf{x}}_k^-) \qquad (2.12)$$

The Kalman gain $\mathbf{K}_k$ not only maps measurement space to the state space but it also weights the measurements according to their covariances. In order to define the most optimal state estimate $\hat{\mathbf{x}}_k$ the covariance matrix for it, $\mathbf{P}_k$ must be minimized. $\mathbf{P}_k$ is defined below:

$$\mathbf{P}_k = E\left\{\mathbf{e}_k \mathbf{e}_k^\top\right\} = E\left\{\mathbf{e}_k \mathbf{e}_k^\top\right\} = E\left\{(\mathbf{x}_k - \hat{\mathbf{x}}_k)(\mathbf{x}_k - \hat{\mathbf{x}}_k)^\top\right\} \qquad (2.13)$$

Plugging in Eq. (2.12) into the above expression for the state estimate covariance creates an expression for the error of $\hat{\mathbf{x}}_k$ which must be minimized. R.G. Brown then uses a matrix differentiation method outlined in Section 4.2 of [28] that then produces an expression for $\mathbf{K}_k$ as:

$$\mathbf{K}_k = \mathbf{P}_k^- \mathbf{H}_k^\top (\mathbf{H}_k \mathbf{P}_k^- \mathbf{H}_k^\top + \mathbf{R}_k)^{-1} \qquad (2.14)$$

where $\mathbf{P}_k^-$ is the forecast variance. This particular weighting matrix, $\mathbf{K}_k$ minimizes the mean-square estimation error on $\hat{\mathbf{x}}$ and therefore we have an expression for the mean-square estimation covariance as:

$$\mathbf{P}_k = (\mathbf{I} - \mathbf{K}_k \mathbf{H}_k)\mathbf{P}_k^- \qquad (2.15)$$
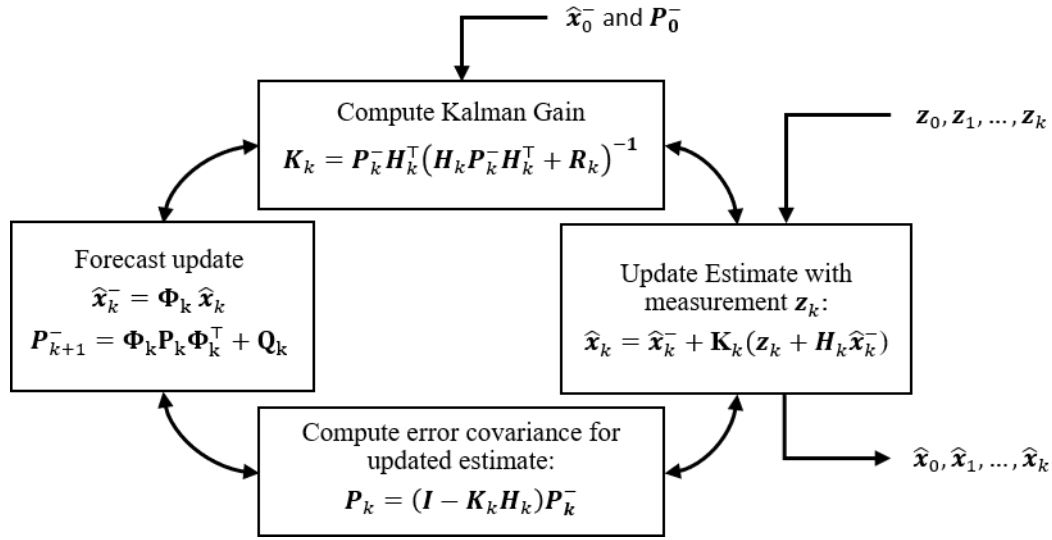
Figure 2.5. Kalman filtering process diagram.

and now it is possible to define the forecast using the process (i.e., dynamic) model equation Eq. (2.6):

$$\hat{\mathbf{x}}_{k+1}^- = \mathbf{\Phi}_k \hat{\mathbf{x}}_k \tag{2.16}$$

The above expression is missing the $\mathbf{w}_k$ because process noise has zero mean and is not correlated with any previous $\mathbf{w}$'s. R.G. Brown then forms the expression for the a priori error and produces the following expression:

$$\mathbf{P}_{k+1}^- = \mathbf{\Phi}_k \mathbf{P}_k \mathbf{\Phi}_k^\top + \mathbf{Q}_k \tag{2.17}$$

R.G. Brown provides an illustration of the Kalman filtering process that has been adapted in Figure 2.5. This figure will be used as a template as a means for establishing my contributions in the field of aeronomy and space physics of the ionosphere-thermosphere region.

**2.2.2 EMPIRE Algorithm.** EMPIRE is a data assimilation algorithm that uses IDA4D time-evolving global estimates of plasma density, $N$, to estimate the electric potential and neutral wind drivers of plasma density rate, $dN/dt$ [29]. EMPIRE does

this by using the ion continuity equation (Eq. 2.5) shown below:

$$\frac{dN}{dt} = \underbrace{s_P - s_L}_{\text{source terms}} - \underbrace{\vec{\nabla} \cdot (N\vec{\mathbf{v}}_\perp)}_{\hat{b}_\perp \text{terms}} - \underbrace{\vec{\nabla} \cdot (N\vec{v}_\parallel)}_{\hat{b}_\parallel \text{terms}} \qquad (2.18)$$

Where $\vec{v}_\parallel$ is

$$\vec{v}_\parallel = [\vec{u} + \vec{v}_g + \vec{v}_D] \cdot \hat{b} \qquad (2.19)$$

where $\hat{b}$ is the magnetic field aligned unit vector direction. EMPIRE casts the ion continuity equation into a form below:

$$y = a + v \qquad (2.20)$$

Where $y$ represents the LHS of the ion continuity equation (i.e., observations of $dN/dt$), $a$ represents a model of $dN/dt$ and $v$ represents the bias error due to a measurement. The model $a$ is equal to:

$$a = \underbrace{a_P + a_L}_{\text{source terms}} + \underbrace{a_{exb}}_{\hat{b}_\perp \text{terms}} + \underbrace{a_u + a_g + a_D}_{\hat{b}_\parallel \text{terms}} \qquad (2.21)$$

Where $a_P$ is the production model, $a_L$ is the loss model, $a_{exb}$ is the field perpendicular drift convection model, $a_u$ is the field parallel neutral wind convection model, $a_g$ is the field parallel gravity model and $a_D$ is the field parallel diffusion model. Each $a_X$ term above represents a different driver of $dN/dt$ and are obtainable through a model simulation.

At any given time the solar conditions vary and EMPIRE's purpose is to provide updates to models and adjust them based on the current conditions. EMPIRE makes use of well documented models that have proven successful in reproducing Sq conditions in the IT and adjusts the models according to current solar activity. This

allows EMPIRE to be used to estimate the enhancement that solar activity has on specific drivers. To described this enhancement I add a $\delta a$ to Equation (2.20) as shown below:

$$y = a + \delta a + \nu_a + \nu \tag{2.22}$$

The measurement inputs, $y$, are also considered to have zero bias. This reduces Equation (2.22) to the following:

$$y = a + \delta a \tag{2.23}$$

EMPIRE's estimation of $\delta a$ is accomplished by moving all unknowns to the LHS and casting $\delta a$ into a linear system that depends on which drivers are being estimated.

$$y - a = \delta a \tag{2.24}$$

The ion continuity equation is used as a mapping function to map from from observation of the enhancements to coefficients of basis functions that will represent the correction to a driver.

$$y - a = \mathbf{H}\mathbf{x} \tag{2.25}$$

where $\mathbf{H}$ is the mapping matrix and $\vec{\mathbf{x}}$ are the basis function coefficients. EMPIRE has previously been used to study enhancements in electrostatic potential and neutral wind drivers. Electric fields as well as neutral wind enhancements along the magnetic field line are the primary drivers during geomagnetic storm events. When both of
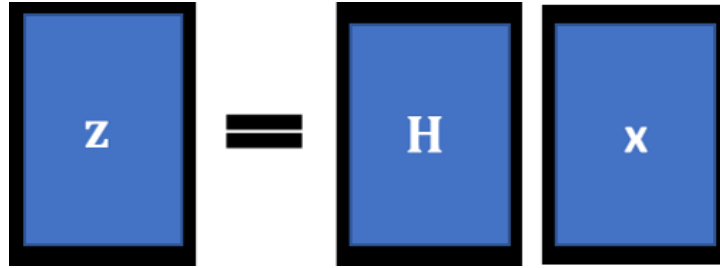
Figure 2.6. Block representation for a linear measurement model, $\mathbf{z} = \mathbf{Hx}$.

these drivers are estimated simultaneously [16] the linear system looks like:

$$\mathbf{H} = \begin{bmatrix} \mathbf{H}_V & \mathbf{H}_\| \end{bmatrix} \tag{2.26}$$

$$\mathbf{y} - \mathbf{a} = \begin{bmatrix} \mathbf{H}_V & \mathbf{H}_\| \end{bmatrix} \begin{bmatrix} \mathbf{x}_V \\ \mathbf{x}_\| \end{bmatrix} \tag{2.27}$$

$$\mathbf{z} = \mathbf{Hx}_\| \tag{2.28}$$

This linear system can be represented using a block diagram where each block represents a term from the linear measurement model. Figure 2.6 shows a linear measurement model represented using blocks. The EMPIRE algorithm's primary function is to provide a self consistent solution with IDA4D plasma density specifications and the ion continuity equation, (2.18). Linearization (Eq. (2.25) allows EMPIRE to use techniques such as Kalman filtering to produce optimal mean-square error estimates on $\mathbf{x}$. This thesis lays out the ground work for implementation of Kalman filtering, successfully ingests a new neutral wind data source (Fabry-Perot interferometer measurements) and spherical harmonic basis functions for enabling global estimates of the physical drivers of the IT system.

CHAPTER 3

KALMAN FILTERING FOR REGIONAL ESTIMATION

This chapter describes how EMPIRE's estimation method was modified to use a Kalman filter. It builds from the Kalman filtering background section and establishes the definition of each Kalman filtering parameter in the context of estimation of the IT system drivers.

Previously, EMPIRE used a weighted-least-squares estimation method and showed promise toward estimation of ionospheric drivers [14, 15, 16]. Least-squares has the form:

$$\hat{\mathbf{x}} = (\mathbf{H}^\top \mathbf{W} \mathbf{H})^{-1} \mathbf{H}^\top \mathbf{W}(\mathbf{z}) \tag{3.1}$$

where $\mathbf{H}$ is the observation matrix, $\hat{\mathbf{x}}$ is the state, $\mathbf{z}$ is the observation and $\mathbf{W}$ is the weighting matrix. This method has no way to connect state estimates $\hat{\mathbf{x}}_k$ to the future state estimates $\hat{\mathbf{x}}_{k+1|k}$ but does allow for assimilation of multiple observations $\mathbf{z}$ to produce a state estimate $\mathbf{x}$ for a given time step. The terms in equation (3.1) do not need to change because the measurement model remains the same but the inversion equation (called the measurement update) does change to equation (3.2) reprinted below:

$$\hat{\mathbf{x}}_k = \hat{\mathbf{x}}_k^- + \mathbf{K}_k(\mathbf{z}_k - \mathbf{H}_k \hat{\mathbf{x}}_k^-) \tag{3.2}$$

where each term was previously defined in Section 2.2.1 and $\mathbf{K}_k$ is defined as:

$$\mathbf{K}_k = \mathbf{P}_k^- \mathbf{H}_k^\top (\mathbf{H}_k \mathbf{P}_k^- \mathbf{H}_k^\top + \mathbf{R}_k)^{-1} \tag{3.3}$$

Also, not available with least-square estimation is the ability to adjust the state over time. This is done using a dynamic model as shown in equation (2.6).
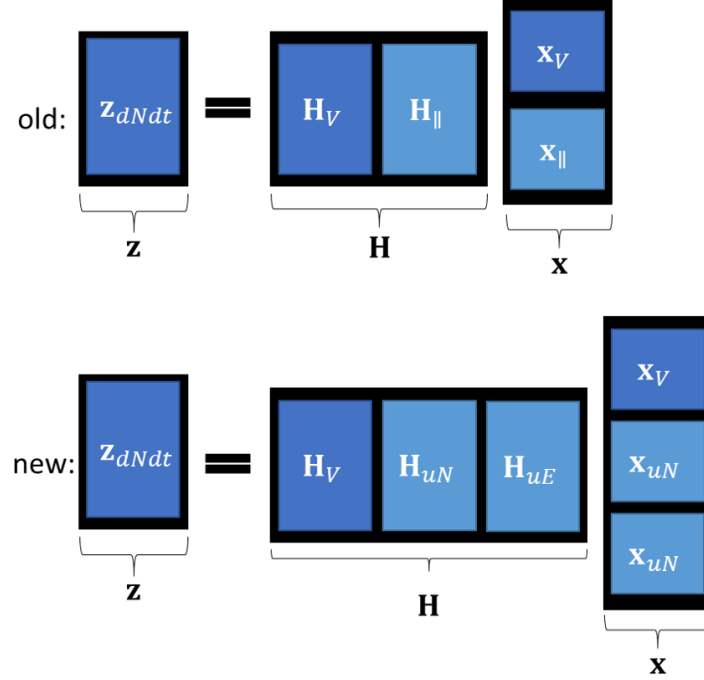
Figure 3.1. EMPIRE measurement model from estimation of parallel neutral winds to estimation of geographic northern and eastern horizontal neutral winds

This chapter proposes two changes to EMPIRE: first, a switch from least-square estimation to Kalman filtering and second, a change of the state from estimating electric potential and parallel neutral wind corrections to estimating north and east neutral wind corrections separately. Changing the state removes $\hat{\mathbf{x}}_\parallel$ and adds the states $\hat{\mathbf{x}}_{uN}$ and $\hat{\mathbf{x}}_{uE}$. The reason for doing this is to prepare EMPIRE for ingestion of Fabry-Perot interferometer (FPI) neutral wind measurement shown in Chapter 4. The change in the measurement model is illustrated with the light blue blocks in Figure 3.1. There are two main models that a Kalman filter requires: the measurement model and dynamic model (see Section 2.2.1). The measurement model is used to estimate the background climate model 'error' and the dynamic model is used to forecast that 'error' from one time step to the next. The EMPIRE algorithm as previously formulated without Kalman filtering is detailed in Appendix A of [16].

Ingestion of plasma densities $N$ is accomplished by organizing measurements

on a gridded region at consecutive time intervals, either from a model or data as-similative method such as IDA4D. In this work, IDA4D is used to specify a global grid of data at 3 degree geomagnetic latitude ($\theta$) and longitude ($\phi$). IDA4D provides the mean and standard deviation of plasma density, $N$, at each time step. EMPIRE subsequently estimates the physical drivers using the ion continuity equation. To do this, EMPIRE center finite differences the gridded $N$ to produce $dN/dt$ in which the time at the midpoint is taken.

$$\frac{\Delta N}{\Delta t}_{(t+\frac{1}{2}\Delta t)} = \frac{N(t_2)_i - N(t_1)_i}{\Delta t} \tag{3.4}$$

The index $i$ is used as a grid point index and to recognize $N$ is specified across the globe at at individual (latitude, longitude and radius) points. The standard deviation chosen for a given midpoint time (i.e., $t+\frac{1}{2}\Delta$) is the greater of the standard deviation at either time step rather than the linear combination of the two:

$$\sigma_{(t+\frac{1}{2}\Delta t)} = \max(\sigma_{t_1}, \sigma_{t_2}) \tag{3.5}$$

EMPIRE uses the specified electron densities and formulates an overdetermined linear system based on the ion continuity equation to estimate the state, i.e. the coefficients to a functional form for neutral wind and electric potential. Estimates of electron density are assumed equivalent to ion densities by the quasi-neutrality of the ionosphere. We start from the main linear equations upon which the additional data ingestion and Kalman filtering are built.

The spatial region being imaged is gridded by geomagnetic colatitude $\theta$, longitude $\phi$ and radius $R = R_e + r$, where $R_e$ is the mean radius of Earth and $r$ is the altitude of a given point in the ionosphere. At these grid points EMPIRE computes the background model and solves for terms that are within the ion continuity equation

shown below:

$$\frac{dN}{dt} = \underbrace{s_P}_{a_P} + \underbrace{s_L}_{a_L} \underbrace{-\vec{\nabla} \cdot (N\vec{v}_\perp)}_{a_{exb}} \underbrace{-\vec{\nabla} \cdot (N\vec{v}_\parallel)}_{a_\parallel} \tag{3.6}$$

$$a_N \triangleq a_P + a_L + a_{exb} + a_\parallel + \delta a_{exb} + \delta a_\parallel \tag{3.7}$$

Each of these $a_{terms}$, where "$terms$" $= \{P, L, \parallel, exb\}$ may be represented by a background model $a_{term}$ and are corrected by the estimation process with $\delta a_{term}$.

The term $a_N$ is defined as the background model for the change in electron density, $N$, over time. Within this background model $a_P$ represents the production rate, $a_L$ the loss rate, and $a_\parallel$ and $a_{exb}$ are drift terms parallel and perpendicular to the local magnetic field line, respectively. The subscript '$exb$' to represent the assumption that $\vec{E} \times \vec{B}$ drift is the primary driver for ion drifts that are perpendicular to the magnetic field line.

The equation is stacked into a system of linear equations of the form:

$$\mathbf{y}_N = \mathbf{H}_N \mathbf{x} + \mathbf{a}_N + \mathbf{v}_N \tag{3.8}$$

$$\mathbf{y}_N = \left[ \frac{\Delta N_1}{\Delta t} \frac{\Delta N_2}{\Delta t} \dots \frac{\Delta N_i}{\Delta t} \right]^T \tag{3.9}$$

$$\mathbf{a}_N = \left[ a_{N1} a_{N2} \dots a_{Ni} \dots a_{Ni_{max}} \right]^T \tag{3.10}$$

$$a_{Ni} = a_{Pi} + a_{Li} + a_{exbi} + a_{\parallel i} \tag{3.11}$$

The corrections $\delta a_{term}$ are estimated as part of the state vector $\mathbf{x}$, the sum of the background models at all $i$ gridpoints is $\mathbf{a}_N$, and $\mathbf{v}_N$ is noise ($N(0, \mathbf{R}_N)$), zero mean with covariance $\mathbf{R}_N$) associated with $\mathbf{y}_N$ and $\mathbf{a}_N$. In these expressions, the elements of $\mathbf{y}_N$ are the finite differenced plasma densities, and $\mathbf{a}_N$ is generated based on background models of the ionosphere. The background models used in this study are

provided by the following: Kirchengast models [30], the Horizonal Wind Model 2014 (HWM14) [20], Weimer 2000 [26] and the International Geomagnetic Reference Field 11th generation (IGRF-11) [31].

The state $\mathbf{x}$ consists of:

$$\mathbf{x} \;=\; \begin{bmatrix} \mathbf{x}_{exb} \\[6pt] \mathbf{x}_{uN} \\[6pt] \mathbf{x}_{uE} \end{bmatrix} \tag{3.12}$$

Where each $\mathbf{x}_{term}$ is an array of the coefficients of the basis functions for that particular term. For example, $\mathbf{x}_{exb}$ consists of the coefficients for the ion drift term correction. If certain terms are not being corrected (in this study, production and loss are not corrected, i.e., $\delta a_{prod} = \delta a_{loss} = 0$), those are truncated from the state vector. See [3] for more information on the basis functions.

In this work I reformulate the problem to filter additional measurements beyond the IDA4D output-based finite-differenced density rates. The Kalman filtering in EMPIRE is based on a 3D variational (3DVAR) approach, [32, 33, 29]. There are many resources for understanding Kalman filtering [34, 35, 36] and how it is derived. This section describes how we use a Kalman filter for our estimation.

The EMPIRE algorithm with Kalman filtering is illustrated as a flow chart in Figure 3.2. Measurements $\mathbf{y_N}$ are derived from IDA4D, a 3D variational data assimilation method that uses dual-frequency Global Positioning Satellite (GPS) ground receivers and satellite occultation GPS receivers for total electron content (TEC) measurements, satellite in-situ plasma density measurements, and ionosonde measurements to obtain an optimal estimate of the global three-dimensional time-varying plasma density [29]. In cases in which FPI data measurements $\mathbf{y_u}$ (to be discussed

more in Chapter 4) are ingested, these are also included in $\mathbf{y}$. The EMPIRE Kalman filter performs a best fit to the difference between the measurements and models to produce a state estimate, which is done similarly to the IDA4D implementation [33, 32, 37, 29]. The state coefficients are then multiplied by the mapping matrix, $\mathbf{H}$, to give the EMPIRE correction estimate. Finally this correction is added to the background models to produce estimates of the ionospheric drivers, e.g., neutral winds. We express Eq. (3.8) in a more familiar form by rearranging it and including more traditional Kalman filter notation:

$$\mathbf{z} \triangleq \mathbf{y} - \mathbf{a} \tag{3.13}$$

$$\mathbf{z} = \mathbf{H}\mathbf{x} + \nu \tag{3.14}$$

$$\mathbf{z} = \begin{bmatrix} \mathbf{H}_V & \mathbf{H}_{uN} & \mathbf{H}_{uE} \end{bmatrix} \begin{bmatrix} \mathbf{x}_{exb} \\ \mathbf{x}_{uN} \\ \mathbf{x}_{uE} \end{bmatrix} \tag{3.15}$$

The submatrices $\mathbf{H}_V$, $\mathbf{H}_{uN}$ and $\mathbf{H}_{uE}$ are defined in Appendix A. In this formulation the state $\mathbf{x}$ is a best estimate of the discrepancy between the measurements $\mathbf{y}$ and model $\mathbf{a}$. Therefore, $\mathbf{z}$ is an adjustment to the background model, not the full ionospheric state. Since the system is linear, another way of saying this is that the full state is a superposition of the background model and the correction $\mathbf{x}$.

The Kalman filter implements a measurement update at time $t$ given measurements at time $t$ (notated as "$t|t$") and a time update to forecast to $t+1$ given measurements at $t$ (notated as "$t+1|t$"). The cost function penalizes the relative contributions of $\mathbf{x}_{t|t}$ according to their squared deviations from the measurements $\mathbf{z}$
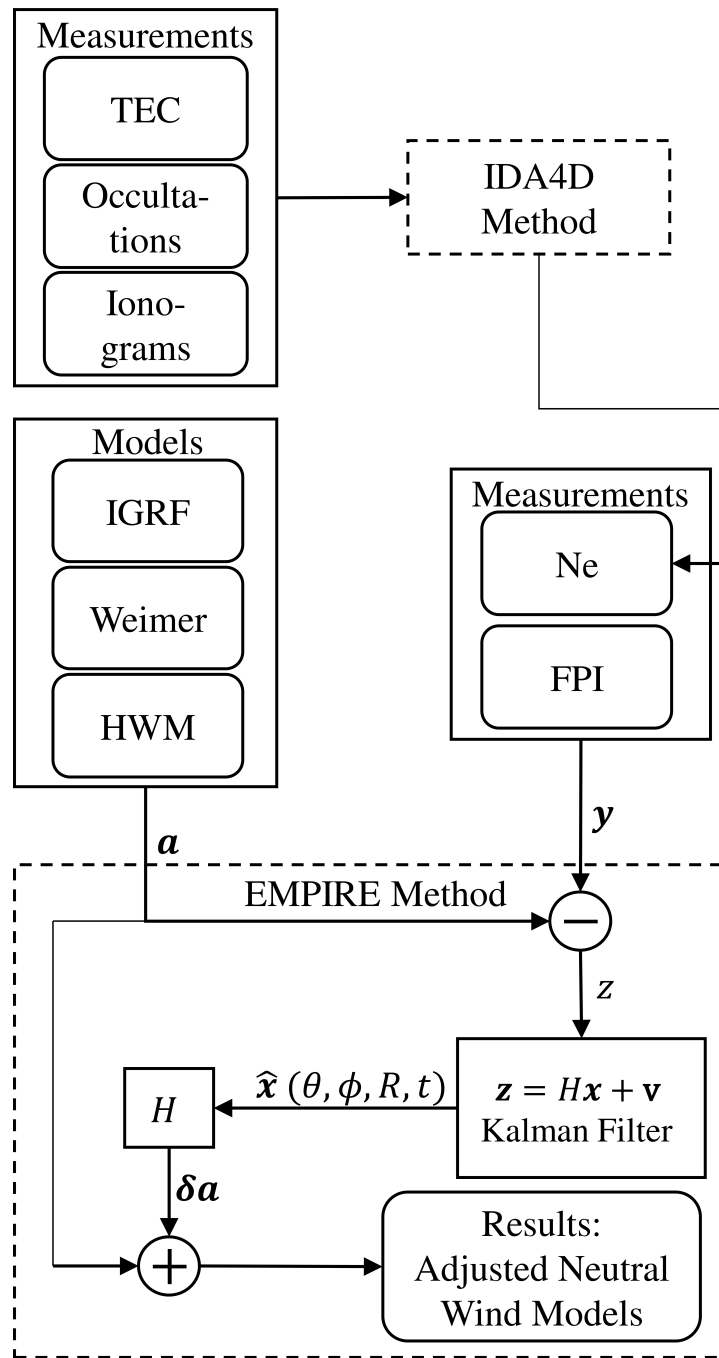
Figure 3.2. Simplified EMPIRE model and data processing flow chart [3]

and their squared error from the previously forecast estimate $\mathbf{x}_{t|t-1}$:

$$J = (\mathbf{z} - \mathbf{H}\hat{\mathbf{x}}_{t|t})^T \mathbf{R}^{-1}(\mathbf{z} - \mathbf{H}\hat{\mathbf{x}}_{t|t}) + (\hat{\mathbf{x}}_{t|t} - \hat{\mathbf{x}}_{t|t-1}^-)^T (\mathbf{P}_{t|t-1}^-)^{-1}(\hat{\mathbf{x}}_{t|t} - \hat{\mathbf{x}}_{t|t-1}^-)$$

(3.16)

where $\mathbf{P}_{t|t-1}^-$ is the covariance of the previous forecast update. The observation co-variance $\mathbf{R}$ comes from the published errors in the IDA4D and FPI data (see Eq. (4.11) for its definition in this study).

We expand the expression $\mathbf{H}(\hat{\mathbf{x}}_{t|t})$ around the previously forecast value as:

$$\mathbf{H}\hat{\mathbf{x}}_{t|t} = \mathbf{H}\hat{\mathbf{x}}_{t|t-1}^- + \mathbf{H}(\hat{\mathbf{x}}_{t|t} - \hat{\mathbf{x}}_{t|t-1}^-)$$

(3.17)

Substituting this expression into the cost function (Eq. (3.16)), computing the gradient with respect to $\hat{\mathbf{x}}_{t|t}$, and equating to 0 yields the optimal estimate:

$$\hat{\mathbf{x}}_{t|t} = \hat{\mathbf{x}}_{t|t-1}^- + (\mathbf{H}^T \mathbf{R}^{-1} \mathbf{H} + (\mathbf{P}_{t|t-1}^-)^{-1} \mathbf{H}^T \mathbf{R}^{-1}(\mathbf{z} - \mathbf{H}\hat{\mathbf{x}}_{t|t-1}^-)$$

(3.18)

This is a measurement update of the forecast state $\hat{\mathbf{x}}_{t|t-1}^-$, which is a correction to the background model $\mathbf{a}$. Using the Sherman-Morrison-Woodbury form [32], the error covariance of the measurement update estimate is:

$$\mathbf{P}_{t|t} = \mathbf{P}_{t|t-1}^- - \mathbf{P}_{t|t-1}^- \mathbf{H}^T (\mathbf{H}\mathbf{P}_{t|t-1}^- \mathbf{H}^T + \mathbf{R}^{-1})\mathbf{H}(\mathbf{P}_{t|t-1}^-)^T$$

(3.19)

For the dynamic model, we assume the state to be Gauss-Markov, with a transition of:

$$\hat{\mathbf{x}}_{t+1|t}^- = \mathbf{\Phi}\hat{\mathbf{x}}_{t|t} + \mathbf{w}_{t|t}$$

(3.20)

$$\mathbf{\Phi} = \exp\left(-\frac{t_{n+1} - t_n}{\tau}\right)\mathbf{I}$$

(3.21)

where the subscript n is the time index, $\mathbf{I}$ is the identity matrix, $\tau$ is a time constant is a tunable parameter which quantifies how rapidly measurements are "forgotten" and $\mathbf{w}$ is process noise that is normally distributed with zero mean and covariance $\mathbf{W}$. The time update is then given by:

$$\hat{\mathbf{x}}_{t+1|t} = \mathbf{\Phi}\hat{\mathbf{x}}_{t|t} \tag{3.22}$$

$$\mathbf{P}^{-}_{t+1|t} = \mathbf{\Phi}\mathbf{P}_{t|t}\mathbf{\Phi}^T + \mathbf{Q} \tag{3.23}$$

The covariance of the process noise $\mathbf{Q}$ is defined to have the forecast covariance revert to the model $\mathbf{a}$ covariance in the absence of measurements over time:

$$\mathbf{Q} = \left(1 - \exp\left(-\frac{t_{n+1} - t_n}{\tau}\right)\right)^2 \mathbf{R}_a \tag{3.24}$$

This concludes the definition of all necessary terms that were required to formulate the Kalman filter. This section showed the measurement model (Eqs. (3.13) through (3.15)), the measurement update (Eqs. (3.18) and (3.19)) and the dynamic model (Eqs. (3.22) and (3.23)). The next section shows how the measurement model is updated to include FPI neutral wind measurements.

CHAPTER 4

NEUTRAL WIND OBSERVATIONS

EMPIRE originally ingested a 4 dimensional grid of electron density from the Ionospheric Data Assimilation 4 Dimensional (IDA4D) algorithm. This contribution adds neutral wind measurements from Fabry-Perot Interferometers (FPI). The EMPIRE algorithm will have direct measurements of an ionospheric driver rather than indirectly estimating it from IDA4D electron density and the ion continuity equation. This provides a distinctive advantage as compared to electron density only information. Section 4.1 describes how the EMPIRE algorithm changes once FPI neutral wind measurements are introduced and Section 4.2 describes how EMPIRE was used to study Storm-Enhanced Densities (SEDs). SEDs refer to an enhancement in the ionospheric electron density due to geomagnetic storm-time processes.

## 4.1 Augmenting the EMPIRE Linear Measurement Model for FPI Neutral Wind Measurements

When neutral winds are assimilated into EMPIRE, the measurement model and dynamic models are augmented to include the new observation from Fabry-Perot interferometer (FPI). FPI neutral wind measurements provide direct measurements of the line-of-sight (LOS) thermospheric wind speeds $u_{LOS}$ and associated uncertainties at an assumed altitude of 250 km, see Figure 4.1. This assumption requires that the peak emissions originate from an altitude of 250 km.

The FPI makes measurements at an elevation of 45 degrees at the four cardinal azimuthal look directions (north, south, east and west). The LOS wind is the projection of the 3-dimensional geographic wind vector onto the LOS direction $\hat{k}$ from
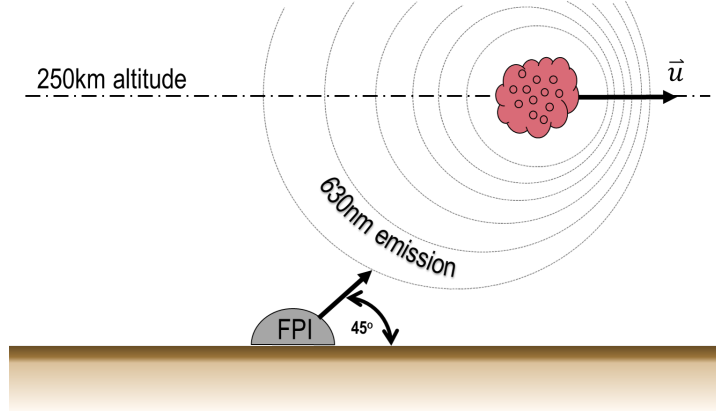
Figure 4.1. An FPI measuring the Doppler shifted emission emitted from the relaxation of a recombined $O_2^+$ atom.

the FPI toward the sky:

$$u_{LOS} = u_N \hat{n}_g \cdot \hat{k} + u_E \hat{e}_g \cdot \hat{k} \qquad (4.1)$$

$$= (a_{uN} + \delta a_{uN}) \hat{n}_g \cdot \hat{k} + (a_{uE} + \delta a_{uE}) \hat{e}_g \cdot \hat{k} \qquad (4.2)$$

Where $u_N$ and $u_E$ are the storm-time horizontal geodetic north and east neutral winds, $\hat{n}_g$ and $\hat{e}_g$ are the geodetic north and east unit vectors, $\hat{k}$ is the FPI LOS direction unit vector, $a_{uN}$ and $a_{uE}$ are the geodetic north and east model neutral wind values and $\delta a_{uN}$ and $\delta a_{uE}$ are the corrections to the geodetic north and east model neutral winds. As in Eqs. (3.6) -(3.7), the geographic zonal and meridional winds are assumed to be comprised of a model (using HWM14) to give $a_{uE}, a_{uN}$, and corrections $\delta a_{uE}$, $a_{uN}$. Each measurement $u_{LOS}$ is stacked into an array $\mathbf{y_u}$ of

thermospheric wind observations.

$$\mathbf{y}_u = \mathbf{H}_u\mathbf{x} + \mathbf{a}_u + \mathbf{v}_u \tag{4.3}$$

$$\mathbf{a_u} = \begin{bmatrix} a_{u_1} & a_{u_2} & \cdots a_{u_i} & \cdots & a_{u_{imax}} \end{bmatrix}^T \tag{4.4}$$

$$a_{u_i} = \begin{bmatrix} \cos(el_i)\sin(az_i) & \cos(el_i)\cos(az_i) & \sin(el_i) \end{bmatrix} \begin{bmatrix} a_{uE} \\ a_{uN} \\ 0 \end{bmatrix} \tag{4.5}$$

where $a_{u_i}$ is the LOS component of the background model neutral winds at the $i^{th}$ location, $el$ is the elevation angle, $az$ is the azimuthal angle of the LOS, and $\epsilon_u$ is measurement assumed to be white noise. The mapping matrix $\mathbf{H}_u$ is detailed in Appendix A of [3].

When ingesting neutral wind measurements, we augment the EMPIRE linear system to include not only the continuity equation (Eq. 3.8), but also the LOS neutral winds.

$$\underbrace{\begin{bmatrix} \mathbf{y}_N \\ \mathbf{y}_u \end{bmatrix}}_{\mathbf{y}} = \underbrace{\begin{bmatrix} \mathbf{H}_N \\ \mathbf{H}_u \end{bmatrix}}_{\mathbf{H}}\mathbf{x} + \underbrace{\begin{bmatrix} \mathbf{a}_N \\ \mathbf{a}_u \end{bmatrix}}_{\mathbf{a}} + \underbrace{\begin{bmatrix} \mathbf{v}_N \\ \mathbf{v}_u \end{bmatrix}}_{\mathbf{v}} \tag{4.6}$$

This also leads to an augmentation of the Kalman filter as shown below.

$$\mathbf{z} \;=\; \mathbf{Hx} + \boldsymbol{\nu} \tag{4.7}$$

$$\mathbf{z} \;=\; \mathbf{y} - \mathbf{a} = \begin{bmatrix} \mathbf{y_N} \\ \mathbf{y_u} \end{bmatrix} - \begin{bmatrix} \mathbf{a}_N \\ \mathbf{a_u} \end{bmatrix} \tag{4.8}$$

$$\mathbf{H} \;=\; \begin{bmatrix} \mathbf{H}_N \\ \mathbf{H}_u \end{bmatrix} = \begin{bmatrix} \mathbf{H}_V & \mathbf{H}_{uN} & \mathbf{H}_{uE} \\ \mathbf{0} & \tilde{\mathbf{H}}_{uN} & \tilde{\mathbf{H}}_{uE} \end{bmatrix} \tag{4.9}$$

$$\mathbf{z} \;=\; \begin{bmatrix} \mathbf{H}_V & \mathbf{H}_{uN} & \mathbf{H}_{uE} \\ \mathbf{0} & \tilde{\mathbf{H}}_{uN} & \tilde{\mathbf{H}}_{uE} \end{bmatrix} \begin{bmatrix} \mathbf{x}_V \\ \mathbf{x}_{uN} \\ \mathbf{x}_{uE} \end{bmatrix} \tag{4.10}$$

Where here I brought in $\mathbf{H}_N$ to differentiate between $\mathbf{H}_N$ and $\mathbf{H}_u$. From here, the same measurement update and dynamic model equation applies but with newly defined terms (See Eqs. (3.18), (3.19), (3.22) and (3.23)). This updates the EMPIRE measurement model from what was defined in Chapter 3 as equation (3.15) to equation (4.10). This change is illustrated with light blue blocks in Figure 4.2.

This concludes modification of the EMPIRE algorithm and my 2nd contribution. The next step was to test this algorithm and examine how the Kalman filter and FPI neutral winds affect the solution and what does ingestion of FPI data into a data assimilation environment tell us about neutral wind measurements and vise versa.

## 4.2 Application of EMPIRE to Study Geomagnetic Storm Enhanced Densities

In this section I apply the EMPIRE algorithm with the newly added KF
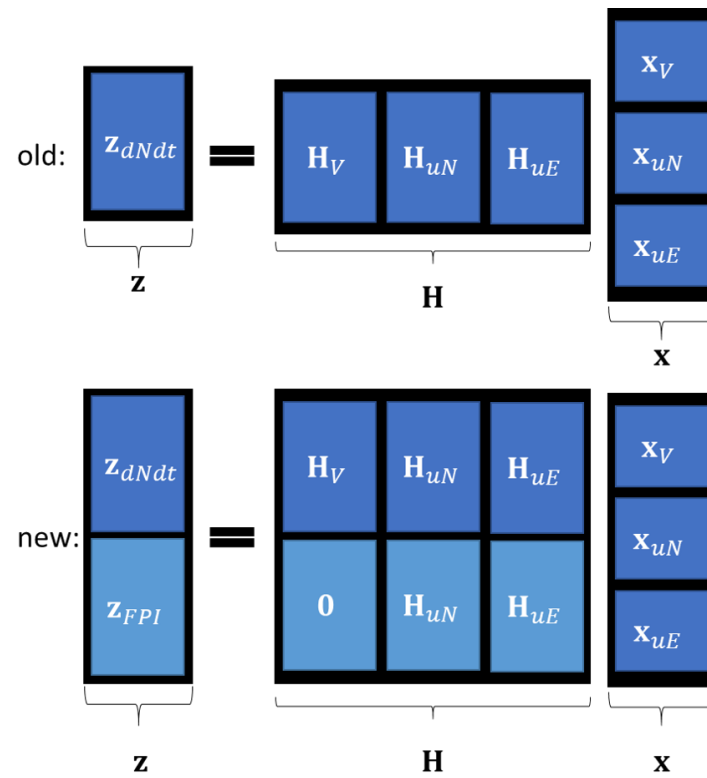
Figure 4.2. EMPIRE measurement model augmentation for ingestion of FPI neutral winds.

and FPI ingestion modifications from contributions 1 and 2 to study a geomagnetic storm. There are four subsections and they are laid out in a standard format with the method describing the EMPIRE configuration, results showing neutral winds and ion drift storm time EMPIRE estimates a discussion and concluding remarks. This work was published in 2016 in the peer reviewed journal of Radio Science [3].

**4.2.1 Method.** The storm to be studied occurred on 24-25 October 2011; Figure 4.3 shows the Dst index during this storm. The Dst minimum occurs at 0100 UT on 25 October. The storm led to a mid-latitude storm enhanced density (SED) in the afternoon/dusk sector over the U.S. [38]. In addition to the SED, there was a localized post-Sunset TEC enhancement over the southeastern United States. Similar mid-latitude TEC enhancements have been studied before [39, 40, 41, 42], albeit only for extreme geomagnetic storms [43].

In Figure 4.4, bi-hourly maps of the southeastern U.S. show the post-Sunset TEC enhancement. These figures were created using a 1-degree resolution grid in IDA4D to generate electron densities that are then integrated to give vertical TEC.

During this storm, a mid-latitude FPI of the North American Thermosphere Ionosphere Observation Network (NATION) array was operational, at Pisgah Astronomical Research Institute (PARI) [44]. The location of the FPI sampling locations at approximately 250 km altitude is marked on each figure with a purple star. The PARI site is at the center of these locations marked by a white star. At 00:00 UT post-Sunset recombination is occurring, but the intensification of the geomagnetic storm causes the formation or convection of 60 TECU of plasma into the mid-latitude region, over Florida and the southeastern U.S. The PARI neutral wind measurement sites straddle the northern boundary of the enhancement. By 04:00 UT the enhancement is still about 60 TECU but does not appear to have co-rotated perfectly, and is over the Gulf of Mexico west of Florida. By 06:00 UT, the TEC enhancement has
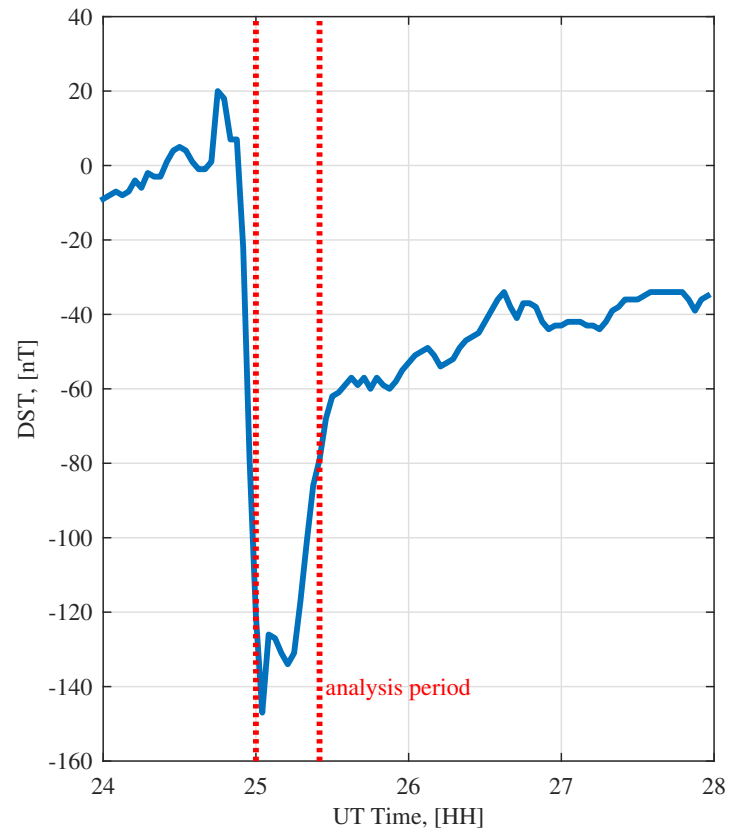
Figure 4.3. Provisional Dst index during the storm period under investigation [3]
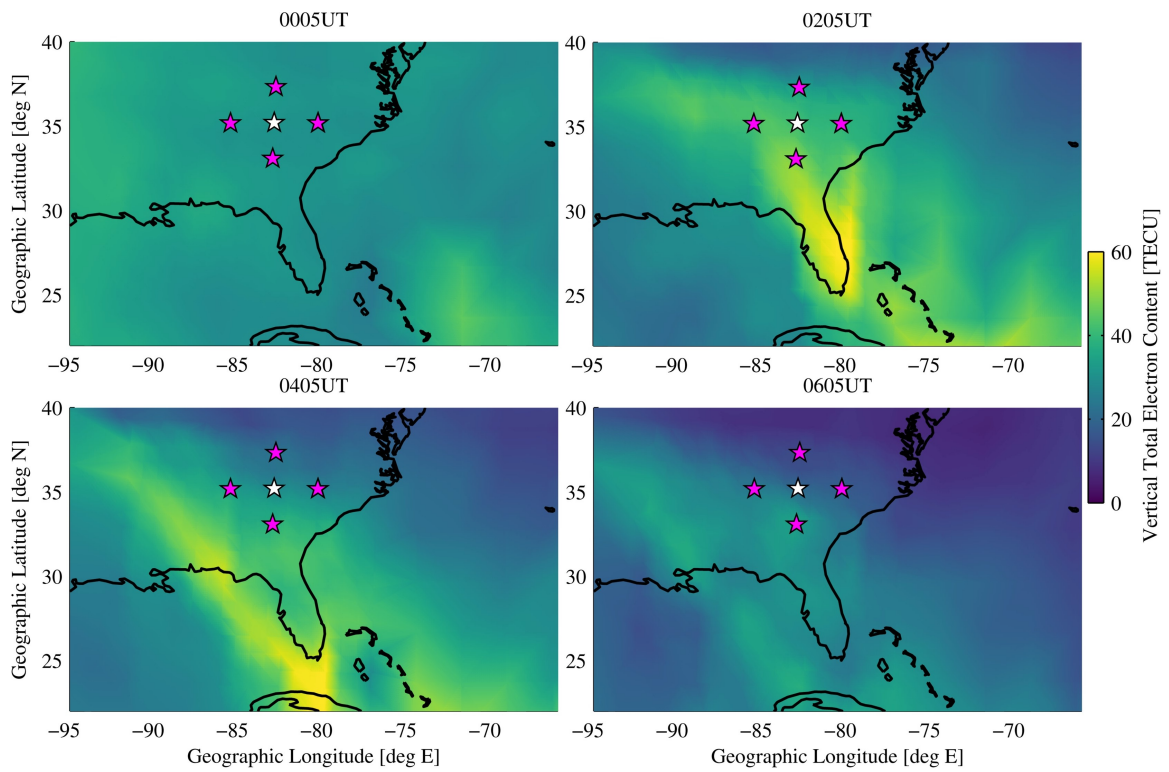
Figure 4.4. TEC maps at 1-degree resolution over southeastern U.S. A post-dusk localized TEC enhancement is visible over the Gulf of Mexico [3]

diminished to less than 40 TECU, with background nighttime plasma of less than 20 TECU.

The orders for the power series fits of the EMPIRE corrected terms are selected to be relatively low order. For $\delta u_{uN}$ and $\delta u_{uE}$ I chose $k_{max}, l_{max}, p_{max}$ to be equal to 3, 3 and 3 respectively. The electric potential is a power series of the equatorial radius of the field line that identified at a given grid point and the longitude. This makes $l_{max} = 0$, but $k_{max}$ and $p_{max}$ are 5 and 6 respectively. The state vector is then a total of 170 elements long with 48 of them being coefficients for electric potential $\delta V$, 64 for $u_{uN}$ and another 64 for $u_{uE}$. All three power series expansions have the radial component centered at Earth's center ($R_0 = 0$), the longitudinal component is centered at 0 radians geomagnetic longitude and the colatitude component is centered at the equator ($\theta_0 = \pi/2$). I selected a relatively low degree for the basis function in order to better understand effects from the Kalman filter as well as FPI ingestion.

The state vector is defined by the number of basis functions. In this study I have a length of 170 where 42 of them are for $\mathbf{x}_V$, 64 for $\mathbf{x}_{uN}$ and another 64 for $\mathbf{x}_{uE}$. I chose not to correct production and loss because production is likely negligible as this occurs during local nighttime, and loss may be so as well, given the persistence of the TEC enhancement. Loss alone cannot be constrained to be nonpositive without reformulating the problem as one with inequality constraints, which is beyond the scope of this work.

In order to expose the behavior of FPI ingestion on EMPIRE we desire the corrections to the model be large. One way to do this is to assume quiet geomagnetic conditions for the HWM14 model and allow ingestion of the FPI to make the necessary corrections. This is accomplished by keeping the Ap value at a default value (19 nT) that is half the mean daily Ap value for October 25th 2011 storm.

The Kalman filtering method in EMPIRE requires characterization of the error for each of the background models and measurements. Appendix A.3 describes the model covariance $\mathbf{R}_a$.

The measurement covariance $\mathbf{R}$ consists of the uncertainty in IDA4D electron density rate "measurements" $\sigma_{y_N}$ and, when ingested, FPI neutral wind measurement uncertainties $\sigma_{y_u}$, such that $\mathbf{R}$ is diagonal matrix of variances. The measurements from IDA4D are all assumed independent which is an approximation since IDA4D is itself a tomographic inversion algorithm. IDA4D provides a covariance matrix which I then manually select the diagonal elements from for the purposes of this first Kalman filtering study.

$$
\begin{aligned}
\mathbf{R} &= \operatorname{diag}(\sigma_{y_N,1}^2, \sigma_{y_N,2}^2, \ldots, \sigma_{y_N,i}^2, \ldots, \sigma_{y_N,i_{max}}^2, \\
&\quad (c\sigma_{y_u,1})^2, (c\sigma_{y_u,2})^2, \ldots, (c\sigma_{y_u,i})^2, \ldots, (c\sigma_{y_u,i_{max}})^2)
\end{aligned} \tag{4.11}
$$

The FPI neutral wind measurement error $\sigma_{y_u,i}$ at the $i^{th}$ location is provided with the data set downloaded from the Madrigal Haystack website. These may be scaled by a factor of $c$ that is artificially included for testing the Kalman filter response in the subsequent sections. Similarly, the IDA4D electron density error $\sigma_t$ at time $t$ is provided with the IDA4D data set. The density rate variance $\sigma_{y_N,i}^2$ is determined by the larger variance of the two densities that are time-differenced. This is done to allow relative weighting between subsequent density variances but so the variance does not become too large as compared to FPI and model variances:

$$
\sigma_{y_N,i}^2 = \frac{\max[\sigma_{t_2}^2, \sigma_{t_1}^2]}{(\Delta t)^2} \tag{4.12}
$$

EMPIRE outputs were tested using traditional summation of the variances for IDA4D densities and for the 'as-is' FPI variances. The resulting variances were too large to

make a meaningful adjustment to the background model. Adjustment of variances and weighting to better capture physical storm time dynamics will be a part of future work with EMPIRE.

**4.2.2  Results.** The results are divided into three parts. In Section 4.2.3 we examine the EMPIRE Kalman filter by analyzing the neutral wind estimate's response to FPI ingestion when tuning the FPI variance. In Section 4.2.4 we discuss neutral wind estimation at all four FPI line of sight measurement locations and explore the effect of ingesting only two of those locations. Section 4.2.5 presents FPI measurements of the vertical neutral wind and describes how it indicates that the FPI measurements are partly contaminated. Finally, in Section 4.2.6 we look at how FPI ingestion affects ion drift estimation.

**4.2.3  Demonstration of Kalman Filtering in EMPIRE.** Figure 4.5 shows how FPI ingestion changes EMPIRE estimation at the northern FPI measurement location. The HWM14 background model is shown in green, and the FPI measurements at this location in black with error bars showing the magnitude of $\sigma_{y_u}$. The red line with X markers, labeled "no ingest" (NI), shows EMPIRE estimates using only the IDA4D plasma density measurements to correct the HWM14 model. The EMPIRE estimates that use FPI measurement data are shown as the cyan through magenta lines, for different choices of factor $c$ in Eq. (4.11) for scaling the FPI data uncertainty $\sigma = \sigma_{y_u}$. As the line color transitions from cyan to magenta $c$ becomes smaller, weighting the FPI measurements more heavily in the Kalman filter.

The NI estimate and the $\sigma \cdot 10$ are nearly coincident with one another. In fact, the root mean square of the difference between the NI estimate and the $\sigma \cdot 10$ over the entire 10 hour analysis time comes to 0.47 m/s which is very small and within uncertainty. Multiplying by $\sigma \cdot 10$ has essentially deweighted the FPI measurements to such a point that the resulting estimate is nearly equivalent to using no FPI
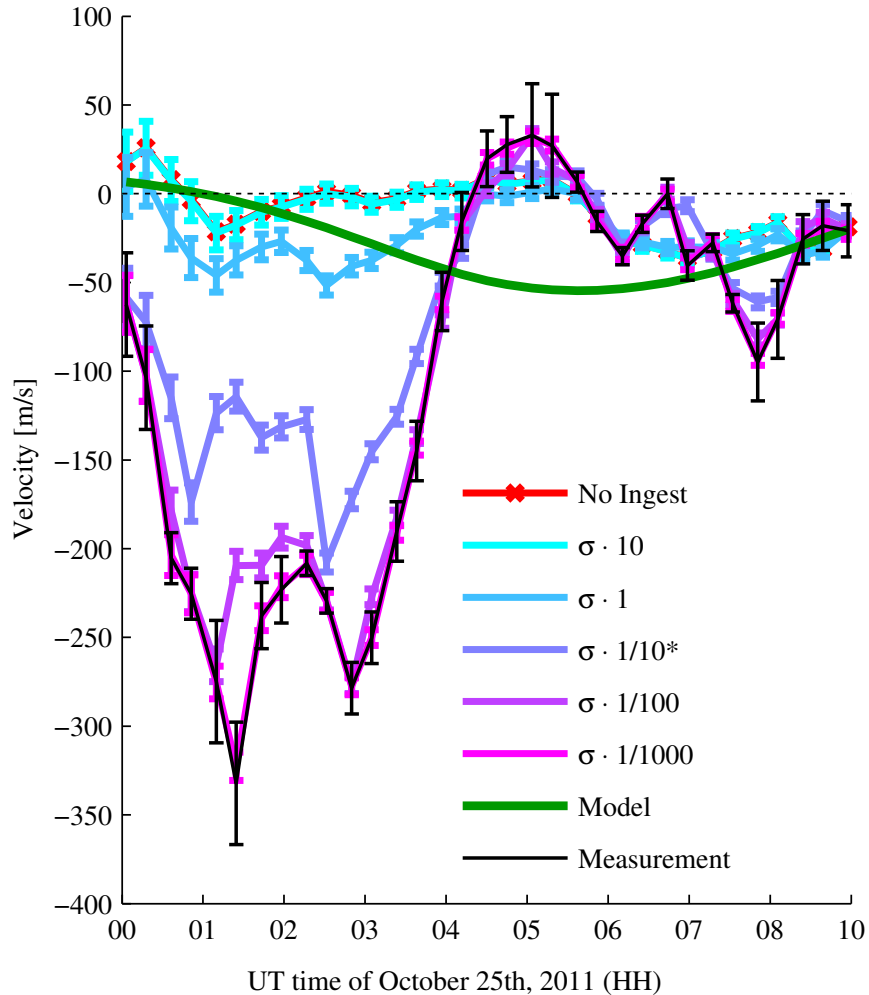
Figure 4.5. Northern facing FPI line of sight neutral wind velocities. The '*' indicates the scaling selected for subsequent analysis [3].

measurements whatsoever.

The $\sigma \cdot 1$ line shows EMPIRE's estimate when the FPI measurements are weighted purely by the uncertainty in the FPI measurements that is provided by the publicly available data set and shown using the error bars in Figure 4.5. If the FPI $\sigma$ is scaled with $c < 1$, the solution curve shifts towards the FPI measurements. This exercise indicates that the Kalman filter works as anticipated, in providing a solution that blends the model with measurement, according to the relative weighting between them.

The scale factor $c$ allows us to control how much the EMPIRE estimates are influenced by the FPI neutral wind measurements. By selecting $c = 1/10$, the FPI measurement's influence on EMPIRE estimation contrasts more strongly with the HWM14 model than would be possible with only the published data covariances. The FPI variances are tuned as opposed to IDA4D and the background models because they are published covariances that have easy access for other researchers to also modify or use as they see fit. Computing IDA4D and background model covariances and weighting is still a subject of continued research. The background model variances/weights could have been adjusted to be larger instead of decreasing the FPI variances and it would have similar effects as decreasing the FPI variances do. We chose to adjust the FPI variances since they are well known and published values compared to IDA4D values and our choice of model.

**4.2.4 EMPIRE Neutral Wind Estimate Validation.**  This section examines three cases, each using a different number of FPI data measurement points, all with $c = 1/10$ used for the FPI data in Eq. (4.11). The "no ingest" (NI) case uses only IDA4D-derived electron densities without any FPI measurements. The "half ingest" (HI) case uses two FPI measurement locations (i.e., north and west LOS directions) and the IDA4D-derived electron densities, and the "full ingest" (FI) case uses all four of the FPI data measurement locations along with the IDA4D-derived electron densities. For the HI case, the north look direction was chosen mainly because it has the largest winds and the western direction was chosen as a perpendicular LOS direction. Having ingested larger winds causes EMPIRE to apply larger corrections. Ingestion of south and east was also tested but is not shown. Other pairs (N-E or S-W) would not span the TEC enhancement shown in Fig 4.6, or in the case of (N-S or E-W) would not sample both meridional and zonal wind directions.

Figure 4.6 shows how FPI ingestion affects the EMPIRE estimation at all four

FPI line of sight measurement locations. Plotted are the line-of-sight neutral winds, positive away from the FPI, as modeled by HWM14 (green), measured by FPI (red), and estimated by EMPIRE. There are three sets of EMPIRE estimates in each figure: NI (light blue), HI (medium blue), and FI (dark blue). The results corresponding to Figure 4.5 are reprinted in Figure 4.6(a) as the model, measurement, NI, and FI lines.

The HWM14 results show an easterly wind beginning at 00 UT. As time progresses the wind turns southward, eventually having almost completely southward flow at around 06 UT. The FPI measurements indicate quite different conditions. Unlike the model, the western and eastern measurement directions show westerly winds that are in stark disagreement with the model. The north and south measurement directions show an interesting feature: the northern site indicates strongly southward flow, particularly from 00 to 05 UT. The southern site shows very little wind with brief periods of northward wind. The north direction measuring a strong southward wind and the south direction measuring a slight northward wind would indicate a convergence is occurring. See Section 4.2.5 for a discussion on the possible reasons for the resolved convergence. The comparison between the HWM14 model and data indicate that the thermospheric state has significantly changed from the quiet time conditions represented by HWM14.

The NI results stay near the model for the east and west directions. From 00 to 05 UT the north and south NI estimates stay closest to the model compared to HI and FI. After 05 UT, the NI result does a better job than HI and FI with estimating the measured north and south winds, for the most part falling within the error bars of the measurements. The improved agreement with FPI data from 05 to 10 UT is notable, given that *only* electron density rates are being assimilated in this case. The ion continuity equation relates only the field aligned neutral winds to changes in field
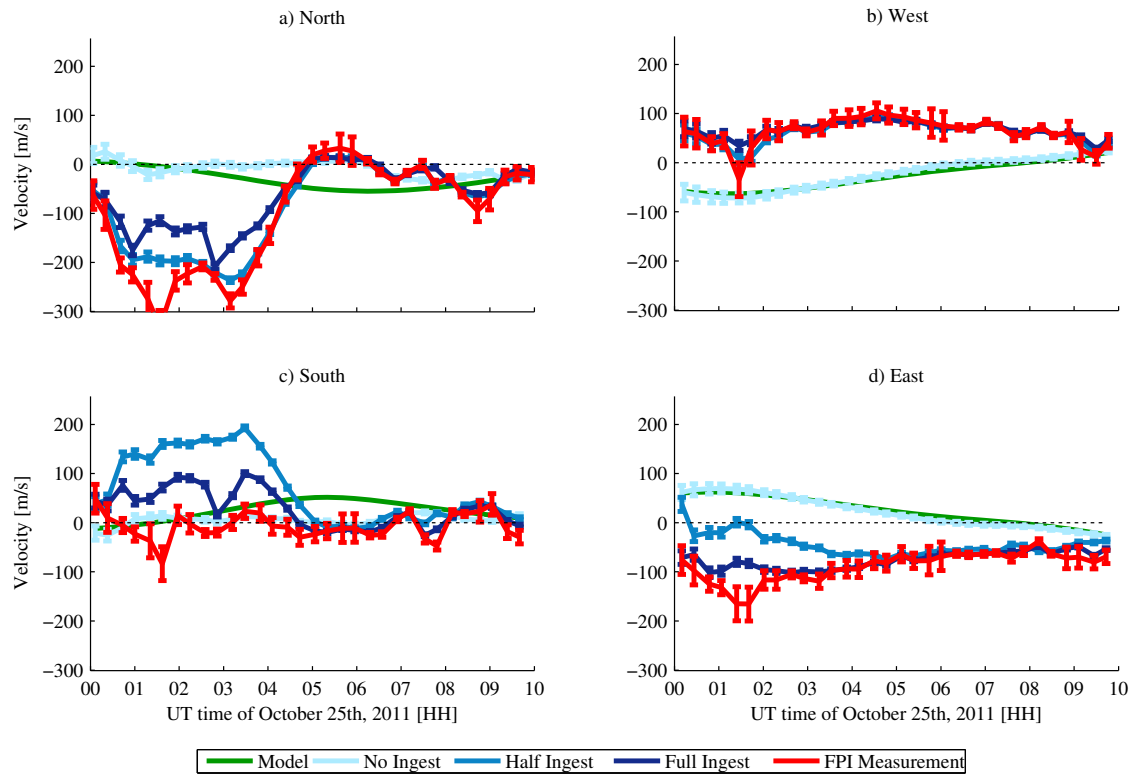
Figure 4.6. FPI measured line of sight component to neutral winds as produced by the HWM14 model, FPI measurements themselves, and EMPIRE estimates for three separate runs: no ingest, half ingest and full ingest. Each subplot corresponds to one of the different FPI line of sight measurement locations[3].

aligned ion drifts. Also, the north and south LOS directions are closer to the field aligned direction than the east and west are because the magnetic field declination angle varies from 1 degree to -11 degrees from the geographic north direction and the dip angle between 52 and 66 degrees from horizontal. This is why there are larger adjustments to the meridional directions than the zonal directions.

Also shown in Figure 4.6 is the HI set of EMPIRE estimates. The purpose of ingesting half of the data is to examine how ingestion of the north and west data affects the estimates in the south and east, whose FPI measurements can then be used for comparison. The HI results at the north and west locations (Figures 4.6(a) and (b)) are closer to the FPI measurements than the model, NI, and the FI cases are. However, for the south directions the HI case disagrees with the FPI measurements even more than the model or NI case and only does from 00 to 05 UT. After 05 UT, the HI and NI cases both have similar solutions. East results indicate an improved comparison between data and the HI case, as compared to the model or NI case. Very good agreement is seen after 05 UT. The south and east HI estimates are being heavily influenced by the north and west directions because of heavy weighting of FPI measurements (of which only the north and west are being considered) as compared to the HWM14 model and IDA4D. The resulting powerseries from the heavy weighting of the FPI measurements in the north and west does not have enough distance ( 500km) to readjust to the green model or IDA4D derived neutral winds. For the FI case the large negative velocities in the north are driving the southern locations to still remain away from the FPI measurements because of a 'stiffness' in the chosen power series.

The north and west's influence on the south and east can be seen in Figure 4.7, which shows HI estimates plotted for all four measurement locations on a single figure. For the north (solid blue) and west (solid red) directions, positive speeds are away from the FPI. Assuming that the vertical winds are negligible, the south and

east EMPIRE HI estimates shown in Figures 4.6(c) and (d) can be multiplied by -1 to make positive speeds also northward and westward (Figure 4.7 dashed lines).

The north and west estimates, whose FPI measurements are ingested, dictate the trend that the winds in the south and east will follow. Any deviation from this trend is due to influences from IDA4D, the models, and the order of the power series basis function only, as EMPIRE also assumes zero vertical velocity. As the order of the power series basis function increases it will allow for more flexibility in the result. If an infinite number of basis functions could be used then the solution can adjust as needed anywhere such that a the exact balance set by covariances and weighting of FPI, IDA4D and model could be reached. The neutral winds estimated by EMPIRE that drive the IDA4D ion density drifts do not produce a neutral wind gradient that is capable of matching the large north-south gradient measured by the FPI. This explains why, in Figure 4.6, the south and east EMPIRE HI estimates disagree with the measurements from 00 to 05 UT. A probable explanation for why IDA4D and the models do not produce such a gradient is because the winds being measured by the FPI are not representative of the actual thermospheric winds as Section 4.2.5 will discuss.

When all four measurement locations are ingested in EMPIRE the FI estimates trend closer to the FPI measurements in all four measurement locations except for the northern location. The relatively slower winds measured and ingested in the south is influencing the solution in the north enough to increase disagreement between FI estimates and the FPI measurements. In the north direction, the very large negative LOS winds measured around 01:30 UT correspond to strong southward winds. At the same time (01:30 UT), the FPI measurements in the south direction are negative winds which correspond to northward winds. The FPI is therefore measuring an apparent wind convergence across the TEC enhancement that EMPIRE never fully
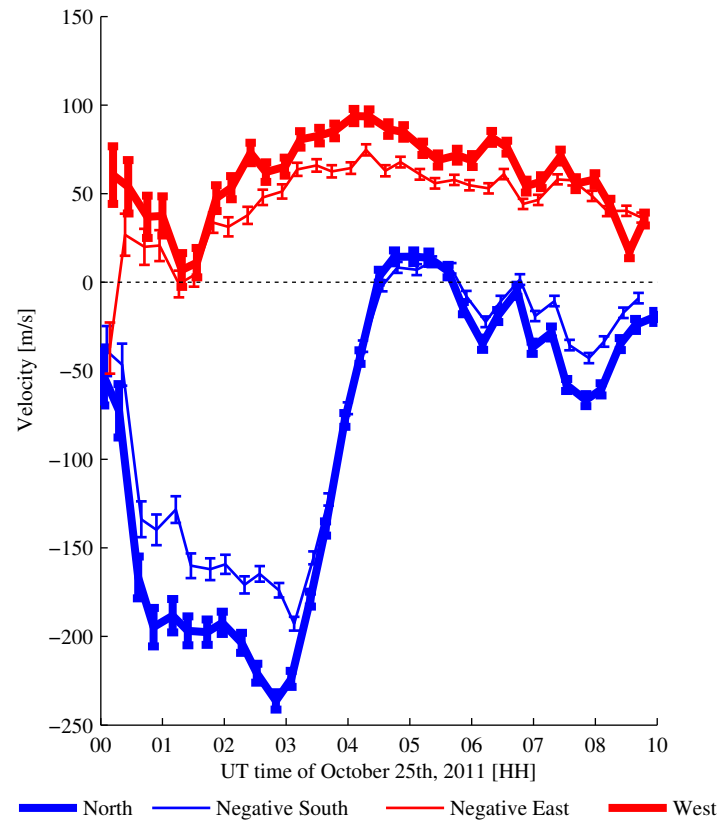
Figure 4.7. EMPIRE estimated winds based on ingesting the north and west locations. The south and east measured speeds are scaled by -1, so that positive speeds on the plot indicate northward and westward speeds, respectively [3] .

captures even with increased weighting on the ingested FPI data. The disagreement between EMPIRE full ingest estimates in the north and south to the FPI measurements between 00 and 05 UT can therefore be attributed to EMPIRE disagreeing with the large spatial gradient of velocity that is measured by the FPI.

**4.2.5 Possible Evidence for the Effects of Contamination in the Redline Emission.** In the HI case, in which wind measurements from the north and west were ingested into the algorithm, EMPIRE estimates for the southern and eastern LOS directions significantly disagree with the FPI measurements from 00 to about 05 UT. After this time, the EMPIRE estimated winds and those measured agree quite well.

EMPIRE's Eq. (4.3) relating FPI measurements to neutral winds assumes that the FPI measurements are indicative of the thermospheric, and only thermospheric, winds at the intersection point of the instrument's line of sight and the assumed emission altitude of 250 km. However, [45] presented evidence that the measured redline emission at midlatitudes during storm conditions can be complicated by the presence of non-thermal O, meaning that the derived winds and temperatures from the instrument are no longer representative of thermospheric wind. Alternatively, similar effects on the estimated neutral winds have been hypothesized due to atmospheric scattering in the presence of a strong spatial gradient in the emission intensity [46], as is the case on this night. The primary signature indicative of either contamination source is the appearance of unrealistic, downward apparent winds. Under typical conditions, the vertical wind in the thermosphere is quite small, with a magnitude less than 10 m/s.

To investigate whether "contamination" is present for the 24-25 October 2011 storm, we present the estimated vertical wind from the PARI FPI in Figure 4.8 as the red error bar lines. The period from approximately 00 to 05 UT shows evidence
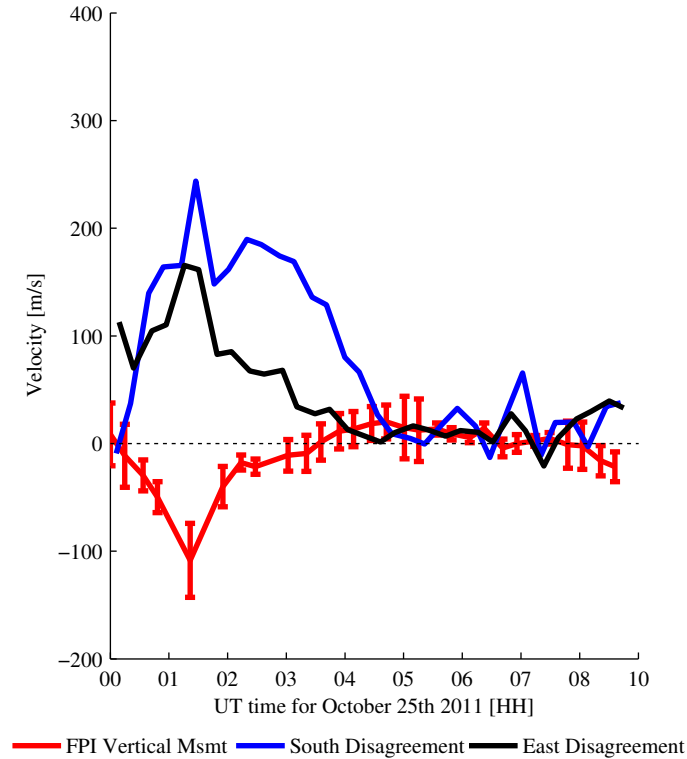
Figure 4.8. FPI vertical winds, the difference between EMPIRE half ingest results and FPI measurements for the measurement directions versus UT hour [3].

of large (peaking at 100 m/s) apparent downward winds, which is likely evidence of the contamination. The south and east directions (Fig. 4.6(c) and Fig. 4.6(d)) were not ingested into EMPIRE in the HI case. From about 00 to 05 UT the largest disagreement with the measured winds coincides with the vertical wind indication of contamination.

Our explanation for the inability of EMPIRE to predict north and west winds from 00 to 05 UT is that the measured velocities from the FPIs during this period are not indicative of solely thermospheric wind. This means the data assimilation method's assumption that FPI measurements are thermospheric winds is no longer valid. Once the contamination goes away after 05 UT, the measured and estimated winds begin to agree, suggesting that the FPI measurements are once again indicative of thermospheric wind.

For the "full-ingestion" case, the EMPIRE Kalman filter is then trying to simultaneously adjust the estimate to non-thermospheric measurements in all four directions. The EMPIRE estimate's disagreement with the FPI measurement can, therefore, be attributed to contamination in addition to the thermospheric motion during the period between 00 to 05 UT.

**4.2.6 Ion Drift Estimation.** With the caveat that the previous section showed the result of ingesting "contaminated" FPI data from 00 to 05 UT, in this section we review the effect the FI and HI cases have on ion drift estimates. Figure 4.9 shows EMPIRE's ion drift estimates at the north FPI LOS location with the three components of ion drifts: field-perpendicular in the zonal (positive eastward) direction (4.9(a)), magnetic field-parallel (4.9(b)), and field-perpendicular in the meridional plane of the field line (4.9(c)). There are 4 lines in each subplot: three lines representing each of the ingestion cases, and the background model (Weimer 2000 and IGRF-11 models.) as the green line.

The field-perpendicular zonal and meridional ion drift velocities shown in Figure 4.9 are insensitive to FPI ingestion, as seen by the lack of difference between NI, HI, FI, and model curves. Not shown here, EMPIRE corrections for the analysis region at north and western longitudes (away from the FPI measurement locations) are much larger. The first possible reason is that the Weimer model is returning negligible electric potential because the convective two cell region has retreated poleward, giving near-zero background model ion drifts at latitudes equatorward of the northern FPI location ($\sim 37.3°$ N). EMPIRE estimating zero corrections to Weimer's predicted zero ion drift is therefore leaves EMPIRE's results reasonable. Also, the relatively large uncertainties on IDA4D-based density rates (median covariance value is 210%), which are the only measurements providing observability of the $\mathbf{E} \times \mathbf{B}$ drifts, means that EMPIRE corrections will tend to be small. IDA4D electron den-
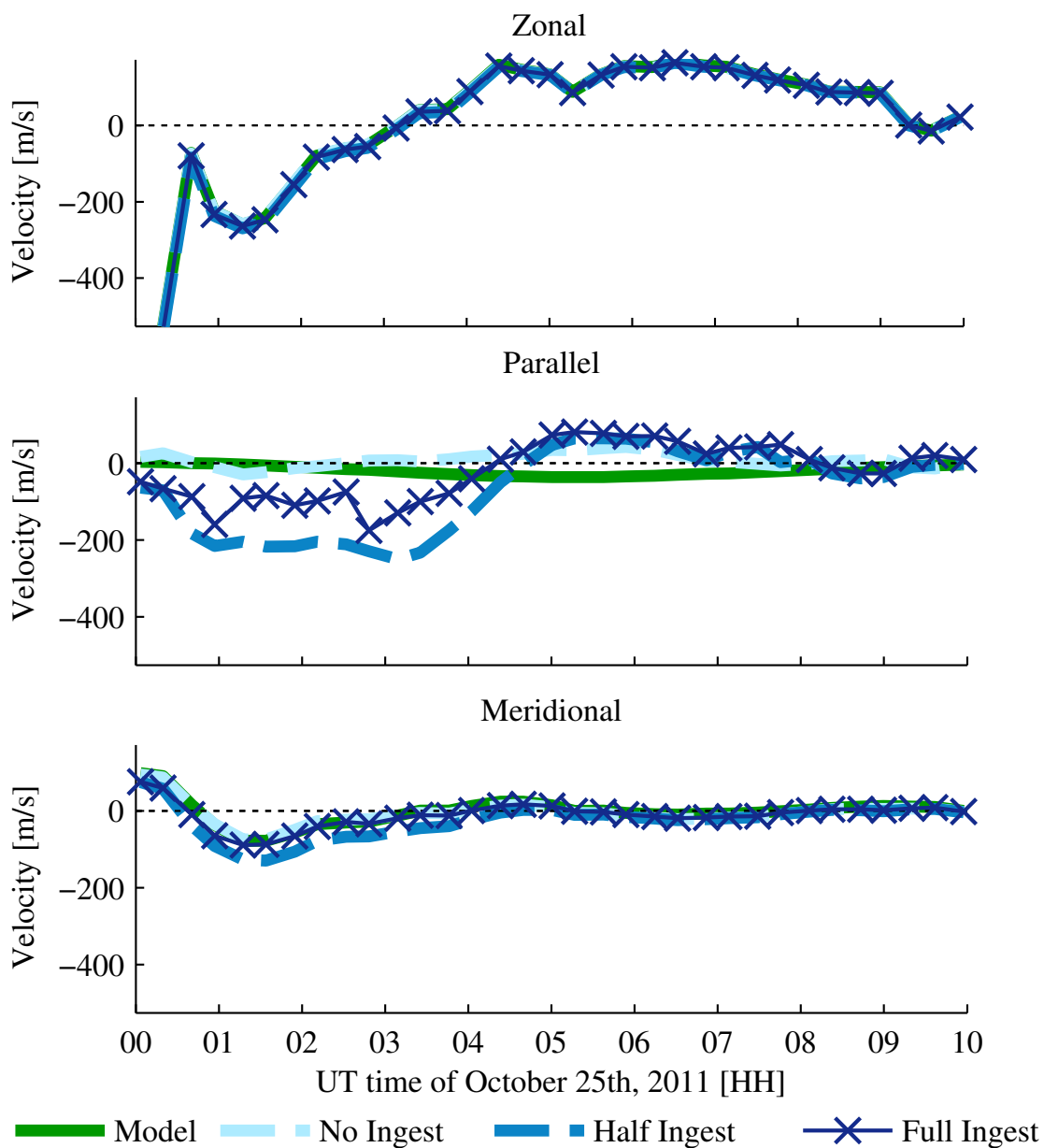
Figure 4.9. Field-aligned ion drift velocity estimates and model estimates for the northern FPI LOS measurement location [3].

sity standard deviations are on the order of 30-40% but because we finite difference the data is made even more noisy.

The reason the parallel direction remains sensitive to FPI neutral wind ingestion may be attributed to the physics described by the ion continuity equation. Equation (2.18) assumes that the dominant term in the field perpendicular direction is $\mathbf{E} \times \mathbf{B}$ drift. In contrast, in Eq. (2.18), ion motion in the field-parallel direction is influenced by neutral winds, gravity and diffusion. This essentially decouples the physical drivers, so ingestion of FPI neutral wind measurements mostly affects EMPIRE ion drift estimation in the field-parallel direction only. From 05 to 10 UT, the NI, HI, and FI solutions estimate similar field-parallel drifts, i.e., northward and downward. During the 00 to 05 UT interval, anti-parallel, namely upward and southward,drifts are estimated by EMPIRE when ingesting the FPI data. Although from 00 to 05 UT the FPI vertical LOS detects significant negative (downward) speeds, indicating contamination [45], the southward drifts are corroborated by the IDA4D density maximum at the longitude of PARI drifting southward particularly after 02 UT.

**4.2.7 Conclusion.** EMPIRE has been successfully adapted for ingesting neutral winds using a Kalman filter technique. By using the ion continuity equation to define the required measurements and models we have estimated the neutral wind state over the southeastern United States during the 24-25 October 2011 storm. The use of Kalman filtering with EMPIRE allows the solution to be sensitive to covariances of models and measured FPI data. Characterization of the EMPIRE estimates based on data provided by FPI neutral wind measurements and IDA4D-derived plasma densities shows that, at the location of the FPI measurements, the EMPIRE neutral wind estimates favor FPI measurements. EMPIRE estimates away from the measurement locations improve, but have difficulty matching the large north-south neutral

wind gradient measured across the storm-induced nighttime plasma enhancement. Ion drift estimation in this region shows sensitivity to FPI ingestion in the magnetic field parallel direction.

The results presented in Section 4.2.5 add to the supporting evidence for contamination of the stormtime, midlatitude redline emission. Developing an understanding of how to handle this contamination in FPI measurements and how to best leverage physical models for data assimilation are both part of ongoing work.

Given that FPI ingestion proved useful, efforts are under way to generalize assimilation of FPI data. More FPIs will allow for improved estimation over entire regions that encompass structures such as the one shown in Figure 4.4. Future development of EMPIRE will also make use of techniques described by [47] to estimate the airglow altitude distribution. Also the effects of increasing the degree of the polynomial while maintaining an adequately overdetermined system is also still a matter of investigation. This could allow for more optimal results with a balance between run time, error and resolution.

CHAPTER 5

GLOBAL ELECTRIC POTENTIAL ESTIMATION

Previously, EMPIRE was designed to produce estimates regionally. While this can be very useful, many phenomena associated with the IT system drivers involve global processes. In order to capture these processes EMPIRE must use methods suitable for global inversion and reconstruction. This section begins by introducing two primary global phenomena of the IT system and then introduces how EMPIRE has been modified to estimate the electric potential driver on a global scale.

## 5.1 Global Phenomena Associated with the IT System

Global phenomena within the IT system typically involve the transport of energy and mass from high to low latitudes and from day to night longitudes. Energy can enter the Earth's ionosphere from the upper boundary ($\sim$1000km). When a coronal mass ejection (CME) is directed toward Earth, the collision between the solar wind and Earth results in an exchange of energy that ultimately results in an observable change in energy (i.e., neutral wind and ion drift velocity) throughout the IT system [23]. Similarly, intense tropospheric storms (i.e., hurricanes) and seismic activity can propagate energy up through the lower boundary (80km) (cite Komjathy) through gravity waves.

The energy in the thermosphere (i.e., neutral gas) can transfer to the ionosphere (i.e., ionized gas) through collisional drag as was explained in Chapter 2. As the ionosphere is accelerated by electric fields during intense geomagnetic storms, it collides with neutral winds resulting in abrupt changes in neutral wind speeds. Similarly, propagating waves within the thermosphere can accelerate ions during both geomagnetically quiet and active times. One of the challenges in understanding the

thermosphere-ionosphere coupling is the ability to capture ionospheric drivers globally. In particular the neutral-wind dynamo effect is an area of great interest within the scientific community.

The neutral wind dynamo describes the collisional interaction between the thermosphere and ionosphere. It is characterized by an acceleration of ionospheric drifts in response to thermospheric winds. Energy deposited into the thermosphere can originate anywhere globally and the dissipation can result in the disturbance reaching around the entire globe. The acceleration of thermospheric winds during geomagnetic storms typically occurs at high latitudes during geomagnetic storms. The thermospheric kinetic energy then dissipates by propagating to low latitudes with slow moving and large gravity waves . It is possible to observe ion and thermospheric accelerations up to 48 hours after storm onset due to the neutral wind dynamo [48]. Understanding the neutral wind dynamo will require an assimilation algorithm that provides estimates of the neutral wind globally during geomagnetic quiet and active periods. With this motivation, the next section describes how EMPIRE is extended from a regional assimilation algorithm to global algorithm.

## 5.2  Basis Functions for Global Estimation of Electric Potential

EMPIRE estimates a best-fit basis function to represent corrections of physical drivers. In order to estimate a function that spans the entire globe the function must be continuous on a spherical domain such as Earth. Previously, EMPIRE was designed with power series basis functions [14, 15, 16, 3]. While power series basis functions are easy to implement, they are not continuous on a spherical domain and are not orthogonal to one another. Spherical harmonic basis functions, on the other hand, are well documented and used widely for fitting to data that is spatially distributed on a sphere. I chose to implement spherical harmonic basis functions within EMPIRE primarily to eliminate the discontinuity that power series basis functions

have on the -180, 180 degree longitude boundary.

Modification of EMPIRE for use with spherical harmonics basis functions to estimate electric potential requires changing its measurement model. The full derivation is laid out in Appendix B and has two main parts. The first part is the definition of the basis function $\delta V$ and the second is mapping from the basis function coefficients $\mathbf{x}_{lm}$ to $\vec{E} \times \vec{B}$ drift ion convection (defined as $\delta \mathbf{a}_{exb}$). The definition of the independent variable $\ell$ constrains the electric potential to a field line and therefore reduces the electric potential to a function of two independent variables.

$$\delta V(\ell, \phi) = \sum_{l=0}^{L} \sum_{m=0}^{l} P_l^m(\ell) \Phi_l^m(\phi) \tag{5.1}$$

$\Phi_l^m(\phi)$ is defined as:

$$\Phi_l^m(\phi) = [x_c^{lm} \cos(m\phi) + x_s^{lm} \sin(m\phi)] \tag{5.2}$$

$\ell$ is defined as:

$$\ell = -1 + \frac{-2}{L_{min} - L_{max}} L_{min} + \frac{2}{L_{max} - L_{min}} L \tag{5.3}$$

and $L$ is a variable that refers to surfaces consisting of all field lines having the same magnetic field strength at the equator, and is defined as:

$$L(r, \theta) = \frac{(r + R_e)}{R_e \sin^2(\theta)} \tag{5.4}$$

$P_l^m$ is the Legendre polynomial shown in the appendix as equation (B.4) and $\Phi_l^m(\phi)$ contains the harmonic term which is a function of longitude as well as the coefficients. If the coordinate system ($r$, $\theta$ and $\phi$) is defined as the geomagnetic coordinate system the centered dipole approximation of Earth's magnetic field may be used to define the $L$-shell Equation (5.4) above. The consequence of defining the spherical harmonic

as a function of $\ell$ and $\phi$ means that the electric potential is constant along dipole magnetic field lines. The scaling from $L$-shell to $\ell$ allows the domain to span from -1 to 1 thereby preserving orthogonality of the Legendre polynomials.

Now I will summarize what is necessary to map from coefficients $\mathbf{x}_V$ of the spherical harmonics to $dN/dt$. To map $\delta V$ to $dN/dt$ the observation matrix $\mathbf{H}_V$ has to be constructed to fit within the EMPIRE linear system shown in Section 2.2.2. Returning to the definition of Kalman filtering measurement model (See Section 2.2.1 and Figure 2.5):

$$\mathbf{z} = \mathbf{Hx} = \delta\mathbf{a}_{exb} + \delta\mathbf{a}_u \tag{5.5}$$

Recall we assume the measurement bias $\boldsymbol{\nu}$ is equal to zero. The observations are defined as:

$$\mathbf{z} = \begin{bmatrix} \mathbf{z}_{dNdt} \\ \\ \mathbf{z}_u \end{bmatrix} = \begin{bmatrix} \mathbf{y}_{dNdt} \\ \\ \mathbf{y}_u \end{bmatrix} - \begin{bmatrix} \mathbf{a}_0 \\ \\ \mathbf{a}_u \end{bmatrix} \tag{5.6}$$

$$\mathbf{H} = \begin{bmatrix} \mathbf{H}_N \\ \\ \mathbf{H}_u \end{bmatrix} = \begin{bmatrix} \mathbf{H}_V & \mathbf{H}_{uN} & \mathbf{H}_{uE} \\ \\ \mathbf{0} & \tilde{\mathbf{H}}_{uN} & \tilde{\mathbf{H}}_{uE} \end{bmatrix} \tag{5.7}$$

$$\mathbf{x} = \begin{bmatrix} \mathbf{x}_V \\ \\ \mathbf{x}_{uN} \\ \\ \mathbf{x}_{uE} \end{bmatrix} \tag{5.8}$$
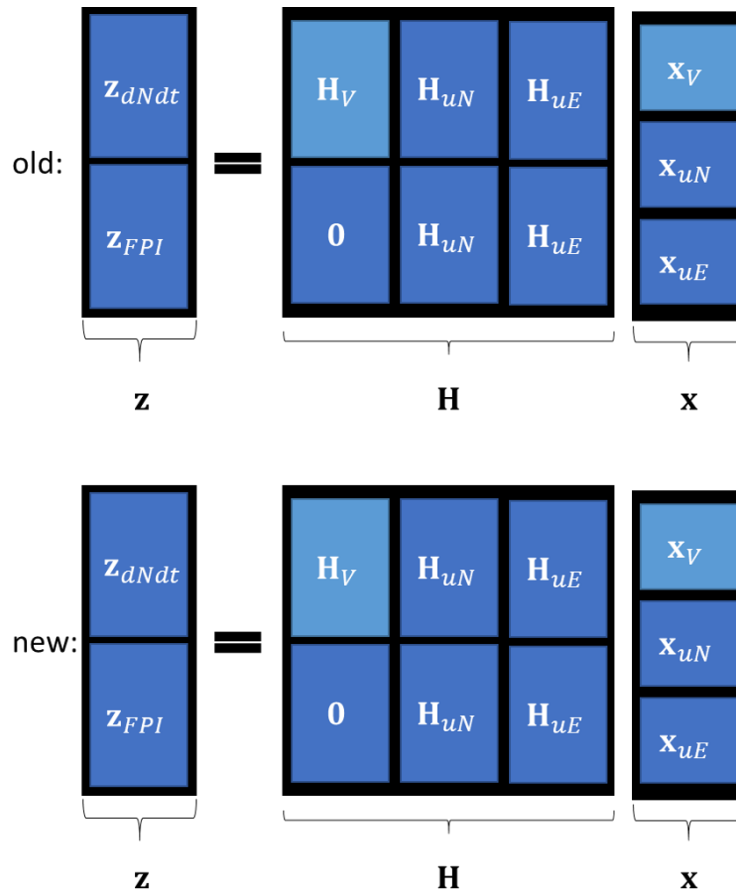
Figure 5.1. EMPIRE measurement model changes that occur due to changing the electric potential basis functions. The mapping matrix $\mathbf{H}_V$ and the coefficients $\mathbf{x}_V$ are affected.

When the expanded form is placed together the measurement model looks like:

$$\begin{bmatrix} \mathbf{y_N} \\ \mathbf{y_u} \end{bmatrix} - \begin{bmatrix} \mathbf{a}_N \\ \mathbf{a_u} \end{bmatrix} = \begin{bmatrix} \mathbf{H}_V & \mathbf{H}_{uN} & \mathbf{H}_{uE} \\ \mathbf{0} & \tilde{\mathbf{H}}_{uN} & \tilde{\mathbf{H}}_{uE} \end{bmatrix} \begin{bmatrix} \mathbf{x}_V \\ \mathbf{x}_{uN} \\ \mathbf{x}_{uE} \end{bmatrix} \tag{5.9}$$

The measurement model terms above that are changed include $\mathbf{M}_V$ and $\mathbf{x}_V$. This is illustrated using the light blue blocks in Figure 5.1. The coefficient array $\mathbf{x}_V$ now contains two sets, one for sine and the other for cosine. The derivation of $\mathbf{H}_V$ is found

in Appendix B and starts with the expression for $\delta\mathbf{a}_{exb}$ shown below.

$$\delta a_{exb} = -\vec{\nabla} \cdot (N \delta\vec{v}_{\perp}) = -\vec{\nabla} \cdot \left( N \frac{-\vec{\nabla}\delta V \times \vec{B}}{B^2} \right) \tag{5.10}$$

Derivation of the above equation requires three operations to be applied to the basis functions $\delta V$ shown below:

1. The gradient: $-\vec{\nabla}$ to form the electric field $\vec{E}$

2. The cross product: $-\frac{1}{B^2}\vec{\nabla}\delta V \times \vec{B}$ to form the ion drift $\delta\vec{v}_{\perp}$

3. The divergence: to form the $\vec{B}$-field perpendicular ion convection

The definition of $\mathbf{H}_V$ completes the measurement model (See Appendix B for full derivation to see the steps carried out above).

**5.2.1 Testing the implementation of spherical harmonics.** The definition of $\delta V(\ell, \phi)$ to be a function of $\ell$ and $\phi$ allows for the electric field to vary along geomagnetic field lines and longitude. It is possible to check if this constraint on the magnetic field line is working properly by plotting $\delta V$ on a 2D slice in longitude so a single meridian is shown. Figure 5.2 shows the grid used to compute a 2D slice of electric potential. The basis functions were fit using measurement and model data from the March 17th 2015 St. Patrick's Day Storm and is at a similar longitude to an ISR located at the Millstone Hill Observatory. Details on the datasets and the geomagnetic storm can be found in Chapter 6. Figure 5.3 shows the the electric potential corrections plotted at the grid points from Figure 5.2. The results show that the electric potential is varying with geomagnetic field line only as the field lines are shown to have constant values. This demonstrates the behavior of the basis functions and shows that they produce electric potentials that are constant along a field line.
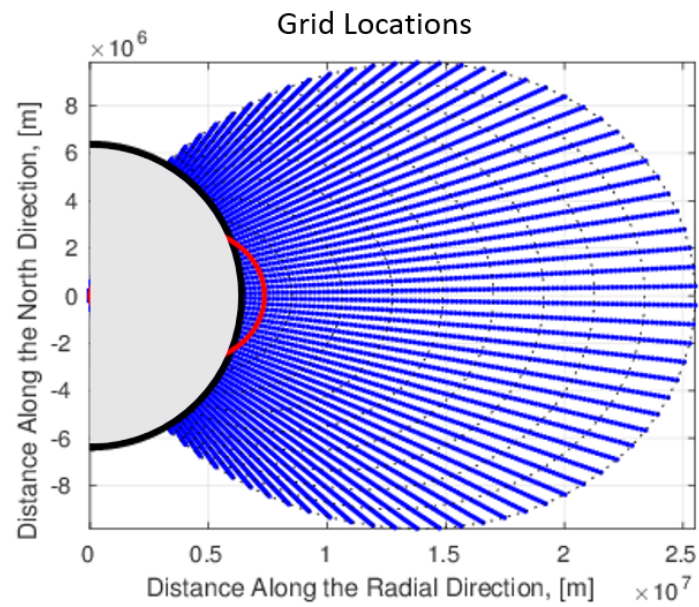
Figure 5.2. A half circle representing a spherical Earth is drawn in black with a red line showing a single dipole field line that corresponds to 250km altitude and 53 degree latitude. The blue dots are the specified grid points used to reconstruct the electric potential values. Also plotted with thin dotted lines are geomagnetic field lines. The y and x axes are both in meters.
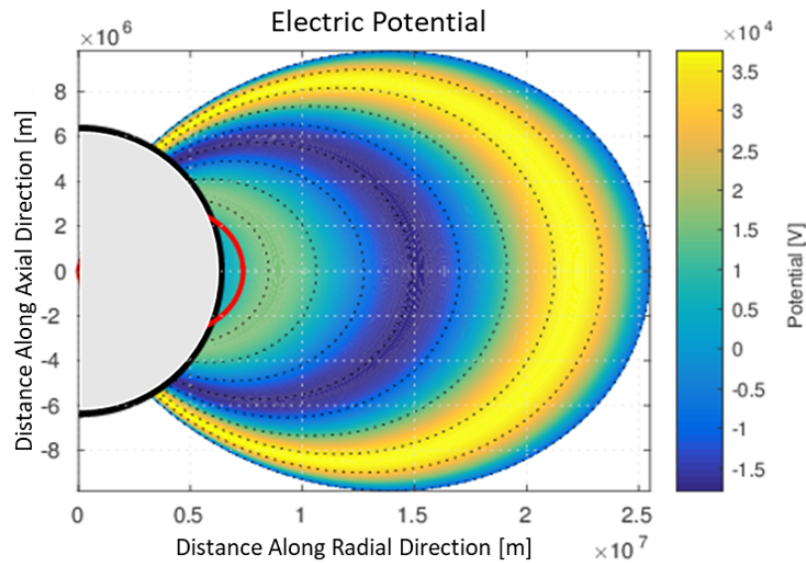
Figure 5.3. A half circle representing a spherical Earth is drawn in black with a red line showing a single dipole field line that corresponds to 250km altitude and 53 degree latitude. Also plotted is the thin dotted lines which represent geomagnetic field lines. The y and x axes are both in meters.

The main purpose of choosing spherical harmonics is to have continuous solutions on a spherical domain. To show that the spherical harmonics are continuous I have plotted in Figure 5.4. The red dashed line locates the -180/180 boundary and shows that EMPIRE's solution is continuous. This figure also shows the shape of the spherical harmonic functions estimated by EMPIRE for the given time step.

Not shown here, as EMPIRE changes its grid the solution also changes. This is expected as the data that is being ingest also changes but when the grid is greater than 60-70 degrees latitude a different effect influences the solution more dramatically. This is due to the use of a dipole magnetic field model. EMPIRE uses the dipole magnetic field model to constrain its electric potential results to be constant along the field line. Earth's magnetic field can be modeled as a dipole to first order, however, as the distance from Earth increases the dipole magnetic field weakens and becomes more distorted by the interplanetary magnetic field that is produced from the Sun and by

the solar wind [23]. As such, modeling the electric potential as constant along a dipole magnetic field becomes inaccurate around geomagnetic latitudes of 60-70 degrees. At higher latitudes than this, the L-shells extend beyond the distance which the dipole field model holds (L-shell of 10). Also, the magnetic field lines at high latitudes are 'open' meaning they connect with the interplanetary magnetic field.

Demonstrating the effects this has on the EMPIRE solution is not trivial but it is summarized here. The effects of using the dipole field model is that the solution across the globe changes drastically as the grid changes from $87°$ to about 65 $°$. The requirement of $\delta V$ to be parameterized by $\ell$ (scaled L-shell) and longitude ($\phi$) essentially creates an non-uniform sampling in the Legendre space. Legendre space is what I call the domain EMPIRE uses to fit the electric potential basis functions, [-1 to 1]. This is an important realization for the way EMPIRE is formulated and is why EMPIRE's grid kept at geomagnetic $30°$ to 150 $°$ colatitude in the study that is conducted later in Chapter 6. Modeling the electric potential as a function of $\ell$ and $\phi$ simplifies the implementation drastically.
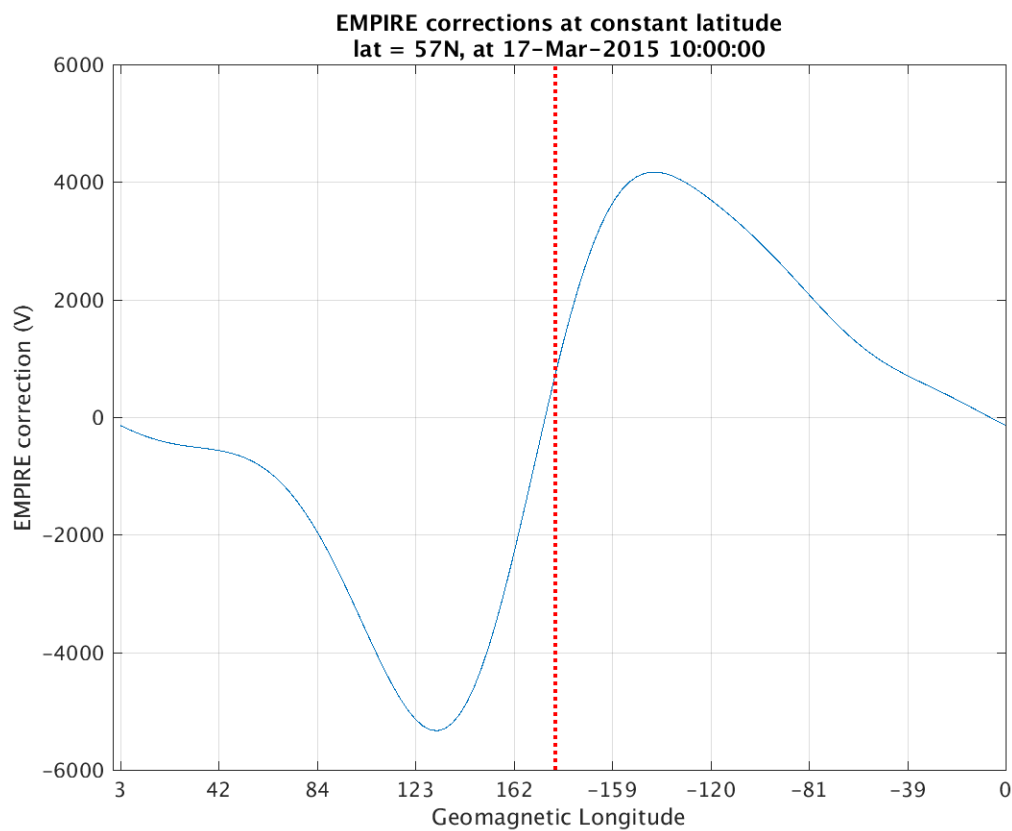
Figure 5.4. EMPIRE electric potential correction estimates plotted at 57° N latitude from -180 to 180. The red line marks the location of the -180/180 boudnary.

CHAPTER 6

A STUDY OF THE SUB-AURORAL POLARIZATION STREAM WITH EMPIRE

Global phenomena within the ionosphere-thermosphere (IT) system typically involve the transport of energy and mass between high to low latitudes and between day to night longitudes. It is typical that equatorward neutral wind surges occur during geomagnetic storms occur at midlatitudes. At high latitudes momentum and energy between the ionosphere and thermosphere are intensified during storm time, and that energy dissipates equatorward. This equatorward surge is particularly visible at mid-latitudes [49].

Occasionally meridional equatorward surges do not occur during geomagnetic storms. Storm-time winds can turn poleward typically following a midnight or post-midnight equatorward surge as seen at the Millstone Hill (MH, 42.6° N, 71.5° W; geodetic) observatory [50]. In the premidnight sector the disturbances are generally weak and equatorward but occasionally have brief poleward turning that is sometimes due to traveling atmospheric disturbances (TADs) [51].

During severe a geomagnetic storm [5] identified an 'anomalous' premidnight poleward meridional surge that persisted for several hours during the 17-18 March 2015 severe geomagnetic storm. They attributed the poleward surge to the sub-auroral polarization stream (SAPS) flow. SAPS is a magnetosphere-ionosphere coupling process located in a relatively narrow region of low conductivity between the auroral precipitation zone and the plasmasphere boundary layer [52]. Intense SAPS flows provide strong convective forcing to move plasma to higher altitudes where recombination rates are reduced, leading to large storm enhanced densities (SEDs). It is also understood that the intense SAPS flows introduce perturbations in the westward

winds due to ion-drag effects [53]. This three way relationship between ionospheric plasma density, thermospheric wind and ionospheric plasma drift motivates us to investigate whether changing ionospheric plasma density during this period is evidence of zonal ion drifts consistent with the SAPS feature identified in [5].

This chapter shows that the assimilated use of global navigation satellite system (GNSS)-derived ionospheric plasma density measurements and Fabry-Perot interferometers with storm-time background models can be used to estimate ion drift behavior consistent with SAPS flows that models struggle to capture. The Estimating Model Parameters for Ionospheric Reverse Engineering algorithm (EMPIRE) uses 4-dimensional ionospheric plasma density measurements provided by IDA4D [29] to estimate corrections to the electric potential and thermospheric winds, globally. The results are storm-time ionospheric driver corrections that are consistent with the ionospheric plasma density changes over time through the use of the ion continuity equation [23].

## 6.1  Method

This section contains 2 main parts, a description of the geomagnetic storm from which the ingestion data originates and a section on the configuration parameters necessary to produce EMPIRE results.

**6.1.1  Geomagnetic Storm.**   On 17 March 2015 Earth was struck by a coronal mass ejection. Sudden commencement began at approximately 04:45 UT with a low latitude response of about 50 nT and a minimum Dst of -195 nT marking the end of the main phase around at 23:00 UT. Figure 6.1 shows the Dst index for the entire month of March 2015. The Kp index reached 8 which classifies this geomagnetic storm as severe, and the daily Ap index was 108, making this storm the most severe magnetic storm of solar cycle 24. This storm became the focus of much research [5].
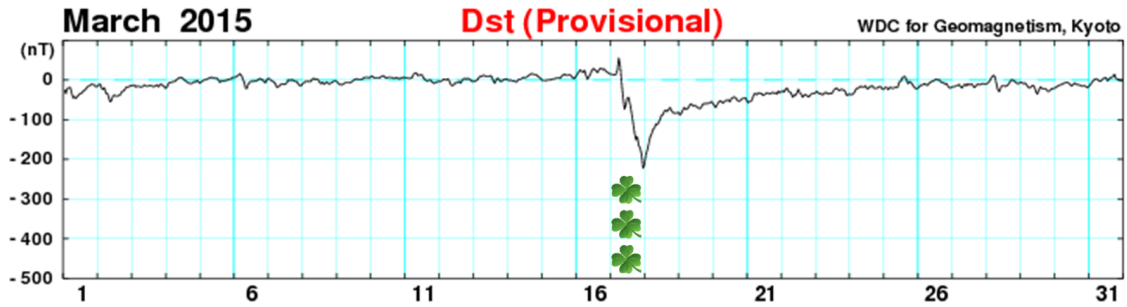
Figure 6.1. Dst index for the month of March where the shamrocks indicate the St. Patrick's Day storm day. Figure modified from the original and provided by the World Data Center (WDC) for Geomagnetism, Kyoto [4].

During this storm, the Sub-Auroral Polarization Stream (SAPS) was identified by the Millstone Hill Observatory's incoherent scatter radar (ISR) measurements of ion drifts [5]. An intense westward zonal ion drift grew to 500 m/s and was sustained for about six hours. It started at (date/hour) = 17/20 UT and ended around 18/02 UT. After 18/02 UT, the zonal ion drifts slow down and changed direction toward the east. This direction change, combined with a northward turning in the thermospheric winds was evidence of the SAPS flow as published by Zhang et al. [5]. The ion drifts oscillated by changing direction two more times until finally dying down at about 18/08 UT.

To investigate whether GNSS TEC and FPI neutral winds can be used to estimate strong SAPS-driven zonal winds, I will first use GPS TEC as inputs to IDA4D, to estimate electron density for 17-19 March 2015. Then the newly estimated electron densities are finite-differenced in time according to Eq. (3.4) for estimates of plasma density rates. These plasma density rates are input to EMPIRE as $\mathbf{y}$ to compute estimates of storm-time electric potential as the first configuration of EMPIRE. In the second configuration, EMPIRE will ingest IDA4D (as in the first configuration) but also estimate northward neutral winds to produce corrections in the field-parallel direction as well as the field-perpendicular directions. Finally, the

third configuration of EMPIRE will ingest IDA4D plasma density rates and FPI neutral winds to estimate electric potential and northward neutral winds.

To analyze the results, I will show the EMPIRE estimates of field-perpendicular drifts at the location of Millstone Hill incoherent scatter radar (ISR). These estimates will be compared to the independent ISR measurements of the ionospheric convection during this storm, that showed evidence of the SAPS field.

**6.1.2 Data.** Both the measurements and the background models must be collocated onto a single grid that EMPIRE uses for assimilation. EMPIRE uses a geomagnetic grid with -180° to 180° longitude, 30° to 150° colatitude and 150 to 650 km altitude with a spacing of 3 degrees in both latitude and longitude and 50 km spacing in altitude.

For this study, IDA4D assimilates only Global Positioning System (GPS) satellite measurements of slant TEC and estimates ionospheric plasma density on a 3D non-uniform grid. The GPS data is provided by 2 networks of GPS receivers run by Continuously Operating Reference Stations (CORS) and by the University NAVigation COnsortium (UNAVCO). Data can be accessed at [54] and [55]. Figure 6.2 shows the GPS ground stations that were assimilated by IDA4D in red and the GPS satellite ground position in blue for a single time step. As time proceeds, the blue satellite ground positions are non-stationary while the red GPS receiver dots remain stationary. IDA4D ingests the satellite-receiver line-of-sight slant TEC measurements and produces estimates on an irregular grid. The IDA4D data points are not collocated with the EMPIRE grid points. To assimilate IDA4D data into EMPIRE, the IDA4D data points are trilinear interpolated to EMPIRE's grid. The IDA4D algorithm runs are configured with the background model data set to 40% weighting and the measurements with 40% weighting.
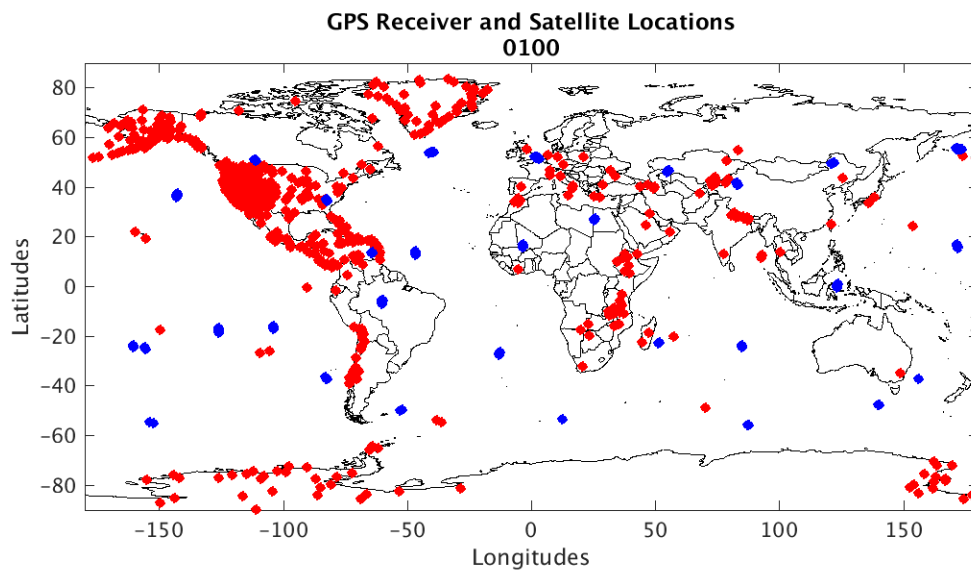
Figure 6.2. IDA4D GPS ground station receivers (red) and satellite transmitter (blue) locations.

FPI data are available for this storm from 5 different FPI sites in the American sector. Their locations are shown in Figure 6.3 with the magenta x's. The labeled dots A, B, C, D, and E correspond to the locations of the northward LOS pierce points which are approximately 250 km north and at an altitude of 250 km above the FPI locations. The longitude, latitude and site name for each location are shown in Table 6.1. Figure 6.4 shows each FPI's northern LOS measurements over the three days. The white circle corresponds to the location at which the EMPIRE ion drift results are shown later in Section 6.2.

Table 6.1. FPI Site Ionospheric Pierce Point Locations

| Site Name | Latitude (North) | Longitude (East) |
|---|---|---|
| A) Arecibo | 20.47 | -66.75 |
| B) Millstone Hill Observatory | 44.75 | -71.45 |
| C) Urbana Astronomical Observatory | 42.26 | -88.2 |
| D) Pisgah Astronomical Research Institute | 37.32 | -82.85 |
| E) Eastern Kentucky University | 39.87 | -84.29 |

EMPIRE ingests each of the models at the EMPIRE grid point locations defined in the first paragraph of Section 6.1.2. The models include: NRLMSIS-00, Weimer 2005, HWM14, IGRF-11 and IRI.

The production and loss models for a given ion species was originally formulated by [30]. When this model is used in EMPIRE, it is simplified and described in Section 2.1 in [14].

The Weimer 2005 model provides an estimate of the Earth's electric potential [56]. Inputs to this model include measurements of the interplanetary magnetic field (IMF) strength [nT] and orientation and the solar wind's velocity [km s$^{-1}$] and solar wind number density [cm$^{-3}$]. These measurements are provided by the Advanced Composition Explorer (ACE) data. Also required are the altitude adjusted corrected geomagnetic coordinates (AACGM), the magnetic local time and the universal time.
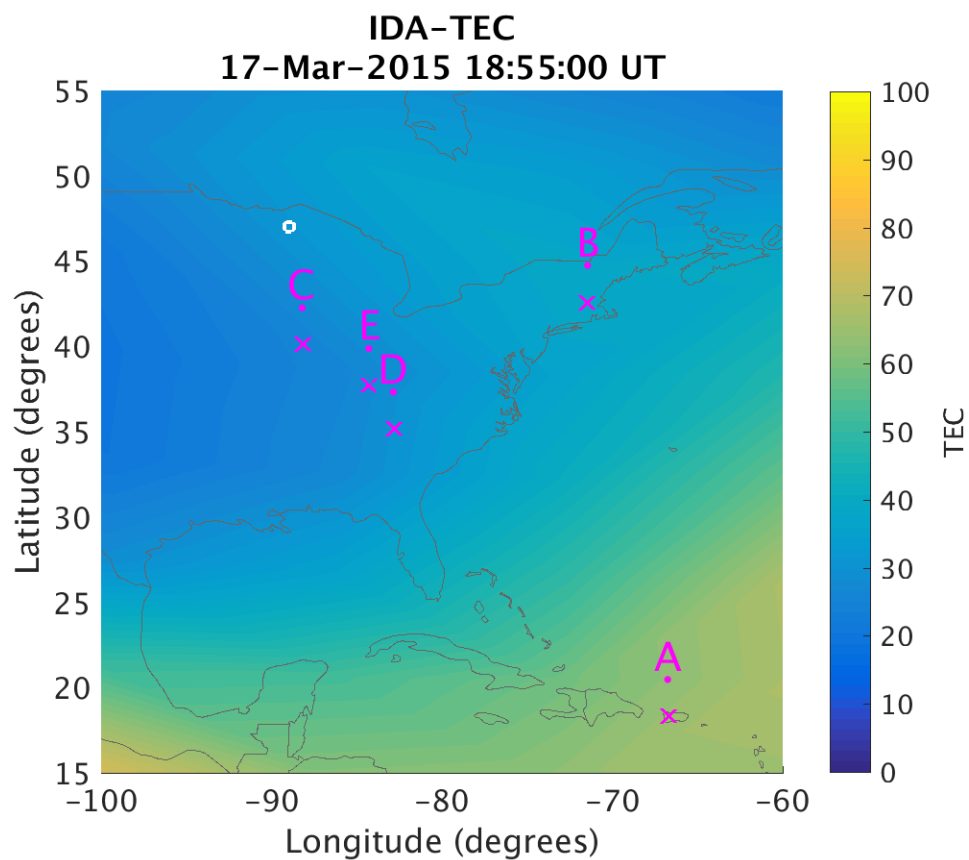
Figure 6.3. TEC map with FPI sensors (magenta x), measurement locations and the white circle shows the location where the EMPIRE results are presented, which is the approximate location of the Millstone Hill ISR beam.
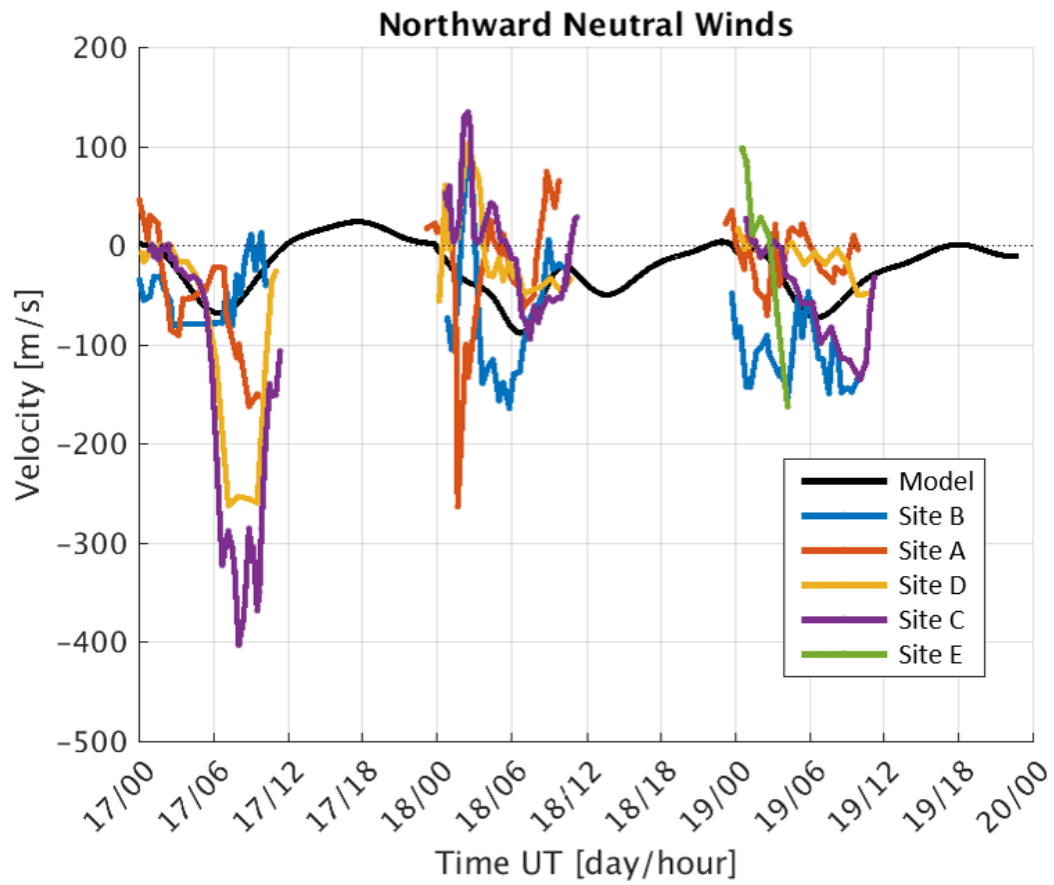
Figure 6.4. EMPIRE-ingested northern FPI LOS measurements. Site labels are described in Table 6.1

The Weimer 2005 model is used along with the IGRF-11 magnetic field model to calculate the divergence term due to $\vec{E} \times \vec{B}$ drift.

The International Geomagnetic Reference Field $11^{th}$ generation (IGRF-11) model provides a model of Earth's geomagnetic field [57]. The inputs to this model include only the location in geographic coordinates and UTC time of interest.

The Horizontal Wind Model 2014 [20] provides a model of the Earth's zonal and meridional thermospheric wind. Its inputs include the 3-hour Ap index.

The gravity model is used for computing the divergence term parallel to the magnetic field. The model includes the projection of Earth's acceleration due to gravity onto the field-parallel direction divided by a collision frequency. The collision frequency depends on the density of neutral species. The NRLMSISE-00 model provides the densities [58], and the model for the collision frequency is described in [14].

The diffusion model is another term that is required for computing the divergence parallel to the magnetic field. The model requires temperatures of the ionized and neutral species and also inversely depends collision frequency. This model is used in the same manner as described in [14].

**6.1.3 EMPIRE Configurations.** This study demonstrates EMPIRE results for three different independent configurations. The first EMPIRE configuration's observations include IDA4D ionospheric plasma density data and its state includes corrections to electric potential. The second EMPIRE configuration includes the same observations as the first but its state includes corrections for both electric potential in the field-perpendicular direction and horizontal neutral winds along the field-parallel direction. The third EMPIRE configuration includes IDA4D ionospheric plasma density and FPI LOS neutral wind observations with a state that includes corrections to

electric potential and northward neutral winds. Figure 6.5 shows the corresponding measurement models for each run depicted as a block diagram. A block diagram is a representation of a linear measurement model (e.g., $\mathbf{z} = \mathbf{Hx}$). The selection of these three ingestion schemes allows the influences of each dataset on the EMPIRE estimation.

For all three EMPIRE configurations, the electric potential is corrected using scalar spherical harmonic basis functions up to degree $l = 5$. The second and third EMPIRE configuration state also includes coefficients for both $5^{th}$ degree electric potential spherical harmonics (like the first) and includes $3^{rd}$ degree northward neutral wind power series basis functions.

EMPIRE also requires configuration parameters that are specific to a Kalman filter. The Kalman filter is set such that standard deviations from IDA4D measurements are equal to the error provided by the IDA4D algorithm, which are assumed independent [29]. The Kalman filter also includes a Gauss-Markov forward model [3]. The Gauss-Markov forward model's time constant is selected to be $\tau =$ 7200 seconds.

EMPIRE uses the basis functions, coefficients and models to reconstruct the storm-time state:

$$\hat{\mathbf{x}}_{\text{storm}} = \mathbf{B}_{\text{state}}\hat{\mathbf{x}}_{\text{state}} + a_{\text{state}} \tag{6.1}$$

I reconstruct the results and provide EMPIRE storm-time corrections located at (89° W, 45° N) geographic. This location coincides with measurements of ion drift velocity taken using the Millstone Hill Observatory's incoherent scatter radar (ISR). The results are reconstructed at an altitude of 250 km.

## 6.2  Results

EMPIRE is used to estimate the ion drifts at the same geographic location
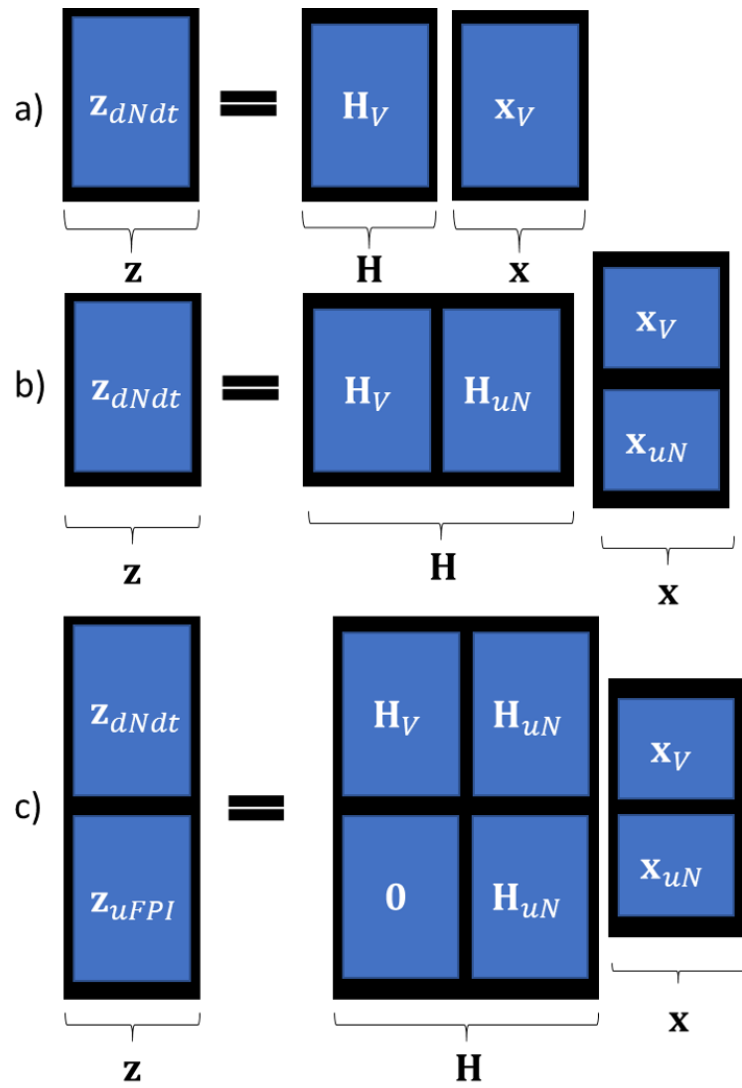
Figure 6.5. The three EMPIRE measurement models for each configuration. The terms represented as blocks are explained in Appendix B.

Figure 6.6. EMPIRE results for the first run. The y-axes shows ion drift velocity in m/s and x axis shows time. Vertical dashed lines show regions when ISR data is available. The blue line shows the EMPIRE storm-time update, red shows models and the yellow line indicate when corrections are being made.

where Millstone Hill ion drifts were provided (47° N, −89° E geographic latitude and longitude). The ion drift velocities are expressed in the magnetic field aligned frame which include the field-perpendicular meridional, field-perpendicular zonal and field-parallel vector directions. The three different run configurations (runs 1, 2 and 3) are shown in Figures 6.6, 6.7 and 6.8.

The first results shown in Figure 6.6 show that the three vector directions during the main phase of the storm (5-23 UT) the ion drifts are most erratic (i.e., not smoothly varying). Also, the peak ion drifts occur at the same time in all three directions with the zonal direction having the largest ion drift of just over -1000

Figure 6.7. EMPIRE results for the second run. The y-axes shows ion drift velocity in m/s and x axis shows time. Vertical dashed lines show regions when ISR data is available. The blue line shows the EMPIRE storm-time update, red shows models and the yellow line indicates when corrections are being made.

m/s. Shown in the first and second subplots (zonal and meridional), the ion drifts in the perpendicular directions are non-zero but in the parallel direction they are zero. This is expected as this first run only corrects the electric potential which drives only the field-perpendicular drifts. The meridional direction is smaller than the zonal direction primarily because this direction requires much larger drifts to produce the same transport. The final subplot shows the parallel corrections and since neutral winds are not being corrected, there are no corrections in this direction Finally, the error of the ion drifts is plotted here but are not visible because they are consistently between 1-10 m/s.

The differences between run 1 and 2 (see Figure 6.6) are primarily with the parallel ion drifts. Most of the time, the field-parallel ion drifts are positive (mostly northward) except during the post-dusk to midnight periods. This neutral wind direction is significantly different from the model which show mostly negative parallel drifts except from post-dusk to near midnight. Another difference between run 1 and 2 that from about 18/04UT to 18/10 UT the zonal drifts are positive in run 1 but in run 2 the zonal drifts are near zero. This positive surge during run 1 is significant and described in more detail in Section 6.3. Also, run 2 shows the zonal drifts accelerating negatively at about 18/08 UT and returning to zero at about 18/14 UT. This negative enhancement does not appear in run 1.

Next, run 3 shows a significant difference between run 1 and 2 in the field-parallel direction (See Figures 6.6 and 6.7). This is due to the ingestion of FPI data. Oscillations can be seen only during times which FPI data is made available (i.e., during local evening hours). The oscillations are the primary indicator of when FPI data is made available. These oscillations are non-physical and are due to multiple FPI site data being ingested. At any given time step (i.e., 10 minute interval) different FPI sites are available. This causes different time steps to have different results. This produces an oscillating solution which is purely due to ingestion of data and is non-physical.

## 6.3  Discussion

One of the uses of EMPIRE is to extract information about ionospheric physical drivers from images of the ionosphere itself (i.e., plasma density images from IDA4D). To assess whether these results, Figure 6.9 compares ion drift measurements taken by the Millstone Hill Observatory (MHO) incoherent scatter radar (ISR) measurements (originally published in [5]) to the EMPIRE results from run 1. The meridional ion drifts MHO ISR measurements are very large around the same time
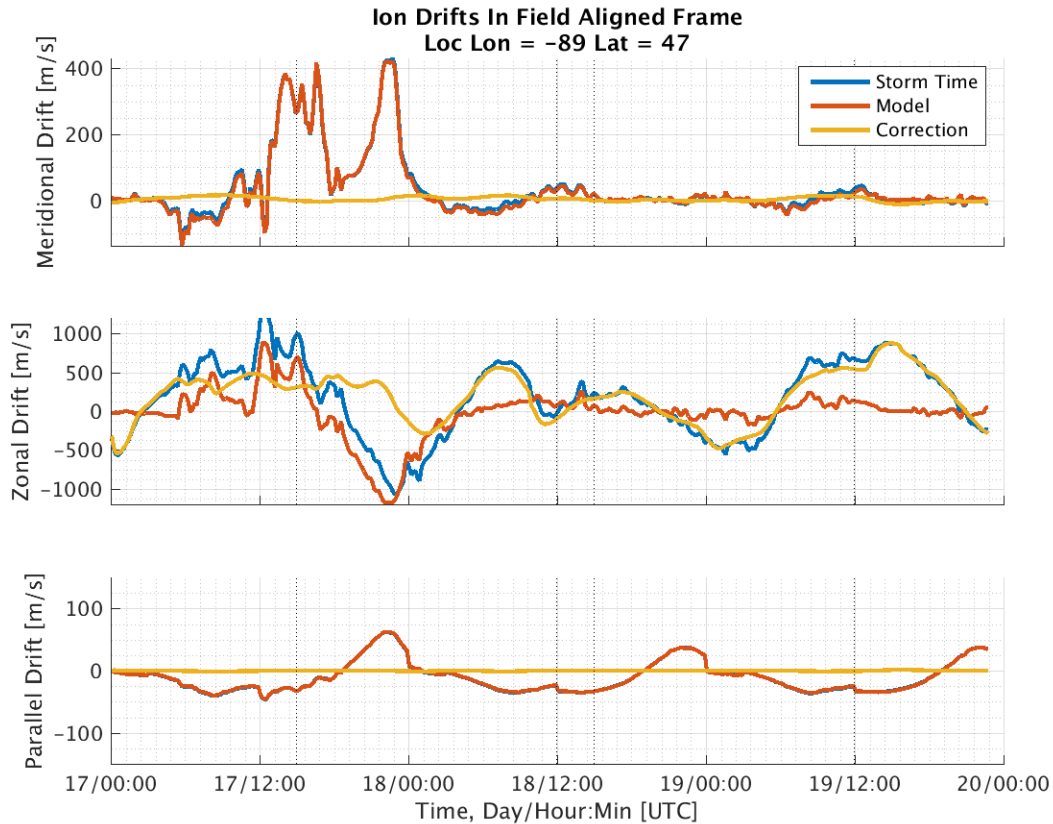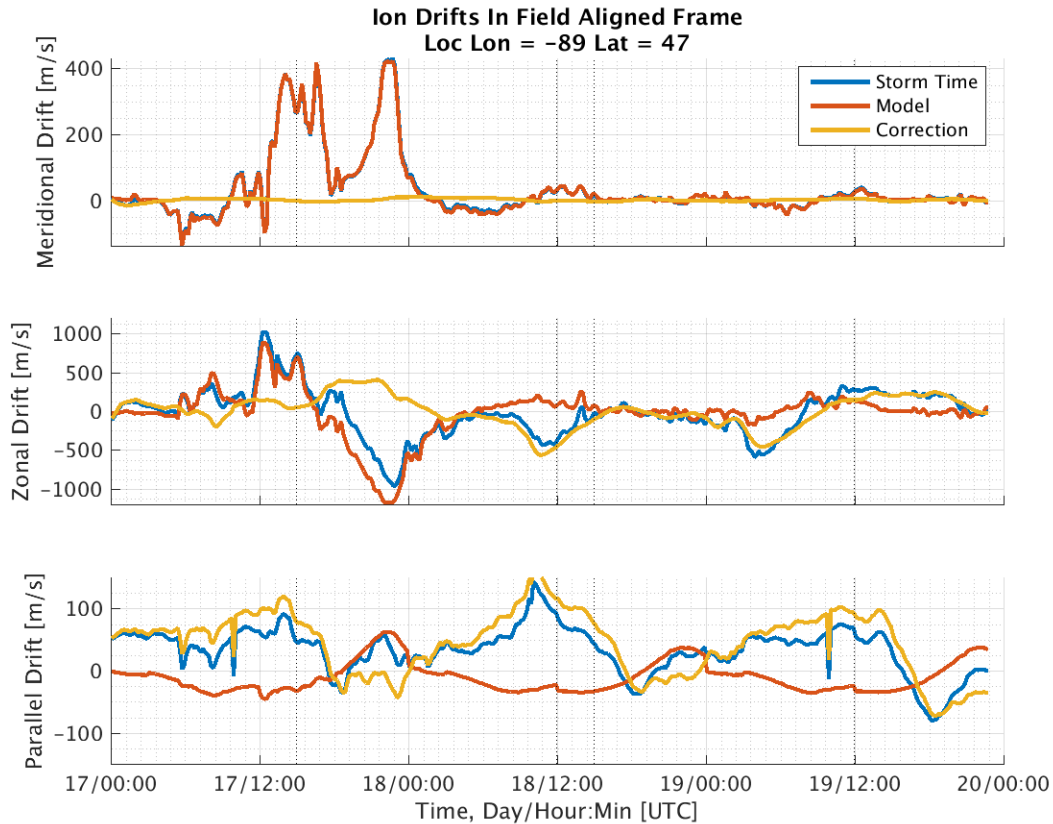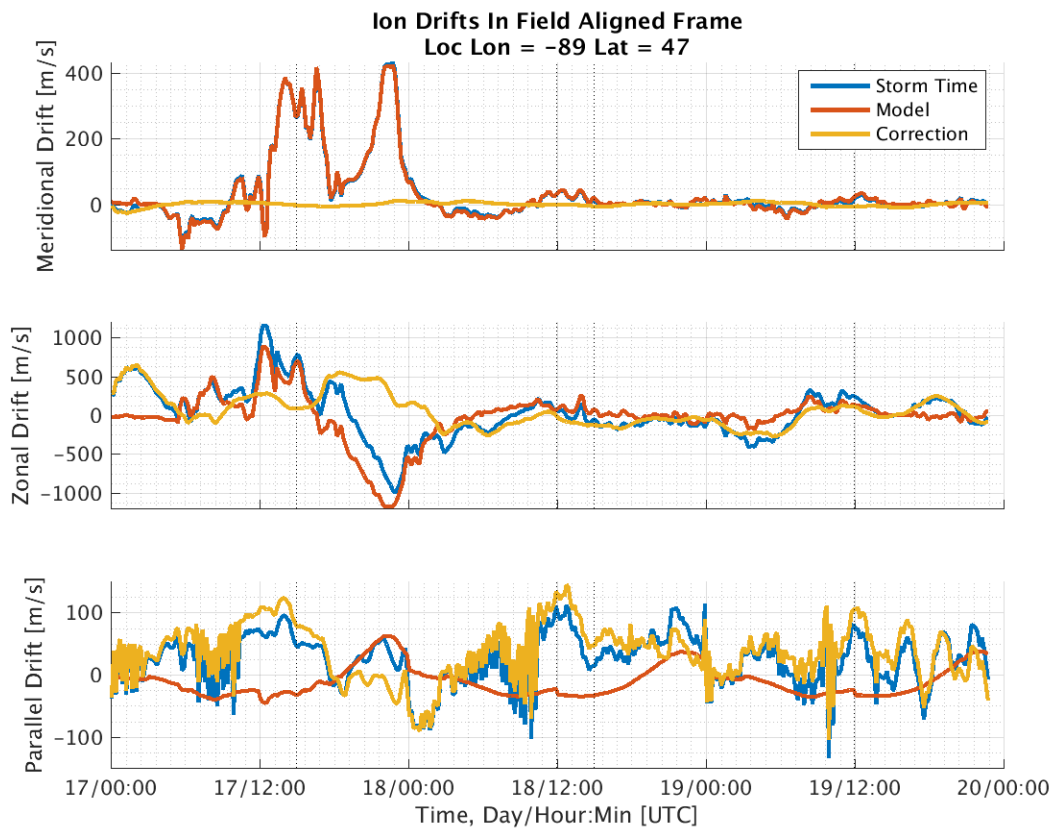
Figure 6.8. EMPIRE results for the third run. The y-axes shows ion drift velocity in m/s and x axis shows time. Vertical dashed lines show regions when ISR data is available. The blue line shows the EMPIRE storm-time update, red shows models and the yellow line indicate when corrections are being made.

the MHO ISR zonal drifts become large. At 18/02 UT a SAPs field event greatly decelerates the ion drifts and then begins accelerating in the eastward direction. This is an indicator of the SAPS field.

Another indicator of the SAPS field are the neutral winds. There are two main features of the neutral wind that are indicators of the SAPS feature. First, the northward surge for sites B,C and D around 18/03 UT coincide with the zonal ion drifts slowing and changing direction (See Figure 6.4). The northward surge was explained by Zhang et al. to be due to the Coriolis force which is driven by the zonal ion drifts [5]. Second, the neutral winds at 18/03 remain westward (see Figure 6.10) at that same time the zonal ion drifts turn eastward. When ion drifts and neutral winds are moving in opposite directions this is a clear indication of electric fields driving the ion drifts more than the neutral wind collisions.

EMPIRE results and the MHO ISR measurements have differences but follow a similar trend. EMPIRE results do a better job at capturing the increasing intensification of the ISR measurements from 17/16 UT to 17/21 than the Weimer 2005 and IGRF-11 models. Also, EMPIRE estimates larger ion drifts than the model which is more consistent with measurements (blue) from 18/00 to 18/02. After 18/02 UT, EMPIRE results capture an eastward ion drift that is delayed with respect to the measurements. The fact that EMPIRE is producing eastward ion drifts but the model is unable to suggests that there may be information within the IDA4D electron density rates that contains SAPS field but is not included in the models. If the ionospheric plasma density rate is driving the eastward ion drift during this time it is possible that this is a result of the SAPS field but with a time delay.

EMPIRE results in the meridional direction are very small. This could be due to the fact that ion drifts at mid-latitudes are mostly zonal and therefore corrections are small as well. From 17/14 to the meridional ion drift peak at 17/22 the
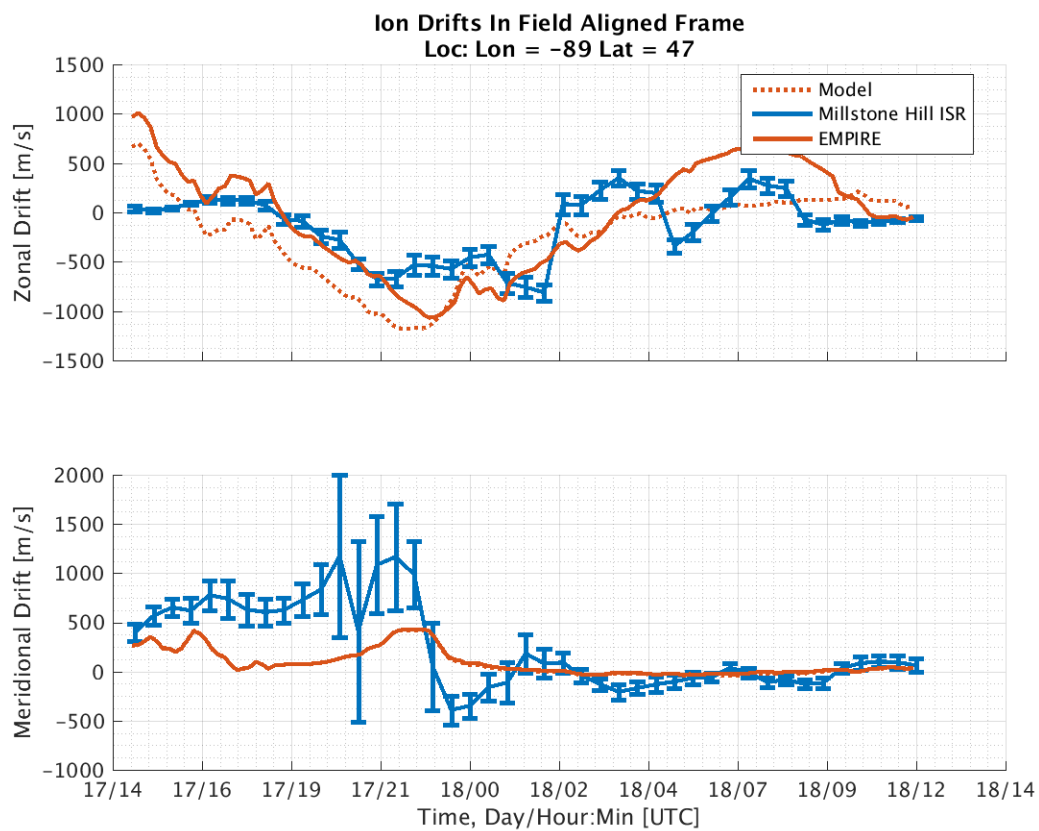
Figure 6.9. Millstone Hill and modeled perpendicular ion drift results are plotted along side the results generated from the first configuration of EMPIRE. Millstone Hill data originally published in [5].
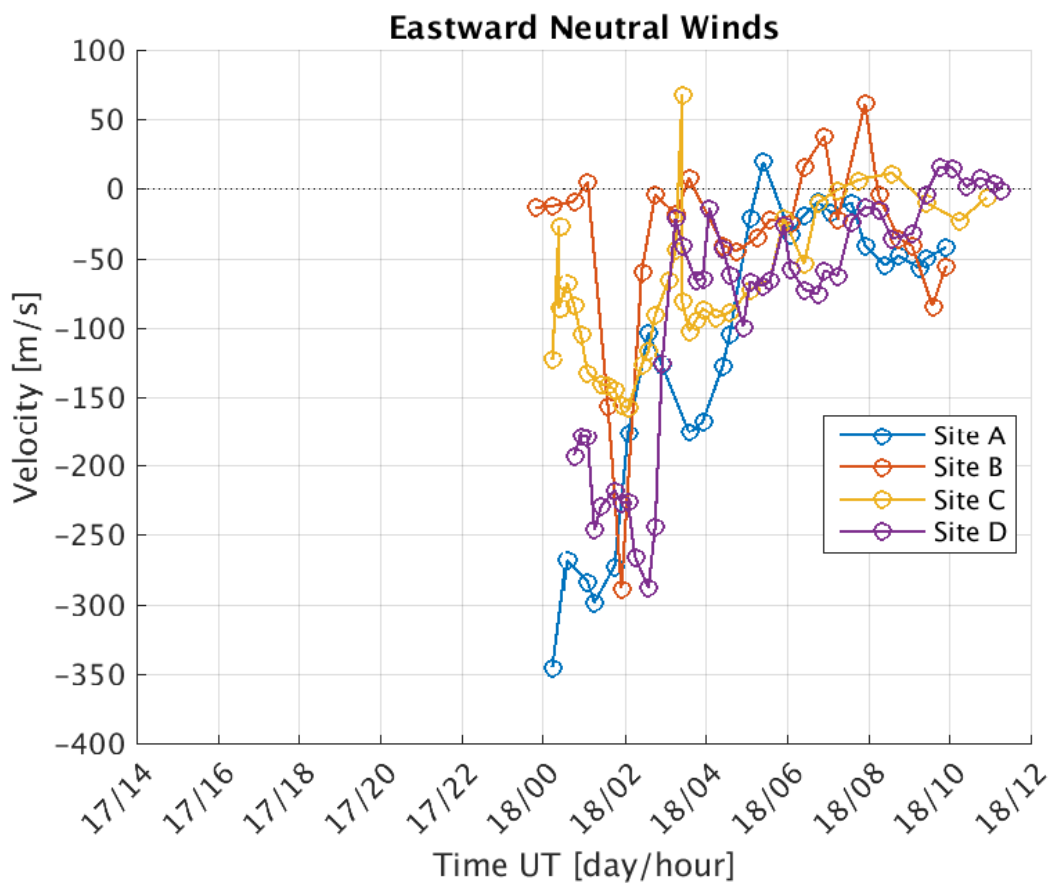
Figure 6.10. FPI neutral wind measurements during the same period as seen in Fig 6.9. Colored lines show the FPI eastward LOS measurements. Site E (Eastern Kentucky) data was not available until the 19 March 2015.

model meridional drifts agree with the ISR measurements on direction and time of the greatest velocity but does not have a correct magnitude. After 18/00 UT, the measurements show the meridional ion drifts slowing down to the model values with some oscillations corresponding to ionospheric waves.

In order to see the difference between EMPIRE runs in detail, Figure 6.11 shows all three of the runs plotted just for the 17/14 to 18/12 UT (i.e., storm-time). The figure shows minor differences between the runs in the zonal direction (top subplot) except for after 18/04 UT. Zhang et al., 2015 identified this time as the same time which the SAPS field is causing ion drifts to accelerate eastward and neutral winds to be remain westward. Eastward EMPIRE estimated ion drifts only occurred for run 1. Looking back at Figure 6.6, the corrections after 18/04 UT are minor. This shows that the Weimer model is doing a good job estimating the ion drifts at this time however Weimer misses the large positive eastward velocities. The same goes for the EMPIRE results which are include a single period of eastward drifts with no momentary turning like shown during 18/04 to 18/07. It is possible that EMPIRE is unable to resolve the high resolution effects of the SAPS field during this time and that Weimer is unable to produce an eastward ion drift response at all.

There are several possible causes for why EMPIRE's results do not match the ISR measurements. The primary cause is that EMPIRE is not using the ISR measurements but is inferring them from plasma density images. It can take time for the ionosphere plasma density to respond if a small time-scale events occur. Even more-so, EMPIRE does not estimate the ion drifts but rather the electric potential. In order to obtain more accurate ion drift information, direct ingestion of ISR data and models of ion drifts would be helpful.

## 6.4 Conclusions
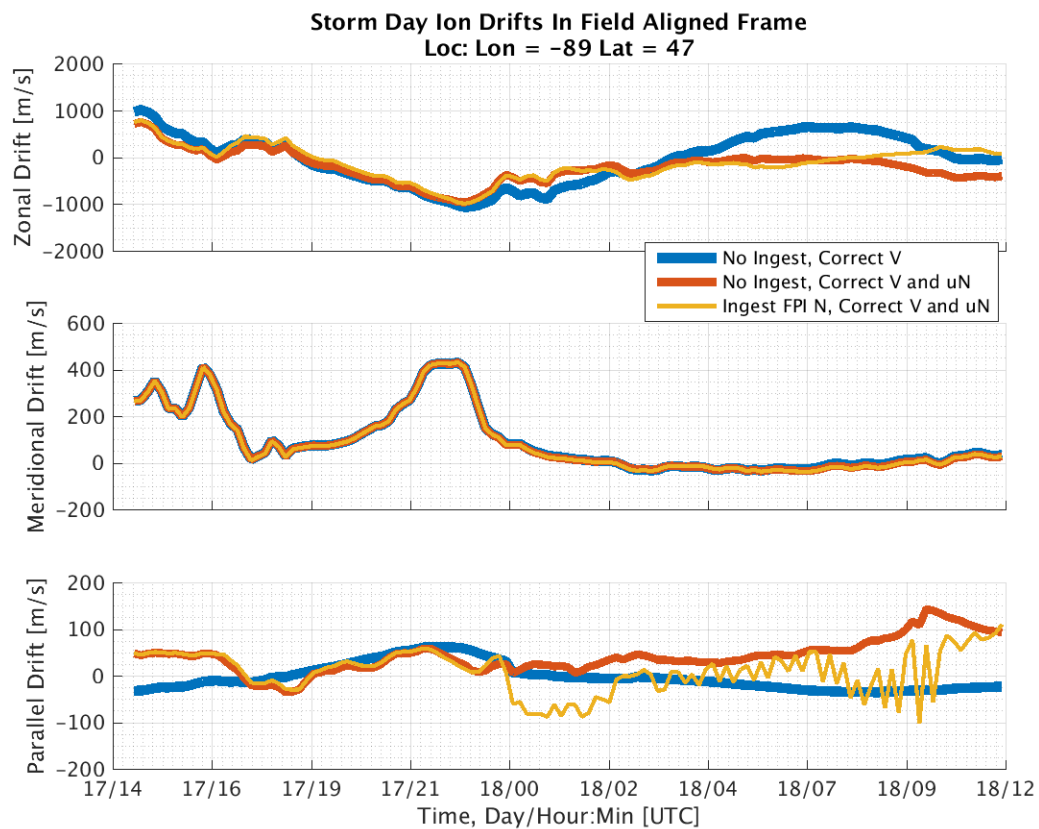
Figure 6.11. All three EMPIRE runs plotted for the storm day. The blue line is the first EMPIRE run, the red is the 2nd and the yellow is the third.

EMPIRE was modified to use spherical harmonic basis functions for estimating electric potential, globally. The subsequent ion drifts from these electric potential corrections were presented for three different EMPIRE configurations. The EMPIRE configuration which matched the measured MHO ISR measurements the most was the first one where EMPIRE was configured to use storm-time IDA4D plasma density rate for estimation of electric potential corrections. As EMPIRE configurations were changed it was shown that adding neutral wind corrections as a state reduced the electric potential corrections and therefore also reduced the field-perpendicular ion drift corrections. Also, adding neutral wind data introduced oscillations because of different FPI site measurements occurring at different time periods. This suggests that electric fields were the primary driver at this time. This shows promise toward providing quality data assimilation estimates that make use of both model data and measurement data to provide storm-time ionosphere state estimation.

CHAPTER 7

CONCLUSION

This dissertation has presented a data assimilation algorithm for ingesting
Global Navigation Satellite System (GNSS) plasma density, Fabry-Perot Interferom-
eter (FPI) neutral wind measurements and background ionosphere and thermosphere
models to estimate the physical drivers of the ionospheric plasma density. A study
that is included within this research demonstrates the use of GNSS plasma density
and FPI measurements for producing ion drift estimates during severe geomangetic
storms where sub-auroral polarization steam features are present. The main contri-
butions include 1) Kalman filtering for multi-instrument ingestion, 2) FPI neutral
wind data ingestion, 3) spherical harmonics for global data ingestion and 4) data
assimilation study during the March 17th 2015 severe geomagnetic storm.

## 7.1 Summary and Discussions

Chapter 3 derived and presented a Kalman filtering approach for assimilating
IDA4D plasma density measurements and background models to estimate ionospheric
drivers. This was an improvement from the previous implementation of weighted-
least-square estimation. The plasma density from IDA4D is finite differenced to
produce the $y_N$ term and the background models are summed together to produce a
net background model for the change in plasma density over time or $a_N$. Subtracting
the measurements from the models produced the Kalman filter's observations, $\mathbf{z}$ The
states are basis functions which represent plasma transport drivers over space. These
drivers include electric potential and neutral winds. The mapping matrix is used in
the linear measurement model ($\mathbf{z} = \mathbf{Hx}$) is defined using ion continuity equation to
map from the transport driver states to the plasma density rate observations. The

developed algorithm is a method for ingesting both observations and uncertainty in those observations to provide estimates of the physical drivers of the ionosphere.

Chapter 4 derived and presented the augmentation of the EMPIRE linear measurement model to include FPI neutral wind measurements. FPI neutral wind measurements provided direct information of the thermospheric neutral wind in geographic east and north directions where previously the ionospheric plasma density rate only provided estimates of neutral winds in the magnetic field-aligned direction. Demonstration of these results was carried out by studying the 24 October 2011 geomagnetic storm. Results showed that FPI neutral winds improved neutral wind estimation. Ion drift estimates also responded to FPI measurement ingestion such that only the parallel direction had any noticeable change. This study showed that with a combination of both FPI neutral winds and GNSS plasma density measurements EMPIRE can improve estimation of storm-time neutral winds regionally.

Chapter 5 proposed use of spherical in basis functions to allow for estimation of ion drifts and neutral winds, globally. The changes were in the EMPIRE measurement model where derivatives of the spherical harmonic basis functions replaced derivatives of power series basis functions for electric potential. The spherical harmonic basis function for EMPIRE is unique in that it provides a spherical harmonic fit for electric potential that is constrained to be constant along the field line. The field lines were modeled as dipole field lines which restricts EMPIRE to low-mid latitudes so the L-shell is not too large. Modifying EMPIRE to use the more sophisticated spherical harmonic basis functions allows the results to be constant along the -180 to 180 boundary and thereby enable estimation of storm-time ionospheric drivers globally.

Chapter 6 demonstrated the EMPIRE algorithm use by ingesting IDA4D plasma density globally and FPI neutral wind data from 5 different locations and compared the results to measurements taken by the Millstone Hill (MH) incoherent

scatter radar (ISR). On 17-18 March 2015, the largest geomagnetic storm of the 24th solar cycle occurred. The MHO ISR recorded ion drifts with a sustained westward zonal drift of 1000 m/s for several hours. Three different EMPIRE configurations were presented: 1) with IDA4D plasma density rate observations for estimating electric potential corrections, 2) with the same IDA4D plasma density rate observations but for simultaneously estimating neutral winds and electric potential corrections and 3) with IDA4D plasma density rate and FPI lOS neutral wind observations for estimating simultaneous electric potential and neutral wind corrections. When comparing to ISR data, the first EMPIRE configuration produced electric potential corrections that best represented the MHO ISR ion drift measurements. Also, the results suggested that the ionospheric plasma density response to the SAPS field lagged the electric field driven ion drifts suggesting a possible delay in the ionospheric response to SAPS fields. Direct ingestion of ion drifts would prove useful when estimating ion drifts during severe geomagnetic storms. For low-latitude phenomena, the system is well-prepared to assimilate measurement from the upcoming NASA Ionospheric Connection Explorer (ICON) mission, since it is global and able to ingest neutral winds.

## 7.2 Future Work

### 7.2.1 Vector Spherical Harmonics for Neutral Wind Estimation.
Chapter 4 laid the foundations for assimilating neutral winds into EMPIRE, however estimates of the neutral wind ionospheric driver are currently fit using power series basis functions. Power series basis functions are insufficient because they are not continuous on a spherical domain. This requires new basis functions similar to the scalar spherical harmonic basis functions of Chapter 5 but neutral winds will use vector spherical harmonics instead. Vector spherical harmonics are an adaptation to spherical harmonics which produce a set of basis functions that analytically describe an orthogonal set.

In the case of the ionosphere and thermosphere region, this can be simplified to two dimensions, North and East.

**7.2.2  Smoothing of ingested data..**  Chapter 6 showed that when FPI LOS measurements from different spatially distributed sites can cause disagreements from one timestep to the next. This results in oscillations in the final estimation because teh available data changes at each time step. While these oscillations are non-physical themselves, a mean value will be more representative. To remedy this current limitation of EMPIRE, pre-smoothing the data using an interpolation model can provide more physically representative results over time.

**7.2.3  Ingestion of ion drift measurements..**  Chapter 4 and 6 presented two different studies which demonstrated the use of EMPIRE in estimating storm-time drivers of the ionosphere. In both studies, EMPIRE showed results of drivers that are vector quantities and revealed the usefulness of directly ingesting measurements of the ionospheric drivers (i.e., the states themselves). In the case of Chapter 4, the study showed that ingestion of FPI LOS neutral wind measurements was crucial in estimating storm-time neutral winds. In Chapter 6 the lack of ingesting ion drift measurements suggested that ingesting them would be useful. In general, direct ingestion of an ionospheric state has shown to be useful and one available state could be ion drifts from incoherent scatter radars or in situ satellite measurements. Augmenting the EMPIRE algorithm to ingest ion drift measurements will be very helpful when estimating storm-time states.

APPENDIX A

EMPIRE KALMAN FILTER MEASUREMENT MODEL MATRICES

This appendix describes the construction of the matrices $\mathbf{H}_N$ in Eq. (3.8) and $\mathbf{H}_u$ in Eq. (4.3) that map the states to the observations when using power series basis functions.

**A.1 The Linear Continuity Equation**    Beginning from Eqs. (3.6), (3.7), and (2.2), the field-perpendicular drift term correction $\delta a_{exb}$ will give the matrix $\mathbf{H}_{Vi}$ as:

$$\delta a_{exb,i} = -\vec{\nabla} \cdot (N\delta\vec{v}_{\perp,i}) = -\vec{\nabla} \cdot (N\frac{-\vec{\nabla}\delta V_i \times \vec{B}}{B^2}) \tag{A.1}$$

$$= \mathbf{H}_{i,V}\mathbf{x}_V \tag{A.2}$$

$$\mathbf{H}_{V,i} = \begin{bmatrix} a_R & a_\theta & a_\phi \end{bmatrix}_i \begin{bmatrix} b_{R1} & b_{R2} & \dots & b_{Rj_{max}} \\ b_{\theta1} & b_{\theta2} & \dots & b_{\theta j_{max}} \\ b_{\phi1} & b_{\phi2} & \dots & b_{\phi j_{max}} \end{bmatrix}_i \tag{A.3}$$

$$b_j = \left(\frac{R_{eq}}{R_E}\right)^k (\theta_i - \theta_0)^l (\phi_i)^p \tag{A.4}$$

$$j = \{1, 2, ..., (k_{max} + 1)(l_{max} + 1)(p_{max} + 1)\}\} \tag{A.5}$$

Where for $\mathbf{E} \times \mathbf{B}$, $l$ and $l_{max}$ both equal zero for the power on $\theta$. So we can then define the $a$ and $b$ terms as:

$$a_R = -\frac{1}{B^2 R \sin(\theta)} \left( B_\theta \frac{\partial N}{\partial R} - \frac{B_r}{R} \frac{\partial N}{\partial \theta} \right) \tag{A.6}$$

$$+ \frac{6N \cos(I)(1 + \cos^2(\theta))}{BR^2 \sin(\theta)(1 + 3\cos^2(\theta))} \tag{A.7}$$

$$a_\theta = \frac{\frac{2B_R}{\tan\theta} + B_\theta}{|B|^2 R \sin^3(\theta)} \frac{\partial N}{\partial \phi} \tag{A.8}$$

$$a_\phi = 0 \tag{A.9}$$

$$b_{Rj} = p \left(\frac{R_{eq}}{R_E}\right)^k (\phi)^{p-1} \tag{A.10}$$

$$b_{\theta j} = \frac{k}{R_E} \left(\frac{R_{eq}}{R_E}\right)^{k-1} (\phi)^p \tag{A.11}$$

$$b_{\phi j} = 0 \tag{A.12}$$

Where $R_{eq} = R/(\sin^2 \theta)$ is the equatorial radius of the field line passing through the given grid point. The index $i$ is for a given grid point. For brevity, the single index $j$ is used instead of the index triplet $klp$ as defined in Eq. (A.5).

The field-aligned correction $\delta a_{||}$ is assumed to be entirely due to neutral winds, which are then decomposed into the geographic horizontal meridional and zonal components (vertical winds corrections are assumed 0). From Eqs. (2.18) and (3.7) the divergence may be distributed.

$$\delta a_{||} = -\vec{\nabla} \cdot (N\delta\vec{v}_{||}) \tag{A.13}$$

$$= \underbrace{-\vec{\nabla} \cdot \left( N(\delta u_N \hat{n}_g \cdot \hat{b})\hat{b} \right)}_{\delta a_{uN}} \underbrace{-\vec{\nabla} \cdot \left( N(\delta u_E \hat{e}_g \cdot \hat{b})\hat{b} \right)}_{\delta a_{uE}} \tag{A.14}$$

Splitting the correction into $\delta a_{uN}$ and $\delta a_{uE}$,

$$\delta a_{uN,i} = -\left( \vec{\nabla} \cdot \hat{b} \right) (N\delta u_{N,i} \hat{n}_g \cdot \hat{b})$$
$$\quad - \left( \hat{b} \cdot \vec{\nabla} \right) (N\delta u_{N,i} \hat{n}_g \cdot \hat{b}) \tag{A.15}$$

$$\tag{A.16}$$

where $\mathbf{H}_{uN,i}$ is structured exactly as in Eq. (A.3), but containing the following ele-

ments instead:

$$a_N = -N\cos(D)\cos(I)(\vec{\nabla}\cdot\hat{b}) - \cos(D)\cos I\hat{b}\cdot\vec{\nabla}N$$

$$- N\cos(I)\hat{b}\cdot\vec{\nabla}(\cos(D)) \tag{A.17}$$

$$+ N\cos(D)\cos(I)\frac{\sin(I)}{2R}(1+3\cos^2(I)) \tag{A.18}$$

$$a_R = N\cos(D)\cos(I)\sin(I) \tag{A.19}$$

$$a_\theta = N\cos(D)\frac{\cos^2(I)}{R} \tag{A.20}$$

$$b_{0j} = \left(\frac{R}{R_E}\right)^k (\theta-\theta_0)^l(\phi)^p \tag{A.21}$$

$$b_{Rj} = \frac{k}{R_E}\left(\frac{R}{R_E}\right)^{k-1} (\theta-\theta_0)^l(\phi)^p \tag{A.22}$$

$$b_{\theta j} = l\left(\frac{R}{R_E}\right)^k (\theta-\theta_0)^{l-1}(\phi)^p \tag{A.23}$$

Meanwhile for $\delta a_{uE}$ we have:

$$\delta a_{uE} = -\left(\vec{\nabla}\cdot\hat{b}\right)\left(N(\delta u_E\hat{e}_g\cdot\hat{b})\right.$$

$$-\left(\hat{b}\cdot\vec{\nabla}\right)\left(N\delta u_E\hat{e}_g\cdot\hat{b}\right) \tag{A.24}$$

$$= \mathbf{H}_{uE,i}\mathbf{x}_{uE} \tag{A.25}$$

where $\mathbf{H}_{uE,i}$ is structured exactly as in Eq. (A.3), but containing the following elements instead:

$$a_N = -N\sin(D)\cos(I)\vec{\nabla}\cdot\hat{b} - \sin(D)\cos(I)\hat{b}\cdot\vec{\nabla}N$$

$$-N\cos(I)\hat{b}\cdot\vec{\nabla}(\sin(D)) + N\sin(D)\frac{\sin(I)\cos(I)}{2R}(1+3\cos^2(I)) \tag{A.26}$$

$$a_R = N\sin(D)\cos(I)\sin(I) \tag{A.27}$$

$$a_\theta = N\sin(D)\frac{\cos^2(I)}{R} \tag{A.28}$$

For $\mathbf{H}_{uE,i}$, the $b_{0j}, b_{Rj}, b_{\theta j}$ are given by Eqs. (A.21)-(A.23).

Finally the $\mathbf{H}_N$ mapping matrix has been fully defined

$$\mathbf{H}_N = \begin{bmatrix} \mathbf{H}_V & \mathbf{H}_{uN} & \mathbf{H}_{uE} \end{bmatrix} \tag{A.29}$$

**A.2 Line of Sight Wind Matrix**   When ingesting neutral wind measurements, the geographic meridional component of the wind correction $\delta u_N$ in Eq. (4.2) is modeled as a power series in geomagnetic radius, colatitude and longitude, as in Eq. (A.10). Then the row matrix $\mathbf{H}_{uN}$ for the $i^{th}$ measurement location consists of:

$$\mathbf{H}_{uN} = \cos(el)\cos(az)\mathbf{b}_i \tag{A.30}$$

where the terms $b_{ij}$ in $\mathbf{b_i}$ are as given in Eq. (A.4), and the geographic meridional wind component $\delta u_{gmer}$ has been projected onto the line of sight direction by multiplying by $\cos(el)\cos(az)$.

A similar process is repeated for the geographic zonal component of the wind correction $\delta u_E$ in Eq. (4.2). The power series matrix in Eq. (A.10) is again constructed and scaled by $\cos(el)\sin(az)$ to project it onto the line of sight direction:

$$\mathbf{H}_{uE} = \cos(el)\sin(az)\mathbf{b}_i \tag{A.31}$$

Now the submatrices in $\mathbf{H}_u$ have been defined

$$\mathbf{H}_u = \begin{bmatrix} \mathbf{0} & \mathbf{H}_{uN} & \mathbf{H}_{uE} \end{bmatrix} \tag{A.32}$$

where $\mathbf{0}$ represents a matrix of zeros of the appropriate dimensions.

**A.3 Model Covariances used in EMPIRE**   The model covariance $\mathbf{R}_a$ contains

a variance for each grid point background model. It is user-defined, then represented in state space for each state term (Eq. 3.12), making it a square matrix with length of the number of state elements. The model estimate at each grid point is assumed to be independent and identically distributed (IID). This results in a diagonal matrix. The covariance matrix for each state term is normalized and then stacked into a single matrix:

$$\mathbf{R}_a = \text{diag}\begin{bmatrix}\mathbf{R}_V & \mathbf{R}_u\end{bmatrix} \tag{A.33}$$

The variance on drift speed associated with the Weimer model is set to $\sigma_V^2 = (20 \text{ km/s})^2$. The drift values are considered IID and placed along the diagonal of a square covariance matrix $\mathbf{R}_{a\vec{v}}$ of length $i_{max}$, where the $v$ superscript represents ion drift space. The electric potential is related to the ion drift as Eq. (5.2) shows, and can be represented with mapping matrices $\mathbf{H}_{Vr}, \mathbf{H}_{V\theta}, \mathbf{H}_{V\phi}$ which take the gradient and cross with the magnetic field to obtain each component of the ion drift, respectively, as indicated by the superscript. These are used to determine the corresponding variance of the coefficients $\mathbf{R}_{a\mathbf{x}_V}$ in state space.

$$\begin{aligned}\tilde{\mathbf{R}}_{a\mathbf{x}_V} &= (\mathbf{H}_{Vr})^\dagger \mathbf{R}_{a\vec{v}}((\mathbf{H}_{Vr})^T)^\dagger \\ &\quad + (\mathbf{H}_{V\theta})^\dagger \mathbf{R}_{a\vec{v}}((\mathbf{H}_{V\theta})^T)^\dagger \\ &\quad + (\mathbf{H}_{V\phi})^\dagger \mathbf{R}_{a\vec{v}}((\mathbf{H}_{V\phi})^T)^\dagger\end{aligned} \tag{A.34}$$

where the † symbol represents the Moore-Penrose pseudoinverse [59]. We then extract only the diagonal terms and divide by 3 to normalize for the fact that there are 3 component directions. Next, the variances are normalized as follows:

$$\mathbf{R}_{a\mathbf{x}_V} = \frac{(2 \cdot 10^4)^2}{3\mathbf{max}[\tilde{\mathbf{R}}_{a\mathbf{x}_V}]}\tilde{\mathbf{R}}_{a\mathbf{x}_V} \tag{A.35}$$

The maximum variance for the modeled geographic meridional horizontal neutral wind is defined as $\sigma^2_{u_N} = (75 \text{ m/s})^2$. Since the HWM14 model values are considered as IID they are placed into a diagonal matrix, $\mathbf{R}_{a,u_N}$.

The row arrays $\mathbf{b_i}$ from Eq. (A.4) can be stacked to produce matrix $\mathbf{B}$ representing the power series factors:

$$\mathbf{B} \;=\; \begin{bmatrix} \mathbf{b_1} \\ \vdots \\ \mathbf{b_i} \\ \vdots \\ \mathbf{b_{i_{max}}} \end{bmatrix} \tag{A.36}$$

So that the model space of $\mathbf{u}$ at all gridpoints is given by $\mathbf{u} = \mathbf{B}\mathbf{x}_{uN}$. Then $\mathbf{R}_{a,u_N}$ is mapped to state space as:

$$\tilde{\mathbf{R}}_{a,\mathbf{x}_{uN}} = \mathbf{B}^{\dagger}\mathbf{R}_{a,u_N}(\mathbf{B}^{T})^{\dagger} \tag{A.37}$$

where $\mathbf{B}$ is given in Eq. (A.36). Assuming that the off diagonal terms are negligible, we extract only the diagonal elements. The final covariance matrix for the meridional neutral wind, $\mathbf{R}_{a,\mathbf{x}_{uN}}$, is obtained by scaling the covariances as:

$$\mathbf{R}_{a,\mathbf{x}_{uN}} = \frac{75^2}{\mathbf{max}[\mathbf{diag}[\tilde{\mathbf{R}}_{a,\mathbf{x}_{uN}}]]}\mathrm{diag}[\tilde{\mathbf{R}}_{a,\mathbf{x}_{uN}}] \tag{A.38}$$

The covariance for the model geographic zonal wind $\mathbf{R}_{a,\mathbf{x}_{uE}} = \mathbf{R}_{a,\mathbf{x}_{uN}}$ for simplicity and ease of implementation.

APPENDIX B

DERIVATION OF SPHERICAL HARMONICS FOR ELECTRIC POTENTIAL

STATE ESTIMATION

This derivation shows how I will apply a spherical harmonic function as a basis function to compute states that correspond to the Earth's electric potential. It contains several sections. The first section will show, the general form of a spherical harmonic function that I will use. The second section will show how I adapt this function for use with estimating electric potential corrections.

## B.1  General Form of a Two Dimensional Scalar Spherical Harmonic Function

**B.1.1  Introduction.**  The two dimensional (2D) scalar spherical harmonic is given by:

$$\Psi_l^m\,(\theta,\phi) = N_l^m P_l^m[\theta][\cos(m\phi) + i\sin(m\phi)] \tag{B.1}$$

$$N_l^m = \sqrt{\frac{2l+1}{2\pi}\frac{(l-m)!}{(l+m)!}} \tag{B.2}$$

$$P_l^m(\theta) = \frac{(-1)^m}{2^l l!}\sqrt{(1-\theta^2)^m}\frac{d^{l+m}}{d\theta^{l+m}}(\theta^2-1)^l \tag{B.3}$$

Where:

- $l \in \mathbf{N}_0$, is the "band class"

- $m \in [0,l]$, sub divides the bands and is called the "degree".

- $N_l^m$, is a normalization constant

- $P_l^m(\theta)$, is the associated Legendre polynomial and is the $\theta$ dependent term.

- $[cos(m\phi) + isin(m\phi)]$, is the harmonic term and is the $\phi$ dependent term.

- $\theta$, is geomagnetic colatitude

- $\phi$, is geomagnetic longitude

Where the spherical harmonic function, $\Psi_l^m(\theta, \phi)$, sometimes is represented by $Y_l^m(\theta, \phi)$. This function is only a function of $\theta$ and $\phi$. Due to the orthogonality of Legendre polynomials (Eq. (B.3)) being defined from -1 to 1 and analysis regions being defined with colatitude from 0 to $\pi$ it is common to map the 0 to $\pi$ domain to the -1 to 1 domain using $\cos(\theta)$. The Legendre polynomial is then:

$$P_l^m(\cos(\theta)) = \frac{(-1)^m}{2^l l!}\sqrt{(1-\cos^2(\theta))^m}\frac{d^{l+m}}{d\cos(\theta)^{l+m}}\left[(\cos^2(\theta)-1)^l\right] \tag{B.4}$$

**B.1.2 Applying this to Electric Potential.** Starting with Eq A1 from Appendix A in reference [3]:

$$\delta a_{exb} = -\vec{\nabla}\cdot(N\delta\vec{v}_\perp) = -\vec{\nabla}\cdot(N\frac{-\vec{\nabla}\delta V\times\vec{B}}{B^2}) \tag{B.5}$$

$$\vec{\nabla} = \left[\frac{\partial}{\partial r}\hat{r}, \frac{1}{r}\frac{\partial}{\partial\theta}\hat{\theta}, \frac{1}{r\sin(\theta)}\frac{\partial}{\partial\phi}\hat{\phi}\right]_{/gm} \tag{B.6}$$

$$-\vec{\nabla}\cdot(N\delta\vec{v}_\perp) = -\left(\vec{\nabla}N\cdot\delta\vec{v}_\perp + N\vec{\nabla}\cdot\delta\vec{v}_\perp\right) \tag{B.7}$$

Equation (B.7) is a useful identity that will be put to use later. The subscript '/gm' indicates that the unit vectors $\hat{r}$, $\hat{\theta}$ and $\hat{\phi}$ are apart of the 'geomagnetic' reference frame. The $\hat{r}$ unit vector is the radial direction (positive facing up away from the normal to the surface of Earth), $\hat{\theta}$ is the colatitude direction (positive southward from the geomagnetic north pole) and $\hat{\phi}$ is the longitude direction (positive eastward facing and completes the right hand). The $\vec{B}$ is the magnetic field, $N$ is the plasma density, and $\delta V$ is the correction to Earth's electric potential. The notation $B^2$ represents the norm of $\vec{B}$ squared and from now on for clarity I will use $B^2$ to represent the norm squared. For this application of spherical harmonic functions I will only keep the real part of the spherical harmonic function (B.1) and I will also add an additional sine term. This requires two pairs of coefficients for every basis function. The new basis function will then take the form:

$$\delta V(\cos(\theta), \phi) = \sum_{l=0}^{L} \sum_{m=0}^{l} \left(\frac{r}{R_e}\right)^l P_l^m(\cos(\theta))[x_c^{lm}\cos(m\phi) + x_s^{lm}\sin(m\phi)] \qquad \text{(B.8)}$$

Where:

$$\Phi_l^m(\phi) \triangleq [x_c^{lm}cos(m\phi) + x_s^{lm}sin(m\phi)] \qquad \text{(B.9)}$$

Defining the basis function $\delta V$ I have

$$\boxed{\delta V = \left(\frac{r}{R_e}\right)^l P_l^m(\cos(\theta))\Phi_l^m(\phi)} \qquad \text{(B.10)}$$

The subscripts $c$ and $s$ correspond to the coefficients multiplying the cosine and sine terms. Also, I am compacting the function such that the Legendre term, $P_l^m$, automatically contains the normalization constant within it. Also, from now on when the subscripts $l$ and $m$ are shown it implies a summation as shown in equation (5.1).

**B.1.3 Derivatives of $\delta V$.** The derivatives of the spherical harmonic function will be needed later in this derivation. Next, I present those gradient functions upfront for ease of reference later on. The derivative with respect to $r$ is zero for this a 2D Spherical harmonic function. Later in Section B.2 I will extend the 2D spehrical harmonic function to 3D using the dipole field line equation to constrain it.

**B.1.3.1 Derivative of the basis function with respect to $\theta$ ($\delta V_{(\theta)}$).**

$$\frac{\partial}{\delta\theta}[\delta V(\cos(\theta), \phi)] = \frac{\partial\cos(\theta)}{\partial\theta}\frac{\partial\delta V}{\partial\cos(\theta)} \qquad \text{(B.11)}$$

Where I have used the chain rule. Taking the derivative of $\cos(\theta)$ with respect to $\theta$ and substituting in (B.10) for $\delta V$ we have:

$$\frac{\partial\delta V}{\partial\theta} = -\sin(\theta)\frac{\partial}{\partial\cos(\theta)}[P_l^m(\cos(\theta))\Phi_l^m(\phi)] \qquad \text{(B.12)}$$

The derivative with respect to $\cos(\theta)$ affects only the $P_l^m$ term:

$$\frac{\partial \delta V}{\partial \theta} = -\sin(\theta)\Phi_l^m(\phi)\frac{\partial}{\partial \cos(\theta)}[P_l^m(\cos(\theta))] \tag{B.13}$$

Where the derivative of a Legendre polynomial will defined in the following manner:

$$\frac{\partial}{\partial \cos(\theta)}[P_l^m(\cos(\theta))] \triangleq P_{l(c\theta)}^m \tag{B.14}$$

$$\boxed{\frac{dP_l^m}{d\ell} = \frac{m\ell P_l^m - (l+m)(l-m+1)\sqrt{1-\ell^2}P_l^{m-1}}{1-\ell^2}} \tag{B.15}$$

Where $\ell = \cos\theta$. This expression has an issue at the degree (i.e., $m$) endpoint when $m = 0$ and therefore $m - 1 = -1$. Below is what happens when $m = 0$:

$$\frac{dP_l^0}{d\ell} = -\frac{l(l+1)}{\sqrt{1-\ell^2}}P_l^{-1} \tag{B.16}$$

Negative degree Legendre to their positive counterpart shown below:

$$P_l^{-m} = (-1)^m\frac{(l-m)!}{(l+m)!}P_l^m \tag{B.17}$$

Plug (B.17) into (B.16) gives:

$$\frac{dP_l^0}{d\ell} = -\frac{[l(l+1)]}{\sqrt{1-\ell^2}}\left[\frac{(l-1)!}{(l+1)!}\right]P_l^1 \tag{B.18}$$

$$= -\frac{[l(l+1)]}{\sqrt{1-\ell^2}}\left[-\frac{1}{l(l+1)}\right]P_l^1 \tag{B.19}$$

$$\boxed{\frac{dP_l^0}{d\ell} = \frac{P_l^1}{\sqrt{1-\ell^2}}} \tag{B.20}$$

Therefore, we now have two expressions for $P_{l(\ell)}^m$:

$$P_{l(\ell)}^m = \begin{cases} \dfrac{P_l^1}{\sqrt{1-\ell^2}} & (m = 0) \\[2ex] \dfrac{muP_l^m - (l+m)(l-m+1)\sqrt{1-\ell^2}P_l^{m-1}}{1-\ell^2} & (m > 0) \end{cases} \tag{B.21}$$

The above expression has a special case for evaluating the derivative of $dP_l^0$ and the general expression for orders $m$ greater than 0. It is important to use this expression over others to avoid another end point issue. So the derivative of the basis function (B.10) with respect to $\theta$ is:

$$\delta V_{(\theta)} = -\sin(\theta)P_{l(c\theta)}^m \Phi_l^m \tag{B.22}$$

### B.1.3.2 Derivative of the basis function with respect to $\phi$ ($\delta V_{(\phi)}$).

$$\frac{\partial \delta V}{\partial \phi} = \frac{\partial}{\partial \phi}[P_l^m(\cos(\theta))\Phi_l^m(\phi)] \tag{B.23}$$

Plugging in (B.9) for $\Phi_l^m(\phi)$ and moving all non-$\phi$ terms out gives:

$$\frac{\partial \delta V}{\partial \phi} = P_l^m(\cos(\theta))\frac{\partial}{\partial \phi}[x_c^{lm}\cos(m\phi) + x_s^{lm}\sin(m\phi)] \tag{B.24}$$

Applying the derivative gives:

$$\frac{\partial \delta V}{\partial \phi} = P_l^m(\cos(\theta))m[-x_c^{lm}\sin(m\phi) + x_s^{lm}\cos(m\phi)] \tag{B.25}$$

Where now I can define $\Phi_{l(\phi)}^m$:

$$\Phi_{l(\phi)}^m = m[-x_c^{lm}\sin(m\phi) + x_s^{lm}\cos(m\phi)] \tag{B.26}$$

Now I can define the derivative of the basis function $\delta V$ with respect to $\phi$ as shown

below:

$$\delta V_{(\phi)} = P_l^m \Phi_{l(\phi)}^m \qquad \text{(B.27)}$$

**B.1.3.3  Second derivative of the basis function with respect to $\theta$ and $\phi$,** $\left(\delta V_{(\theta,\phi)}\right)$. Another term that will be needed often is the second partial derivative of $\delta V$ with respect to $\phi$ and $\theta$, I show this below:

$$\frac{\partial^2 \delta V}{\partial \phi \partial \theta} = \frac{\partial^2}{\partial \phi \partial \theta}[P_l^m \Phi_l^m] \qquad \text{(B.28)}$$

Applying the derivative to the appropriate terms:

$$\frac{\partial^2 \delta V}{\partial \phi \partial \theta} = \frac{\partial P_l^m}{\partial \theta} \frac{\partial \Phi_l^m}{\partial \phi} \qquad \text{(B.29)}$$

Using equations (B.21) and (B.26) and defining $\delta V_{(\theta\phi)}$ we have:

$$\delta V_{(\theta,\phi)} = -\sin(\theta) P_{l(c\theta)}^m \Phi_{l(\phi)}^m \qquad \text{(B.30)}$$

**B.1.3.4  Summary of Derivatives.** Equations (B.10), (B.22), (B.26) and (B.30) define the basis function and some derivatives. They are summarized in Table B.1.

Table B.1. Basis Function & Derivatives

| | |
|---|---|
| $\delta V = P_l^m \Phi_l^m$ | (B.10) |
| $P_l^m(\cos(\theta)) = \frac{(-1)^m}{2^l l!}\sqrt{(1-\cos^2(\theta))^m}\frac{d^{l+m}}{d\cos(\theta)^{l+m}}\left[(\cos^2(\theta)-1)^l\right]$ | (B.4) |
| $\Phi_l^m(\phi) \triangleq [x_c^{lm}cos(m\phi) + x_s^{lm}sin(m\phi)]$ | (B.9) |
| $\delta V_{(\theta)} = -\sin(\theta) P_{l(c\theta)}^m \Phi_l^m$ | (B.22) |
| $\delta V_{(\phi)} = P_l^m \Phi_{l(\phi)}^m$ | (B.27) |
| $\delta V_{(\theta,\phi)} = -\sin(\theta) P_{l(c\theta)}^m \Phi_{l(\phi)}^m$ | (B.30) |
| $P_{l(\ell)}^m = \frac{mu P_l^m - (l+m)(l-m+1)\sqrt{1-\ell^2}P_l^{m-1}}{1-\ell^2}$ | (B.15) |
| $\Phi_{l(\phi)}^m = m[-x_c^{lm}\sin(m\phi) + x_s^{lm}\cos(m\phi)]$ | (B.26) |

There are three mathematical operations that must be done on $\delta V$ to produce

an expression for $\delta a_{exb}$ I have listed them below:

1. Take the gradient of $\delta V$ to produce: $\vec{\nabla} V = \left[ \delta V_{(r)} \hat{r}, \quad \delta V_{(\theta)} \hat{\theta}, \quad \delta V_{(\phi)} \hat{\phi} \right]$

2. Compute the ion drift: $\delta \vec{v}_\perp = \frac{-\vec{\nabla} V \times \vec{B}}{B^2}$

3. Compute the convection term: $\vec{\nabla} \cdot (N \delta \vec{v}_\perp)$

These three steps are completed in Sections B.1.4, B.1.5 and B.1.6 below.

**B.1.4  Definition of $\vec{\nabla} \delta V$.**  Using Eq. (B.6) I operate on (B.10):

$$\vec{\nabla} \delta V = \left[ \frac{\partial}{\partial r} \hat{r}, \frac{1}{r} \frac{\partial}{\partial \theta} \hat{\theta}, \frac{1}{r \sin(\theta)} \frac{\partial}{\partial \phi} \hat{\phi} \right] [P_l^m(\cos(\theta)) \Phi_l^m(\phi)] \tag{B.31}$$

**B.1.4.1  Applying the $\hat{r}$ operator.**  There are no $r$ variables in the expression for $\delta V$ so the derivative with respect to $r$ is equal to zero.

$$\boxed{\delta V_{(r)} = 0} \tag{B.32}$$

**B.1.4.2  Applying the $\hat{\theta}$ operator.**

$$\frac{1}{r} \frac{\partial}{\partial \theta} [\delta V]] \hat{\theta} = \frac{1}{r} \delta V_{(\theta)} \hat{\theta} \tag{B.33}$$

As a reminder by using Eq. (B.22) we have:

$$\boxed{\frac{1}{r} \delta V_{(\theta)} \hat{\theta} = \frac{-\sin(\theta)}{r} P_{l(c\theta)}^m \Phi_l^m \hat{\theta}} \tag{B.34}$$

**B.1.4.3  Applying the $\hat{\phi}$ operator.**

$$\frac{1}{r \sin(\theta)} \frac{\partial}{\partial \phi} [\delta V] \hat{\phi} = \frac{1}{r \sin(\theta)} \delta V_{(\phi)} \hat{\phi} \tag{B.35}$$

Where the expression for $\delta V_{(\phi)}$ (B.27) is shown below as a reminder:

$$\boxed{\frac{1}{r\sin(\theta)}\delta V_{(\phi)}\hat{\phi} = \frac{m}{r\sin(\theta)}P_l^m\Phi_{(\theta)}\hat{\phi}} \tag{B.36}$$

Equations (B.32), (B.34) and (B.35) and form the gradient of $\delta V$: $\vec{\nabla}\delta V = \left[0\hat{r}, \ \frac{1}{r}\delta V_{(\theta)}\hat{\theta}, \ \frac{1}{r\sin(\theta)}\delta V_{(\phi)}\hat{\phi}\right]$. Now I may begin the next step of computing the magnetic field perpendicular ion drifts, $\delta\vec{v}_\perp$.

**B.1.5 Defining $\delta\vec{v}_\perp$.** Evaluating all components to $\vec{\nabla}\delta V$ means I have also determined the electric field term, $\delta\vec{E} = -\vec{\nabla}\delta V$. Now I can determine the form of $(\delta\vec{E}\times\vec{B})/B^2$. I model the Earth's magnetic field strength in the $\hat{\phi}$ direction as zero for a dipole in magnetic field coordinates. I have the following two expressions for $\vec{B}$ and $-\vec{\nabla}V$:

$$\vec{B} = [B_r\hat{r}, \ B_\theta\hat{\theta}, \ 0\hat{\phi}] \tag{B.37}$$

$$\delta E = -\vec{\nabla}V = \left[0\hat{r}, \ -\frac{1}{r}\delta V_{(\theta)}\hat{\theta}, \ -\frac{1}{r\sin(\theta)}\delta V_{(\phi)}\hat{\phi}\right] \tag{B.38}$$

Taking the cross product between $\delta\vec{E}$ and $\vec{B}$ gives:

$$\boxed{\delta\vec{v}_\perp = (\delta\vec{E}\times\vec{B})/B^2 = \frac{1}{B^2}\left[\frac{B_\theta}{r\sin(\theta)}\delta V_{(\phi)}\hat{r} \ \ -\frac{B_r}{r\sin(\theta)}\delta V_{(\phi)}\hat{\theta} \ \ \frac{B_r}{r}\delta V_{(\theta)}\hat{\phi}\right]} \tag{B.39}$$

$$B^2 = B_r^2 + B_\theta^2 \tag{B.40}$$

Where I used $B^2$ to represent $B^2$ for simplifying the notation. Computation of equation (B.39) was the goal of this section. It represents the field perpendicular ion drift velocities $(\delta\vec{v}_\perp)$ expressed in geomagnetic coordinates. For now, it is best to leave this in symbolic form. In the next step I will apply the necessary derivatives and expand there.

**B.1.6 Definition of: $\vec{\nabla}\cdot(N\delta\vec{v}_\perp)$.** Now I can use equation (B.39) and the spherical

del operator to compute the final step. First I distribute the $\vec{\nabla}$ operator as shown in Eq. (B.7). The first term of Eq. (B.7) $(-\vec{\nabla}N \cdot \delta\vec{v}_\perp)$ is the gradient of the plasma density $\left[\frac{\partial N}{\partial r}\hat{r}, \quad \frac{1}{r}\frac{\partial N}{\partial \theta}\hat{\theta}, \quad \frac{1}{r\sin(\theta)}\frac{\partial N}{\partial \phi}\hat{\phi}\right]$ dotted with $\delta\vec{v}_\perp$. The gradient of plasma $\vec{\nabla}N$ is already done in previous work [3]. The 2nd term $(-N\vec{\nabla} \cdot \delta\vec{v}_\perp)$ is broken down into three terms and will be evaluated separately in the following subsections. Next, I show the divergence of a vector using the spherical del operator applied to a general vector, $\vec{A}$, in spherical coordinates:

$$\vec{\nabla} \cdot \vec{A} = \frac{1}{r^2}\frac{\partial(r^2 A_r)}{\partial r} + \frac{1}{r\sin(\theta)}\frac{\partial(\sin(\theta)A_\theta))}{\partial \theta} + \frac{1}{r\sin(\theta)}\frac{\partial A_\phi}{\partial \phi} \tag{B.41}$$

Where $\vec{A} = \left[A_r\hat{r}, \quad A_\theta\hat{\theta}, \quad A_\phi\hat{\phi}\right]$. Next I show this when applied to $\delta\vec{E}$.

$$-N\vec{\nabla} \cdot \delta\vec{v}_\perp =$$

$$\left\{ \underbrace{-\frac{N}{r^2 B^2}\frac{\partial}{\partial r}\left[r^2\left(\frac{B_\theta}{r\sin(\theta)}\delta V_{(\phi)}\right)\right] - \frac{N}{r\sin(\theta)B^2}\frac{\partial}{\partial \theta}\left[\sin(\theta)\left(-\frac{B_r}{r\sin(\theta)}\delta V_{(\phi)}\right)\right]}_{r\ term \qquad\qquad\qquad\qquad\qquad\qquad \theta\ term} \right.$$

$$\left. \underbrace{-\frac{N}{r\sin(\theta)B^2}\frac{\partial}{\partial \phi}\left[\frac{B_r}{r}\delta V_{(\theta)}\right]}_{\phi\ term} \right\} \tag{B.42}$$

Where I have assumed that the Earth's magnetic field $\vec{B}$ does vary with space. This is an assumption and this algorithm can me modified later to include these changes as well.

**B.1.6.1  The r Term.** Canceling the $r$:

$$-\frac{N}{r^2 B^2}\frac{\partial}{\partial r}\left[r\left(\frac{B_\theta}{\sin(\theta)}\delta V_{(\phi)}\right)\right] \tag{B.43}$$

Applying the derivative:

$$\boxed{\text{The } r \text{ term} = -\frac{NB_\theta}{r^2 B^2 \sin(\theta)}\delta V_{(\phi)}} \tag{B.44}$$

**B.1.6.2  The $\theta$ Term.** As a reminder the $\theta$ term from Eq. (B.42) is:

$$-\frac{N}{r\sin(\theta)B^2}\frac{\partial}{\partial\theta}\left[\sin(\theta)\left(-\frac{B_r}{r\sin(\theta)}\delta V_{(\phi)}\right)\right] \tag{B.45}$$

Canceling the $\sin(\theta)$ and applying the derivative to $\delta V_{(\phi)}$ gives:

$$-\frac{N}{r\sin(\theta)B^2}\left[-\frac{B_r}{r}\delta V_{(\phi,\theta)}\right] \tag{B.46}$$

I can stop here and define the $\theta$ term because $\delta V_{(\theta,\phi)}$ was defined previously as Eq. (B.30).

$$\boxed{\text{The } \theta \text{ term} = \frac{B_r N}{r^2 \sin(\theta)B^2}\delta V_{(\phi,\theta)}} \tag{B.47}$$

**B.1.6.3  The $\phi$ Term.** As a reminder, the $\phi$ term in equation (B.42) is:

$$-\frac{N}{r\sin(\theta)B^2}\frac{\partial}{\partial\phi}\left[\frac{B_r}{r}\delta V_{(\theta)}\right] \tag{B.48}$$

Distributing the derivative and moving all non-$\phi$ terms out:

$$-\frac{B_r N}{r^2 \sin(\theta)B^2}\frac{\partial}{\partial\phi}\delta V_{(\theta)} \tag{B.49}$$

Using equation (B.30) for $\delta V_{(\theta,\phi)}$ defines the $\phi$ term:

$$\boxed{\text{The } \phi \text{ term} = -\frac{B_r}{r^2 \sin(\theta)B^2}\delta V_{(\theta,\phi)}} \tag{B.50}$$

**B.1.7  Summary.**  Summing all three of the terms (Eqs. (B.44), (B.47) and (B.50))

and applying the negative sign this gives us the analytic form for corrections to the divergence of plasma, Eq. (B.5):

$$
\delta a_{exb} = -\vec{\nabla} \cdot (N \delta \vec{v}_\perp) = \underbrace{-\frac{N B_\theta}{r^2 B^2 \sin(\theta)} \delta V_{(\phi)}}_{\text{The } r \text{ term}}
$$

$$
\underbrace{+ \frac{B_r N}{r^2 \sin(\theta) B^2} \delta V_{(\phi,\theta)}}_{\text{The } \theta \text{ term}}
$$

$$
\underbrace{- \frac{B_r N}{r^2 \sin(\theta) B^2} \delta V_{(\theta,\phi)}}_{\text{The } \phi \text{ term}} \tag{B.51}
$$

$$
\underbrace{-\frac{N}{B^2} \left[ (\frac{B_\theta}{r\sin(\theta)} \delta V_{(\phi)})\hat{r} \quad -(\frac{B_r}{r\sin(\theta)} \delta V_{(\phi)})\hat{\theta} \quad (\frac{B_r}{r} \delta V_{(\theta)})\hat{\phi} \right] \cdot \left[ \frac{\partial N}{\partial r}\hat{r} \quad \frac{1}{r}\frac{\partial N}{\partial \theta}\hat{\theta} \quad \frac{1}{r\sin(\theta)}\frac{\partial N}{\partial \phi}\hat{\phi} \right]}_{\delta \vec{v}_\perp \cdot \vec{\nabla} N}
$$

The 2nd and 3rd terms cancel to get:

$$
\delta a_{exb} = -\vec{\nabla} \cdot (N \delta \vec{v}_\perp) = \underbrace{-\frac{N B_\theta}{r^2 B^2 \sin(\theta)} \delta V_{(\phi)}}_{\text{The } r \text{ term}}
$$

$$
\underbrace{-\frac{N}{B^2} \left[ (\frac{B_\theta}{r\sin(\theta)} \delta V_{(\phi)})\hat{r} \quad -(\frac{B_r}{r\sin(\theta)} \delta V_{(\phi)})\hat{\theta} \quad (\frac{B_r}{r} \delta V_{(\theta)})\hat{\phi} \right] \cdot \left[ \frac{\partial N}{\partial r}\hat{r} \quad \frac{1}{r}\frac{\partial N}{\partial \theta}\hat{\theta} \quad \frac{1}{r\sin(\theta)}\frac{\partial N}{\partial \phi}\hat{\phi} \right]}_{\delta \vec{v}_\perp \cdot \vec{\nabla} N}
$$

$$\tag{B.52}$$

At this point I have determined the final form of $\delta a_{exb}$ as a function of $\theta$ and $\phi$ however, this is only a two dimensional function. If one is to model Earth as a three dimensional system then one approach is to assume Earth's magnetic field is a dipole. This allows us to make use of the equation of a field line to define a three dimensional system with one constraint. Thereby we are reducing the degrees of freedom by one and we effectively have two variables and we may retain two term in our basis

function. How this is done is described in the following section.

## B.2 Extending the Spherical Harmonic Basis Function to Three Dimensions Using the Equation for a Dipole Field Line

For the electric potential of Earth, it is known that the potential is constant along a field line. Where now the voltage $V$ will be defined as a function of $R_{eq}$ and $\phi$ instead of $\cos(\theta)$ and $\phi$. Our new basis function has been modified from (B.10) below:

$$\delta V = P_l^m(R_{eq})\Phi_l^m(\phi) \tag{B.53}$$

Where the equatorial radius ($R_{eq}$) for a dipole is:

$$R_{eq} = \frac{r}{\sin^2[\theta]} \tag{B.54}$$

Where $R_{eq}$ is the location at which a dipole field line crosses the geomagnetic equator in meters. Using this definition, it can be proven that the gradient of the potential along a field line is zero (possibly add this section later).

**B.2.1 Derivatives of $\delta V$, Field Line.** The derivatives of $\delta V$ will now include a change with respect to $r$. Below I add those relevant derivatives to Table B.1.

**B.2.1.1 Derivative with respect to $r$.**

$$\frac{\partial \delta V}{\partial r} = \frac{\partial \delta V}{\partial R_{eq}}\frac{\partial R_{eq}}{\partial r} \tag{B.55}$$

Where:

$$\frac{\partial R_{eq}}{\partial r} = \frac{1}{\sin^2(\theta)} \tag{B.56}$$

and

$$\frac{\partial \delta V}{\partial R_{eq}} = \boxed{\delta V_{(R_{eq})} = P_{l(R_{eq})}^m \Phi_l^m} \tag{B.57}$$

Previously, $P_{l(\ell)}^m$ was defined as equation (B.15) with $\cos(\theta)$ as the argument. Now we substitute in $R_{eq}$ in place of $\cos(\theta)$ and the form of the equation remains the same:

$$P_{l(R_{eq})}^m = \frac{1}{2\sqrt{1-R_{eq}^2}}\left[(l+m)(l-m+1)P_l^{m-1} - P_l^{m+1}\right] \tag{B.58}$$

We can define the derivative of

$$\delta V_{(r)} = \frac{\delta V_{(R_{eq})}}{\sin^2(\theta)} \tag{B.59}$$

### B.2.2  Derivative with Respect to $\theta$.

$$\frac{\partial \delta V}{\partial \theta} = \frac{\partial \delta V}{\partial R_{eq}}\frac{\partial R_{eq}}{\partial \theta} \tag{B.60}$$

Where

$$\frac{\partial R_{eq}}{\partial \theta} = -\frac{2r}{\tan(\theta)\sin^2(\theta)} \tag{B.61}$$

Where we can define the basis function's derivative with respect to $\theta$ as:

$$\frac{\partial \delta V}{\partial \theta} = -\frac{2r}{\tan(\theta)\sin^2(\theta)}\delta V_{(R_{eq})} \tag{B.62}$$

Some alternate forms that may be useful are:

$$\frac{\partial \delta V}{\partial \theta} = -\frac{2R_{eq}}{\tan(\theta)}\delta V_{(R_{eq})} = -\frac{2r}{\tan(\theta)}\delta V_{(r)} \tag{B.63}$$

I will choose to use the relationship with respect to $\delta V_{(r)}$

$$\delta V_{(\theta)} = -\frac{2r}{\tan(\theta)}\delta V_{(r)} \tag{B.64}$$

### B.2.2.1  Second Derivative with Respect to $r$ and $\phi$.  Another derivative that

will be used is the second derivative of the basis function (B.10) with respect to $r$ and $\phi$. I start with the derivative with respect to $r$, $\delta V_{(r)}$ and I take the derivative with respect to $\phi$:

$$\frac{\partial \delta V_{(r)}}{\partial \phi} = \frac{\partial}{\partial \phi} \left[ \frac{P_{l(R_{eq})}^m \Phi_l^m}{\sin^2(\theta)} \right] \tag{B.65}$$

using equation (B.26) for $\frac{\partial \Phi_l^m}{\partial \phi}$ I have defined $\delta V_{(r,\phi)}$:

$$\delta V_{(r,\phi)} = \frac{P_{l(R_{eq})}^m \Phi_{l(\phi)}^m}{\sin^2(\theta)} \tag{B.66}$$

**B.2.2.2  Second Derivative with Respect to $\theta$ and $\phi$.**   To be complete, I present the form of the 2nd derivative of $\delta V$ with respect to $\theta$ and $\phi$. I start with the derivative with respect to $\theta$ and then take the derivative with respect to $\phi$

$$\frac{\partial \delta V_{(\theta)}}{\partial \phi} = -\frac{\partial}{\partial \phi} \left[ \frac{2r}{\tan(\theta)} \delta V_{(r)} \right] \tag{B.67}$$

$$\delta V_{(\theta,\phi)} = -\frac{2r}{\tan(\theta)} \frac{P_{l(R_{eq})}^m \Phi_{l(\phi)}^m}{\sin^2(\theta)} \tag{B.68}$$

$$\delta V_{(\theta,\phi)} = -\frac{2r}{\tan(\theta)} \delta V_{(r,\phi)} \tag{B.69}$$

**B.2.2.3  Summary of Derivatives.**   Table B.2 shows all the derivatives and is updated with the two new derivatives:

Next I will define the gradient of $\delta V$

**B.2.3  Definition of $\vec{\nabla}\delta V$.**

**B.2.3.1  Applying the $\hat{r}$ Operator.**   This time, there are terms that are a function of $r$. I can simply use the previously defined derivative (B.59) shown in Table B.2:

$$\frac{\partial \delta V}{\partial r} \hat{r} = \delta V_{(r)} \hat{r} \tag{B.70}$$

Table B.2. Basis Function & Derivatives Continued

| | |
|---|---|
| $\delta V = P_l^m \Phi_l^m$ | (B.10) |
| $P_l^m(\ell) = \frac{(-1)^m}{2^l l!}\sqrt{(1-\ell^2)^m}\frac{d^{l+m}}{d\ell^{l+m}}\left[(\ell^2-1)^l\right]$ | (B.4) |
| $\Phi_l^m(\phi) \triangleq [x_c^{lm}cos(m\phi) + x_s^{lm}sin(m\phi)]$ | (B.9) |
| $\delta V_{(\theta)} = -\frac{2r}{\tan(\theta)}\delta V_{(r)}$ | (B.64) |
| $\delta V_{(r)} = \frac{\delta V_{(R_{eq})}}{\sin^2(\theta)}$ | (B.59) |
| $\delta V_{(R_{eq})} = P_{l(R_{eq})}^m \Phi_l^m$ | |
| $P_{l(R_{eq})}^m = \frac{1}{2\sqrt{1-R_{eq}^2}}\left[(l+m)(l-m+1)P_l^{m-1} - P_l^{m+1}\right]$ | (B.58) |
| $\delta V_{(\phi)} = P_l^m \Phi_{l(\phi)}^m$ | (B.27) |
| $\Phi_{l(\phi)}^m = m[-x_c^{lm}\sin(m\phi) + x_s^{lm}\cos(m\phi)]$ | (B.26) |
| $\delta V_{(\theta,\phi)} = -\frac{2r}{\tan(\theta)}\delta V_{(r,\phi)}$ | (B.68) |
| $\delta V_{(r,\phi)} = \frac{P_{l(R_{eq})}^m \Phi_{l(\phi)}^m}{\sin^2(\theta)}$ | (B.66) |

### B.2.3.2 Applying the $\hat{\theta}$ Operator.

$$\frac{1}{r}\frac{\partial}{\partial\theta}[\delta V]\hat{\theta} = \frac{1}{r}\delta V_{(\theta)}\hat{\theta} \qquad (B.71)$$

As a reminder by using Eq. (B.22) we have:

$$\boxed{\frac{1}{r}\delta V_{(\theta)}\hat{\theta} = -\frac{2}{\tan(\theta)}\delta V_{(r)}\hat{\theta}} \qquad (B.72)$$

### B.2.3.3 Applying the $\hat{\phi}$ Operator. Using equation (B.27) we have the $\phi$ operator

$$\frac{1}{r\sin(\theta)}\frac{\partial}{\partial\phi}[\delta V]\hat{\phi} = \frac{1}{r\sin(\theta)}\delta V_{(\phi)}\hat{\phi} \qquad (B.73)$$

### B.2.3.4 Definition of $\delta\vec{E}$. The definition of electric field is the negative gradient of the electric potential. Equations (B.70), (B.72) and (B.73) and form the gradient of $\delta V$: $\vec{\nabla}\delta V = \left[\delta V_{(r)}\hat{r}, \quad \frac{1}{r}\delta V_{(\theta)}\hat{\theta}, \quad \frac{1}{r\sin(\theta)}\delta V_{(\phi)}\hat{\phi}\right]$. Therefore, $\delta\vec{E}$ and is defined below:

$$\delta \vec{E} = \left[ -\delta V_{(r)} \hat{r}, \quad -\frac{1}{r} \delta V_{(\theta)} \hat{\theta}, \quad -\frac{1}{r \sin(\theta)} \delta V_{(\phi)} \hat{\phi} \right] \tag{B.74}$$

$$\delta \vec{E} = \left[ E_r \ \hat{r}, \quad E_\theta \ \hat{\theta}, \quad E_\phi \ \hat{\phi} \right] \tag{B.75}$$

Now I may begin the next step of computing the magnetic field perpendicular ion drifts, $\delta \vec{v}_\perp$.

**B.2.4 Computing $\delta \vec{v}_\perp$ (3D).** Now I compute $\delta \vec{v}_\perp$ just as it was done in Section B.1.5.

$$\delta \vec{v}_\perp = \frac{-\vec{\nabla} \delta V \times \vec{B}}{||B^2||} = \frac{\delta \vec{E} \times \vec{B}}{||B^2||} \tag{B.76}$$

$$-\vec{\nabla} V \times \vec{B} = \left[ -\delta V_{(r)} \hat{r}, \quad -\frac{1}{r} \delta V_{(\theta)} \hat{\theta}, \quad -\frac{1}{r \sin(\theta)} \delta V_{(\phi)} \hat{\phi} \right] \times \left[ B_r \hat{r} \quad B_\theta \hat{\theta} \quad 0 \right] \tag{B.77}$$

Crossing the two terms gives:

$$\delta \vec{v}_\perp = \frac{1}{B^2} \left[ \frac{1}{r \sin(\theta)} \delta V_{(\phi)} B_\theta \hat{r} \quad -\frac{1}{r \sin(\theta)} \delta V_{(\phi)} B_r \hat{\theta} \quad (\frac{1}{r} \delta V_{(\theta)} B_r - \delta V_{(r)} B_\theta) \hat{\phi} \right] \tag{B.78}$$

Now I can compute the divergence.

**B.2.5 Creating a Matrix $\mathbf{H}_{(exb)}$ for $\delta a_{exb}$ by Defining A and B Submatrices and Using the CTIP Model for $\vec{\nabla} \cdot \delta \vec{v}_\perp$.** I can define the $\mathbf{H}$ matrix by defining two submatrices $\mathbf{A}$ and $\mathbf{B}$. Where submatrix $\mathbf{A}$ contains all physics and the divergence operators and submatrix $\mathbf{B}$ contains only first derivative operators on the given basis functions. The idea is to separate the terms so those terms that are specific to the chosen basis function are separated from those terms that are general for any chosen basis function. Starting with the definition of $\delta a_{exb}$ we have:

$$\delta a_{exb} = -\delta \vec{v}_\perp \cdot \vec{\nabla} N - N \vec{\nabla} \cdot \delta \vec{v}_\perp \tag{B.79}$$

Where by using the CTIP model as explained in [15] (see Eq. (25) therein) we can define an expression for the 2nd term $\vec{\nabla} \cdot \delta \vec{v}_\perp$ as shown below:

$$\vec{\nabla} \cdot \vec{v}_\perp = \frac{6E_\phi \cos I (1 + \cos^2 \theta)}{||\vec{B}|| r (1 + 3 \cos^2 \theta)} \tag{B.80}$$

Where, $E_\phi$, is the electric field vector component in the longitudinal direction or $\hat{\phi}$ direction and $I$ is the dip angle defined by:

$$\cos I = \frac{\sin \theta}{\sqrt{1 + 3 \cos^2 \theta}} \tag{B.81}$$

I can substitute the expression for $E_\phi$ as defined by (B.75) to get an expression with a derivative of the basis function:

$$\vec{\nabla} \cdot \vec{v}_\perp = -\frac{6 \delta V_{(\phi)} \cos I (1 + \cos^2 \theta)}{||\vec{B}|| r^2 \sin \theta (1 + 3 \cos^2 \theta)} \tag{B.82}$$

Now I may use Eq. (B.82) with the definition for $\delta a_{exb}$ shown in Eq. (B.79).

$$\delta a_{exb} = -\delta \vec{v}_\perp \cdot \vec{\nabla} N + N \frac{6 \delta V_{(\phi)} \cos I (1 + \cos^2 \theta)}{||\vec{B}|| r^2 \sin \theta (1 + 3 \cos^2 \theta)} \tag{B.83}$$

Now I must add in the expression for $-\delta \vec{v}_\perp \cdot \vec{\nabla} N$ which is:

$$
\begin{aligned}
- \delta \vec{v}_\perp \cdot \vec{\nabla} N = \\
- \frac{1}{B^2} \left[ \frac{B_\theta}{r \sin \theta} \frac{\partial N}{\partial r} \delta V_{(\phi)} - \frac{B_r}{r^2 \sin \theta} \frac{\partial N}{\partial \theta} \delta V_{(\phi)} + \frac{B_r}{r^2 \sin \theta} \frac{\partial N}{\partial \phi} \delta V_{(\theta)} - \frac{B_\theta}{r \sin \theta} \frac{\partial N}{\partial \phi} \delta V_{(r)} \right]
\end{aligned}
\tag{B.84}
$$

Using the expression from eq. (B.64) for $\delta V_{(\theta)}$ in terms of $\delta V_{(r)}$:

$$\delta V_{(\theta)} = -\frac{2r}{\tan \theta} \delta V_{(r)} \tag{B.85}$$

Plugging the above expression into Eq. (B.84) gives:

$$-\delta\vec{v}_\perp \cdot \vec{\nabla}N =$$
$$-\frac{1}{B^2}\left[\frac{B_\theta}{r\sin\theta}\frac{\partial N}{\partial r}\delta V_{(\phi)} - \frac{B_r}{r^2\sin\theta}\frac{\partial N}{\partial\theta}\delta V_{(\phi)} - \frac{2B_r}{r\tan\theta\sin\theta}\frac{\partial N}{\partial\phi}\delta V_{(r)} - \frac{B_\theta}{r\sin\theta}\frac{\partial N}{\partial\phi}\delta V_{(r)}\right]$$

(B.86)

For simplification I pull a $\frac{1}{r\sin\theta}$ term out:

$$-\delta\vec{v}_\perp \cdot \vec{\nabla}N =$$
$$-\frac{1}{B^2 r\sin\theta}\left[B_\theta\frac{\partial N}{\partial r}\delta V_{(\phi)} - \frac{B_r}{r}\frac{\partial N}{\partial\theta}\delta V_{(\phi)} - \frac{2B_r}{\tan\theta}\frac{\partial N}{\partial\phi}\delta V_{(r)} - B_\theta\frac{\partial N}{\partial\phi}\delta V_{(r)}\right]$$

(B.87)

Now I may organize like terms of the derivatives of $\delta V$:

$$\boxed{-\delta\vec{v}_\perp \cdot \vec{\nabla}N = -\frac{1}{B^2 r\sin\theta}\left[\left(B_\theta\frac{\partial N}{\partial r} - \frac{B_r}{r}\frac{\partial N}{\partial\theta}\right)\delta V_{(\phi)} - \left(\frac{2B_r}{\tan\theta} + B_\theta\right)\frac{\partial N}{\partial\phi}\delta V_{(r)}\right]}$$

(B.88)

Now I may add together Eq. (B.88) and (B.82) to get a form for $\delta a_{exb}$

$$\delta a_{exb} = -\frac{1}{B^2 r\sin\theta}\left[\left(B_\theta\frac{\partial N}{\partial r} - \frac{B_r}{r}\frac{\partial N}{\partial\theta}\right)\delta V_{(\phi)} - \left(\frac{2B_r}{\tan\theta} + B_\theta\right)\frac{\partial N}{\partial\phi}\delta V_{(r)}\right]$$
$$+ \frac{6N\delta V_{(\phi)}\cos I(1+\cos^2\theta)}{||\vec{B}||r^2\sin\theta(1+3\cos^2\theta)}$$

(B.89)

Again, reorganizing in terms of derivatives of $\delta V$:

$$\delta a_{exb} =$$
$$\underbrace{\left[-\frac{1}{B^2 r\sin\theta}\left(B_\theta\frac{\partial N}{\partial r} - \frac{B_r}{r}\frac{\partial N}{\partial\theta}\right) + \frac{6N\cos I(1+\cos^2\theta)}{||\vec{B}||r^2\sin\theta(1+3\cos^2\theta)}\right]}_{=a_1}\delta V_{(\phi)}$$
$$\underbrace{+ \frac{1}{B^2 r\sin\theta}\left(\frac{2B_r}{\tan\theta} + B_\theta\right)\frac{\partial N}{\partial\phi}}_{=a_2}\delta V_{(r)}$$

(B.90)

Where I have defined the $a_1$ and $a_2$ terms that are analogous to the terms shown in

[15]. There is only one difference and that is a $\frac{1}{sin^2\theta}$ term that is pulled out of the derivative of the power series basis function with respect to $r$. For spherical harmonics that $\frac{1}{\sin^2\theta}$ term does not come out the same. Next, I can expand the derivative terms by plugging in Eqs. (B.59) and (B.27)

$$\delta a_{exb} = a_1 P_l^m \Phi_{l(\phi)}^m - a_2 \frac{\delta V_{(R_{eq})}}{\sin^2(\theta)} \tag{B.91}$$

Plugging in Eq. (B.57) for $\delta V_{(R_{eq})}$:

$$\delta a_{exb} = a_1 P_l^m \Phi_{l(\phi)}^m + a_2 \frac{P_{l(R_{eq})}^m \Phi_l^m}{\sin^2(\theta)} \tag{B.92}$$

Plugging in Eqs. (B.26) and (B.9) to expand the terms containing the coefficients to be solved for:

$$\delta a_{exb} = a_1 P_l^m m[-x_c^{lm}\sin(m\phi) + x_s^{lm}\cos(m\phi)] + a_2 \frac{1}{\sin^2(\theta)} P_{l(R_{eq})}^m [x_c^{lm}cos(m\phi) + x_s^{lm}sin(m\phi)] \tag{B.93}$$

I can rearrange the above equation and define $b$ terms:

$$
\begin{aligned}
\delta a_{exb} \;=\; & a_1 \left[ \underbrace{-mP_l^m \sin(m\phi)}_{=b_{1c}^{lm}} x_c^{lm} + \underbrace{mP_l^m \cos(m\phi)}_{=b_{1s}^{lm}} x_s^{lm} \right] \\[2mm]
+ \; & a_2 \left[ \underbrace{\frac{1}{\sin^2(\theta)} P_{l(R_{eq})}^m cos(m\phi)}_{=b_{2c}^{lm}} x_c^{lm} + \underbrace{\frac{1}{\sin^2(\theta)} P_{l(R_{eq})}^m sin(m\phi)}_{=b_{2s}^{lm}} x_s^{lm} \right]
\end{aligned} \tag{B.94}
$$

With the definition of $a_1$, $a_2$, $b_{1c}^{lm}$, $b_{1s}^{lm}$, $b_{2c}^{lm}$ and $b_{2s}^{lm}$ we may express $\delta a_{exb}$ as:

$$\delta a_{exb} = a_1 \left[ b_{1c}^{lm} x_c^{lm} + b_{1s}^{lm} x_s^{lm} \right] + a_2 \left[ b_{2c}^{lm} x_c^{lm} + b_{2s}^{lm} x_s^{lm} \right] \tag{B.95}$$

Given that there are multiple grid points we may represent this as two matrices $A$

and $B$ where $A$ is defined as:

$$\mathbf{A} = \begin{bmatrix} a_1 & a_2 \end{bmatrix}_i \tag{B.96}$$

and $B$ as:

$$\mathbf{B} = \begin{bmatrix} b_{1c}^{10} & b_{1c}^{11} & \cdots & b_{1c}^{lm} & b_{1s}^{10} & b_{1s}^{11} & \cdots & b_{1s}^{lm} \\ b_{2c}^{10} & b_{2c}^{11} & \cdots & b_{2c}^{lm} & b_{2s}^{10} & b_{2s}^{11} & \cdots & b_{2s}^{lm} \end{bmatrix}_i \tag{B.97}$$

So now we may represent $\delta a_{exb}$ as:

$$\delta a_{exb} = \mathbf{Hx} = \mathbf{ABx}$$

$$= \begin{bmatrix} a_1 & a_2 \end{bmatrix}_i \begin{bmatrix} b_{1c}^{10} & b_{1c}^{11} & \cdots & b_{1c}^{lm} & b_{1s}^{10} & b_{1s}^{11} & \cdots & b_{1s}^{lm} \\ b_{2c}^{10} & b_{2c}^{11} & \cdots & b_{2c}^{lm} & b_{2s}^{10} & b_{2s}^{11} & \cdots & b_{2s}^{lm} \end{bmatrix}_i \begin{bmatrix} x_c^{10} \\ x_c^{11} \\ \vdots \\ x_c^{lm} \\ x_s^{10} \\ x_s^{11} \\ \vdots \\ x_s^{lm} \end{bmatrix} \tag{B.98}$$

Where $\mathbf{A}$ and $\mathbf{B}$ is equal to our mapping matrix $\mathbf{H}$. The Table B.3 shows the terms I have just defined for quick reference.

## B.3  Using L-shell for the Legendre Polynomial's Independent Variable and Mapping it to a Domain from -1 to 1

The Legendre Polynomials are defined from -1 to 1. As such, the MATLAB function (legendre.m) for computing them requires them to be from -1 to 1. Rather

Table B.3. Term for the **H** matrix using **A** and **B** Matrices

| | |
|---|---|
| $\mathbf{H} = \mathbf{AB}$ | |
| $\mathbf{A} = \begin{bmatrix} a_1 & a_2 \end{bmatrix}_i$ | (B.96) |
| $a_1 = -\frac{1}{B^2 r \sin\theta}\left(B_\theta \frac{\partial N}{\partial r} - \frac{B_r}{r}\frac{\partial N}{\partial \theta}\right) + \frac{6N\cos I(1+\cos^2\theta)}{\|\vec{B}\| r^2 \sin\theta(1+3\cos^2\theta)}$ | (B.90) |
| $a_2 = -\frac{1}{B^2 r \sin\theta}\left(\frac{2B_r}{\tan\theta} + B_\theta\right)\frac{\partial N}{\partial \phi}$ | (B.90) |
| $\mathbf{B} = \begin{bmatrix} b_{1c}^{10} & b_{1c}^{11} & \cdots & b_{1c}^{lm} & b_{1s}^{10} & b_{1s}^{11} & \cdots & b_{1s}^{lm} \\ b_{2c}^{10} & b_{2c}^{11} & \cdots & b_{2c}^{lm} & b_{2s}^{10} & b_{2s}^{11} & \cdots & b_{2s}^{lm} \end{bmatrix}_i$ | (B.97) |
| $b_{1c}^{lm} = -mP_l^m \sin(m\phi)$ | (B.94) |
| $b_{1s}^{lm} = mP_l^m \cos(m\phi)$ | (B.94) |
| $b_{2c}^{lm} = \frac{1}{\sin^2(\theta)}P_{l(R_{eq})}^m \cos(m\phi)$ | (B.94) |
| $b_{2s}^{lm} = \frac{1}{\sin^2(\theta)}P_{l(R_{eq})}^m \sin(m\phi)$ | (B.94) |
| $\mathbf{x} = \begin{bmatrix} x_c^{lm} \\ x_s^{lm} \end{bmatrix}$ | (B.98) |

than rewriting the Legendre polynomial to accept different ranges it will be faster to just use a scalar mapping to map our domain to -1 to 1.

A linear scaling mapping function maps two points in a domain to two other points. In our case we want to map the lower and upper limit of the L-shell range to -1 and 1, respectively. A general linear scaling mapping function looks like:

$$f(x) = C + \frac{C - D}{B - A}A + \frac{D - C}{B - A}x \tag{B.99}$$

f Where $A$ and $B$ are the minimum L-shell $(L_{min})$ and maximum L-shell $(L_{max})$, $C$ and $D$ are the minimum and maximum of the new domain (i.e., -1 and 1), $x$ is the L-shell, $L$ and $f(x)$ is the $\ell$ that is the independent variable of the Legendre polynomial. Our linear scaling mapping function is:

$$\ell = -1 + \frac{-2}{L_{min} - L_{max}}L_{min} + \frac{2}{L_{max} - L_{min}}L \tag{B.100}$$

Since our grid may change, this function will change automatically based on the

minimum and maximum L-shell is for any given run.

Next, I will define the function for L-shell:

$$L(R_e, r, \theta) = \frac{(r + R_e)}{R_e \sin^2(\theta)} \tag{B.101}$$

Now that we have these definitions for the argument $\ell$ inside the legendre polynomial new terms will arise when performing derivatives. The next subsections will redefine the relevant derivatives for the final mapping matrix.

**B.3.1  Derivatives of $\delta V$.**  The derivatives of $\delta V$ will contain new terms because of the scaling function and L-shell definitions. So first I will take the derivative of the scaling function with respect to $r$ and $\theta$:

$$\frac{\partial \ell}{\partial r} = \frac{\partial \ell}{\partial L} \frac{\partial L}{\partial r} \tag{B.102}$$

$$= \frac{1}{R_e \sin^2(\theta)} \frac{\partial \ell}{\partial L} \tag{B.103}$$

$$\boxed{\frac{\partial \ell}{\partial r} = \frac{1}{R_e \sin^2(\theta)} \frac{2}{L_{max} - L_{min}}} \tag{B.104}$$

and now the $\theta$ derivative

$$\frac{\partial \ell}{\partial \theta} = \frac{\partial \ell}{\partial L} \frac{\partial L}{\partial \theta} \tag{B.105}$$

$$= \frac{-2(r + R_e)}{R_e \tan(\theta) \sin^2(\theta)} \frac{\partial \ell}{\partial L} \tag{B.106}$$

$$\boxed{\frac{\partial \ell}{\partial \theta} = \frac{-2(r + R_e)}{R_e \tan(\theta) \sin^2(\theta)} \frac{2}{L_{max} - L_{min}}} \tag{B.107}$$

With the above definitions of $\partial \ell / \partial r$ and $\partial \ell / \partial \theta$ we can now include the new terms for each of the derivatives of the basis function $\delta V$. Note that the derivative with respect to $\phi$ remains the same as before so I will only be presenting that of $r$

and $\theta$

**B.3.1.1 Derivatives with respect to $r$.** Using the new derivative ((B.104)) $\delta V_r$ is now defined as:

$$\frac{\partial \delta V}{\partial r} = \frac{\partial \delta V_{(r)}}{\partial \ell} \frac{\partial \ell}{\partial r} \tag{B.108}$$

$$\boxed{\delta V_{(r)} = \frac{1}{R_e \sin^2(\theta)} \frac{2}{L_{max} - L_{min}} P_{l(\ell)}^m \Phi_l^m} \tag{B.109}$$

We can further unpack ((B.109)) using equation ((B.15)) shown later. **B.3.1.2 Derivatives with respect to $\theta$.** Using the new derivatives (eq. ((B.107))) $\delta V_{(\theta)}$ is now defined as:

$$\frac{\partial \delta V_{(\theta)}}{\partial \theta} = \frac{\partial \delta V_{(\theta)}}{\partial \theta} \tag{B.110}$$

$$= \frac{\partial \delta V_{(\theta)}}{\partial \ell} \frac{\partial \ell}{\partial \theta} \tag{B.111}$$

$$= \underbrace{\frac{-2(r + R_e)}{\tan(\theta)} \frac{2}{L_{max} - L_{min}} \frac{1}{R_e \sin^2(\theta)}}_{\frac{\partial \ell}{\partial \theta}} \underbrace{P_{l(\ell)}^m \Phi_l^m}_{\frac{\partial \delta V_{(\theta)}}{\partial \ell}} \tag{B.112}$$

Finally $\delta V_{(\theta)}$ in its most compact form:

$$\boxed{\delta V_{(\theta)} = -\frac{2(r + R_e)}{\tan(\theta)} \delta V_{(r)}} \tag{B.113}$$

This is the last derivative that will be modified from using the linear scaling matrix to scale the L-shell range to a -1 to 1 range. With the derivatives of the potential we have defined the electric field and thus with the magnetic field vector we may define the field perpendicular ion drifts just as it is done in Section B.1.5.

**B.3.1.3 Modifications to the Divergence.** We can draw from work done in Section B.2.5 to continue modifying only what is necessary. Beginning with equation

we have:

$$\delta a_{exb} = \left[ -\frac{1}{B^2 r \sin\theta} \left( B_\theta \frac{\partial N}{\partial r} - \frac{B_r}{r} \frac{\partial N}{\partial \theta} \right) + \frac{6N \cos I (1 + \cos^2\theta)}{||\vec{B}|| r^2 \sin\theta (1 + 3\cos^2\theta)} \right] \delta V_{(\phi)}$$
$$+ \frac{1}{B^2 r \sin\theta} \left( \frac{2B_r}{\tan\theta} + B_\theta \right) \frac{\partial N}{\partial \phi} \delta V_{(r)} \tag{B.114}$$

We must recognize that the value of r is not the height from the Earth's surface but that from the center of Earth or $r + R_e$, the same as it is defined for the L-shell. So I must make the necessary correction to the above equation for that:

$$\delta a_{exb} =$$
$$\underbrace{\left[ \frac{-1}{B^2 (r + R_e) \sin\theta} \left( B_\theta \frac{\partial N}{\partial r} - \frac{B_r}{(r + R_e)} \frac{\partial N}{\partial \theta} \right) + \frac{6N \cos I (1 + \cos^2\theta)}{||\vec{B}|| (r + R_e)^2 \sin\theta (1 + 3\cos^2\theta)} \right] \delta V_{(\phi)}}_{=a_1}$$
$$\underbrace{+ \frac{1}{B^2 (r + R_e) \sin\theta} \left( \frac{2B_r}{\tan\theta} + B_\theta \right) \frac{\partial N}{\partial \phi} \delta V_{(r)}}_{=a_2}$$

$$\tag{B.115}$$

From here we again define $a_1$ and $a_2$ and plug in the derivatives of $\delta V$. However, the derivative $\delta V_{(r)}$ is different because of the new scaling and so we have:

$$\delta a_{exb} = a_1 P_l^m \Phi_{l(\phi)}^m + a_2 \frac{2}{R_e \sin^2(\theta)(L_{max} - L_{min})} P_{l(\ell)}^m \Phi_l^m \tag{B.116}$$

At this point we unpack the $\Phi_l^m$ term and collect like terms of coefficients as done before.

$$\delta a_{exb} = a_1 P_l^m m[-x_c^{lm} \sin(m\phi) + x_s^{lm} \cos(m\phi)]$$
$$+ a_2 \frac{2}{R_e \sin^2(\theta)(L_{max} - L_{min})} P_{l(R_{eq})}^m [x_c^{lm} cos(m\phi) + x_s^{lm} sin(m\phi)] \tag{B.117}$$

I can rearrange the above equation and define $b$ terms:

$$\delta a_{exb} = a_1 \left[ \underbrace{-mP_l^m \sin(m\phi)}_{=b_{1c}^{lm}} x_c^{lm} + \underbrace{mP_l^m \cos(m\phi)}_{=b_{1s}^{lm}} x_s^{lm} \right]$$
$$+ a_2 \left[ \underbrace{\frac{2}{R_e \sin^2(\theta)(L_{max} - L_{min})} P_{l(\ell)}^m cos(m\phi)}_{=b_{2c}^{lm}} x_c^{lm} \right.$$
$$\left. + \underbrace{\frac{2}{R_e \sin^2(\theta)(L_{max} - L_{min})} P_{l(\ell)}^m sin(m\phi)}_{=b_{2s}^{lm}} x_s^{lm} \right] \tag{B.118}$$

From here, I follow the same steps that take us from Eq. (B.95) up to the definition of **H** in Eq. (B.98). I need not repeat the steps because they are identical. Lastly, I have updated the summary table below (Table to include the new definitions of derivatives:

## B.4 Corrections to Earth's Electric Field

In this section I describe how updates to electric fields are computed by formulating mapping matrices that map from coefficients to electric field to ion drifts. First, we start with the definition of each derivative to form the electric field vector, $\vec{E}$ using Equations B.109, B.113 and B.27 for the gradients of the electric potential corrections. The electric field vector will be defined as a $3 \times i$ matrix where $i$ corresponds to a grid point index.

$$\begin{bmatrix} \vec{E}_r \\ \vec{E}_\theta \\ \vec{E}_\phi \end{bmatrix} = \begin{bmatrix} -\delta V_{(r)} \\ -\frac{1}{(r+R_e)}\delta V_{(\theta)} \\ -\frac{1}{(r+R_e)\sin(\theta)}\delta V_{(\phi)} \end{bmatrix} \tag{B.119}$$

Where each correction to the derivative of the basis functions can be expressed as sub matrices $H_r, H_\theta$ and $H_\phi$ that map the coefficients to electric potential vector.

Table B.4. Summary: Terms for defining $\mathbf{H}$ and $\mathbf{x}$

| | |
|---|---|
| $\delta V = P_l^m \Phi_l^m$ | (B.10) |
| $P_l^m(\ell) = \frac{(-1)^m}{2^l l!}\sqrt{(1-\ell^2)^m}\frac{d^{l+m}}{d\ell^{l+m}}\left[(\ell^2-1)^l\right]$ | (B.4) |
| $\Phi_l^m(\phi) = [x_c^{lm}cos(m\phi) + x_s^{lm}sin(m\phi)]$ | (B.9) |
| $\delta V_{(\theta)} = -\frac{2(r+R_e)}{\tan(\theta)}\delta V_{(r)}$ | (B.113) |
| $\delta V_{(r)} = \frac{1}{R_e \sin^2(\theta)}\frac{2}{L_{max}-L_{min}}\delta V_{(\ell)}$ | (B.109) |
| $\delta V_{(\ell)} = P_{l(\ell)}^m \Phi_l^m$ | |
| $P_{l(\ell)}^m = \frac{m\ell P_l^m - (l+m)(l-m+1)\sqrt{1-\ell^2}P_l^{m-1}}{1-\ell^2}$ | (B.15) |
| $P_{l(\ell)}^0 = \frac{P_l^1}{\sqrt{1-\ell^2}}$ | (B.20) |
| $\delta V_{(\phi)} = P_l^m \Phi_{l(\phi)}^m$ | (B.27) |
| $\Phi_{l(\phi)}^m = m[-x_c^{lm}\sin(m\phi) + x_s^{lm}\cos(m\phi)]$ | (B.26) |
| $\mathbf{H} = \mathbf{AB}$ | |
| $\mathbf{A} = \begin{bmatrix} a_1 & a_2 \end{bmatrix}_i$ | (B.96) |
| $a_1 = -\frac{1}{B^2(r+R_e)\sin\theta}\left(B_\theta\frac{\partial N}{\partial r} - \frac{B_r}{(r+R_e)}\frac{\partial N}{\partial\theta}\right) + \frac{6N\cos I(1+\cos^2\theta)}{||\vec{B}||(r+R_e)^2\sin\theta(1+3\cos^2\theta)}$ | (B.90) |
| $a_2 = -\frac{1}{B^2(r+R_e)\sin\theta}\left(\frac{2B_r}{\tan\theta} + B_\theta\right)\frac{\partial N}{\partial\phi}$ | (B.90) |
| $\mathbf{B} = \begin{bmatrix} b_{1c}^{10} & b_{1c}^{11} & \cdots & b_{1c}^{lm} & b_{1s}^{10} & b_{1s}^{11} & \cdots & b_{1s}^{lm} \\ b_{2c}^{10} & b_{2c}^{11} & \cdots & b_{2c}^{lm} & b_{2s}^{10} & b_{2s}^{11} & \cdots & b_{2s}^{lm} \end{bmatrix}_i$ | (B.97) |
| $b_{1c}^{lm} = -mP_l^m\sin(m\phi)$ | (B.118) |
| $b_{1s}^{lm} = mP_l^m\cos(m\phi)$ | (B.118) |
| $b_{2c}^{lm} = \frac{2}{R_e\sin^2(\theta)(L_{max}-L_{min})}P_{l(\ell)}^m\cos(m\phi)$ | (B.118) |
| $b_{2s}^{lm} = \frac{2}{R_e\sin^2(\theta)(L_{max}-L_{min})}P_{l(\ell)}^m\sin(m\phi)$ | (B.118) |
| $\mathbf{x} = \begin{bmatrix} x_c^{lm} \\ x_s^{lm} \end{bmatrix}$ | (B.98) |

Expanding each derivative term we have:

$$\begin{bmatrix} \delta V_{(r)} \\ \delta V_{(\theta)} \\ \delta V_{(\phi)} \end{bmatrix} = \begin{bmatrix} \frac{1}{R_e\sin^2(\theta)}\frac{2}{L_{max}-L_{min}}P_{l(\ell)}^m\Phi_l^m \\ -\frac{2(r+R_e)}{\tan(\theta)}\delta V_{(r)} \\ \frac{1}{(r+R_e)\sin(\theta)}P_l^m\Phi_{l(\phi)}^m \end{bmatrix} \quad (B.120)$$

**B.4.1  Defining $H_r$.** Expanding $\delta V_r$ using the definition of $\Phi_l^m$ (Eq. B.9) we have:

$$\delta V_{(r)} = \left( \frac{1}{R_e \sin^2(\theta)} \frac{2}{L_{max} - L_{min}} P_{l(\ell)}^m \right) \left( x_c^{lm} \cos(m\phi) + x_s^{lm} \sin(m\phi) \right) \tag{B.121}$$

We may isolate the coefficients, $x_c^{lm}$ and $x_s^{lm}$ and give a $j$ index for the $j^{th}$ grid point:

$$\delta V_{(r)} = \underbrace{\left( \frac{\cos(m\phi)}{R_e \sin^2(\theta)} \frac{2}{L_{max} - L_{min}} P_{l(\ell)}^m \right)_j}_{\triangleq c_{rj}^{lm}} x_c^{lm} + \underbrace{\left( \frac{\sin(m\phi)}{R_e \sin^2(\theta)} \frac{2}{L_{max} - L_{min}} P_{l(\ell)}^m \right)_j}_{\triangleq s_{rj}^{lm}} x_s^{lm}$$

$$\tag{B.122}$$

We may stack this into matrix form:

$$\underbrace{\begin{bmatrix} \delta V_{(r)1} \\ \\ \delta V_{(r)2} \\ \\ \vdots \\ \\ \delta V_{(r)j} \end{bmatrix}}_{[j \times 1]} = \underbrace{\begin{bmatrix} c_{r0}^{00} & c_{r0}^{10} & \cdots & c_{r0}^{lm} & s_{r0}^{00} & s_{r0}^{10} & \cdots & s_{r0}^{lm} \\ c_{r2}^{00} & c_{r2}^{10} & \cdots & c_{r2}^{lm} & s_{r2}^{00} & s_{r2}^{10} & \cdots & s_{r2}^{lm} \\ \vdots & \vdots & \ddots & \vdots & \vdots & \vdots & \ddots & \vdots \\ c_{rj}^{00} & c_{rj}^{10} & \cdots & c_{rj}^{lm} & s_{rj}^{00} & s_{rj}^{10} & \cdots & s_{rj}^{lm} \end{bmatrix}}_{[j \times k/2] | [j \times k/2]} \underbrace{\begin{bmatrix} x_c^{10} \\ x_c^{11} \\ \vdots \\ x_c^{lm} \\ \hline x_s^{10} \\ x_s^{11} \\ \vdots \\ x_s^{lm} \end{bmatrix}}_{\substack{[k/2 \times 1] \\ \hline [k/2 \times 1]}} \tag{B.123}$$

$$\delta V_{(r)j} = \left[ \mathbf{H}_{rc} | \mathbf{H}_{rs} \right]_{jk} \begin{bmatrix} x_c^{lm} \\ \hline x_s^{lm} \end{bmatrix}_k \tag{B.124}$$

$$\boxed{\delta \vec{V}_{(r),j} = \mathbf{H}_{r,jk} \vec{x}_k} \tag{B.125}$$

Where $\mathbf{H}_{r,jk}$ is defined as:

$$\mathbf{H}_{r,jk} = \left[ \begin{array}{cccc|cccc} c_{r0}^{00} & c_{r0}^{10} & \cdots & c_{r0}^{lm} & s_{r0}^{00} & s_{r0}^{10} & \cdots & s_{r0}^{lm} \\ c_{r2}^{00} & c_{r2}^{10} & \cdots & c_{r2}^{lm} & s_{r2}^{00} & s_{r2}^{10} & \cdots & s_{r2}^{lm} \\ \vdots & \vdots & \ddots & \vdots & \vdots & \vdots & \ddots & \vdots \\ c_{rj}^{00} & c_{rj}^{10} & \cdots & c_{rj}^{lm} & s_{rj}^{00} & s_{rj}^{10} & \cdots & s_{rj}^{lm} \end{array} \right] \tag{B.126}$$

**B.4.2  Defining $H_\theta$.** $\delta E_\theta$ is defined by a term multiplied by the previously defined $\delta V_r$ (Eq. B.125):

$$\delta V_{(\theta)} = \underbrace{\frac{-2(r + R_e)}{\tan(\theta)}}_{\triangleq \vec{c}_{\theta,j}} \delta V_{(r)} \tag{B.127}$$

Plugging in Eq B.125 for $\delta V_{(r)}$:

$$\boxed{\delta V_{(\theta),j} = \vec{c}_{\theta,j} \mathbf{H}_{r,jk} \vec{x}_k} \tag{B.128}$$

**B.4.3  Defining $H_\phi$.** $\delta V_\phi$ is defined by the derivative of the harmonic term $\Phi_l^m$ as shown in Eq. (B.9)

$$\delta V_{(\phi)} = P_l^m \Phi_{l(\phi)}^m \tag{B.129}$$

$$\delta V_{(\phi)} = m P_l^m [-x_c^{lm} \sin(m\phi) + x_s^{lm} \cos(m\phi)] \tag{B.130}$$

Isolating the coefficients as done before:

$$\delta V_{(\phi)} = \underbrace{(-m P_l^m \sin(m\phi))}_{c_{\theta j}^{lm}} x_c^{lm} + \underbrace{(m P_l^m \cos(m\phi))}_{s_{\theta j}^{lm}} x_s^{lm} \tag{B.131}$$

Stacking this into matrix form:

$$
\underbrace{\begin{bmatrix} \delta V_{(\theta)1} \\ \delta V_{(\theta)2} \\ \vdots \\ \delta V_{(\theta)j} \end{bmatrix}}_{[j\times 1]} = \underbrace{\begin{bmatrix} c_{\theta 0}^{00} & c_{\theta 0}^{10} & \cdots & c_{\theta 0}^{lm} & s_{\theta 0}^{00} & s_{\theta 0}^{10} & \cdots & s_{\theta 0}^{lm} \\ c_{\theta 2}^{00} & c_{\theta 2}^{10} & \cdots & c_{\theta 2}^{lm} & s_{\theta 2}^{00} & s_{\theta 2}^{10} & \cdots & s_{\theta 2}^{lm} \\ \vdots & \vdots & \ddots & \vdots & \vdots & \vdots & \ddots & \vdots \\ c_{\theta j}^{00} & c_{\theta j}^{10} & \cdots & c_{\theta j}^{lm} & s_{\theta j}^{00} & s_{\theta j}^{10} & \cdots & s_{\theta j}^{lm} \end{bmatrix}}_{[j\times k/2]|[j\times k/2]} \underbrace{\begin{bmatrix} x_c^{10} \\ x_c^{11} \\ \vdots \\ x_c^{lm} \\ \hline x_s^{10} \\ x_s^{11} \\ \vdots \\ x_s^{lm} \end{bmatrix}}_{\begin{bmatrix}[k/2\times 1]\\ \hline [k/2\times 1]\end{bmatrix}}
\tag{B.132}
$$

$$
\delta V_{(\theta)j} = \left[\mathbf{H}_{\theta c}|\mathbf{H}_{\theta s}\right]_{jk} \begin{bmatrix} x_c^{lm} \\ \hline x_s^{lm} \end{bmatrix}_k
\tag{B.133}
$$

$$
\boxed{\delta \vec{V}_{(\theta),j} = \mathbf{H}_{\theta,jk}\vec{x}_k}
\tag{B.134}
$$

Where $\mathbf{H}_{\theta,jk}$ is defined as:

$$\mathbf{H}_{\theta,jk} = \begin{bmatrix} c_{\theta 0}^{00} & c_{\theta 0}^{10} & \cdots & c_{\theta 0}^{lm} & s_{\theta 0}^{00} & s_{\theta 0}^{10} & \cdots & s_{\theta 0}^{lm} \\ c_{\theta 2}^{00} & c_{\theta 2}^{10} & \cdots & c_{\theta 2}^{lm} & s_{\theta 2}^{00} & s_{\theta 2}^{10} & \cdots & s_{\theta 2}^{lm} \\ \vdots & \vdots & \ddots & \vdots & \vdots & \vdots & \ddots & \vdots \\ c_{\theta j}^{00} & c_{\theta j}^{10} & \cdots & c_{\theta j}^{lm} & s_{\theta j}^{00} & s_{\theta j}^{10} & \cdots & s_{\theta j}^{lm} \end{bmatrix} \tag{B.135}$$

**B.4.4 Matrix Form of Electric Potential.** We can use the definitions of $H_r$, $H_\theta$ and $H_\phi$ (Eqs. (B.126), (B.128) and (B.135) respectively) to define a mapping from $\vec{x}_k$ to $\vec{E}_{ij}$. Where the index $i$ corresponds to the spatial vector dimensions $r$, $\theta$ and $\phi$. The index $j$ corresponds to the grid point and $k$ is the coefficient number. Now I define the Electric field in matrix form:

$$\begin{bmatrix} E_r \\ E_\theta \\ E_\phi \end{bmatrix}_j = - \begin{bmatrix} H_r \\ \frac{1}{r+R_e}H_\theta \\ \frac{1}{(r+R_e)sin(\theta)}H_\phi \end{bmatrix}_{jk} \begin{bmatrix} x_c \\ x_s \end{bmatrix}_k \tag{B.136}$$

or with using full index notation:

$$\mathbf{E}_{ij} = -\mathbf{H}_{ijk}x_k \tag{B.137}$$

From here we may use the above expression as the electric field to define the ion drift at all grid points using equation (B.39).

## B.5 Mapping from Coefficients to Ion Drifts

This section provides the derivation for calculations of implementing EMPIRE

ion drift correction calculations. The goal is to provide an expression for a linear matrix form that maps coefficients to the field-aligns ion drifts.

Beginning with the expression for $\vec{E} \times \vec{B}$ ion drift (Eq. B.39)

$$\delta v_{\perp} = \frac{\delta \vec{E} \times \vec{B}}{B^2} \tag{B.138}$$

Where $\delta \vec{E}$ was previously defined as Eq. (B.137). The next step is to perform the cross product of $\delta \vec{E}$ and $\vec{B}$.

$$\vec{v}_{\perp} = \frac{1}{B^2} \left[ \vec{E} \times \vec{B} \right] \tag{B.139}$$

$$= \frac{1}{B^2} \begin{vmatrix} \hat{r} & \hat{\theta} & \hat{\phi} \\ \delta E_r & \delta E_\theta & \delta E_\phi \\ B_r & B_\theta & 0 \end{vmatrix} \tag{B.140}$$

$$\boxed{\vec{v}_{\perp} = \frac{1}{B^2} \begin{bmatrix} -\delta E_\phi B_\theta \hat{r} \\ \delta E_\phi B_r \hat{\theta} \\ \left( \delta E_r B_\theta - \delta E_\theta B_r \right) \hat{\phi} \end{bmatrix}} \tag{B.141}$$

Where the matrix form for $\delta \vec{E}$ is already defined with mapping matrices $\mathbf{H}_r$, $\mathbf{H}_\theta$ and $\mathbf{H}_\phi$ from sections B.4.1, B.4.2 and B.4.3 respectively. To produce an expression that maps coefficients to ion drifts, I substitute the expression shown as equation (B.137) into (B.141).

$$\vec{v}_{\perp} = \frac{1}{B^2} \begin{bmatrix} -\delta E_\phi B_\theta \hat{r} \\ \delta E_\phi B_r \hat{\theta} \\ \left( \delta E_r B_\theta - \delta E_\theta B_r \right) \hat{\phi} \end{bmatrix} \tag{B.142}$$

$$
\begin{bmatrix} \delta v_{\perp,r} \\ \delta v_{\perp,\theta} \\ \delta v_{\perp,\phi} \end{bmatrix} = \begin{bmatrix} \frac{1}{(r+R_e)sin(\theta)} H_\phi B_\theta \hat{r} \\ -\frac{1}{(r+R_e)sin(\theta)} H_\phi B_r \hat{\theta} \\ \left( -H_r B_\theta + \frac{1}{r+R_e} H_\theta B_r \right) \hat{\phi} \end{bmatrix} \begin{bmatrix} x_c \\ \hline x_s \end{bmatrix} \tag{B.143}
$$

Where now a new set of mapping matrices can be defined as: $\mathbf{F}_r$, $\mathbf{F}_\theta$ and $\mathbf{F}_\phi$ that map the coefficients $\mathbf{x}$ to ion drifts.

$$
\begin{bmatrix} \delta v_{\perp,r} \\ \delta v_{\perp,\theta} \\ \delta v_{\perp,\phi} \end{bmatrix} = \begin{bmatrix} \mathbf{H}_{\vec{v}r}\hat{r} \\ \mathbf{H}_{\vec{v}\theta}\hat{\theta} \\ \mathbf{H}_{\vec{v}\phi}\hat{\phi} \end{bmatrix} \begin{bmatrix} x_c \\ \hline x_s \end{bmatrix} \tag{B.144}
$$

BIBLIOGRAPHY

[1] J. K. Hargreaves, *The Solar-Terrestrial Environment*, vol. 5. 1992.

[2] D. Stern and M. Peredo, *Particle Drifts in Space.* 2007.

[3] D. S. Miladinovich, S. Datta-Barua, G. S. Bust, and J. J. Makela, "Assimilation of thermospheric measurements for ionosphere-thermosphere state estimation," *Radio Science*, vol. 51, no. 12, pp. 1818–1837, 2016.

[4] K. World Data Center for Geomagnetism, "Geomagnetic data service."

[5] S.-r. R. Zhang, P. J. Erickson, J. C. Foster, J. M. Holt, A. J. Coster, J. J. Makela, J. Noto, J. W. Meriwether, B. J. Harding, J. Riccobono, and R. B. Kerr, "Thermospheric poleward wind surge at midlatitudes during great storm intervals," *Geophysical Research Letters*, pp. 5132–5140, 2015.

[6] C. Hively, *Space Foundation Report Reveals Global Space Economy at $329 Billion in 2016.* 2017.

[7] D. Nixon, *International Space Station : architecture beyond earth.* Circa Press, illustrated ed., 2016.

[8] National Science and Technology Council, "National Space Weather Strategy," no. October, 2015.

[9] USA National Science and Technology Council, "National Space Weather Action Plan," no. October, p. 44, 2015.

[10] Y. Su, *Kilometer-Spaced GNSS Array for Ionospheric Irregularity Monitoring.* PhD Thesis, 2017.

[11] C. J. Heinselman and M. J. Nicolls, "A Bayesian approach to electric field and E-region neutral wind estimation with the Poker Flat Advanced Modular Incoherent Scatter Radar," *Radio Science*, vol. 43, no. 5, p. RS5013, 2008.

[12] J. J. Makela, D. J. Fisher, J. W. Meriwether, R. A. Buriti, and A. F. Medeiros, "Near-continual ground-based nighttime observations of thermospheric neutral winds and temperatures over equatorial Brazil from 2009 to 2012," *Journal of Atmospheric and Solar-Terrestrial Physics*, vol. 103, pp. 94–102, Oct. 2013.

[13] G. S. Bust and C. N. Mitchell, "History, current state, and future directions of ionospheric imaging," *Reviews of Geophysics*, vol. 46, no. 1, p. RG1003, 2008.

[14] S. Datta-Barua, G. S. Bust, G. Crowley, and N. Curtis, "Neutral wind estimation from 4-D ionospheric electron density images," *Journal of Geophysical Research*, vol. 114, June 2009.

[15] S. Datta-Barua, G. S. Bust, and G. Crowley, "Deducing storm time F region ionospheric dynamics from 3-D time-varying imaging," *Journal of Geophysical Research*, vol. 116, May 2011.

[16] S. Datta-Barua, G. S. Bust, and G. Crowley, "First storm-time plasma velocity estimates from high-resolution ionospheric data assimilation," *Journal of Geophysical Research: Space Physics*, vol. 118, no. 11, pp. 7458–7471, 2013.

[17] T. Fuller-rowell, "Physical Characteristics and Modeling of Earth ' s Thermosphere," pp. 13–27, 2013.

[18] T. L. Killeen, "Energetics and dynamics of the Earth's thermosphere," *Reviews of Geophysics*, vol. 25, p. 433, Apr. 1987.

[19] H. Rishbeth, "Thermospheric winds and the F-region: A review," *Journal of Atmospheric and Terrestrial Physics*, vol. 34, pp. 1–47, Jan. 1972.

[20] D. P. Drob, J. T. Emmert, J. W. Meriwether, J. J. Makela, E. Doornbos, M. Conde, G. Hernandez, J. Noto, K. a. Zawdie, S. E. McDonald, J. D. Huba, and J. H. Klenzing, "An Update to the Horizontal Wind Model (HWM): The Quiet Time Thermosphere," *Earth and Space Science*, vol. 2, pp. n/a–n/a, July 2015.

[21] M. A. Macleod, "Sporadic E Theory. I. Collision-Geomagnetic Equilibrium," *Journal of the Atmospheric Sciences*, vol. 23, pp. 96–109, Jan. 1966.

[22] T. F. Tascione, *Introduction to the space environment.* Krieger Publishing, 2010.

[23] M. C. Kelley, *The earth's ionosphere : plasma physics and electrodynamics.* Academic Press, 2009.

[24] G. S. Bust and S. Datta-Barua, "Scientific Investigations Using IDA4d and EMPIRE," in *Modeling the Ionosphere-Thermosphere System* (J. D. Huba, R. Schunk, and G. Khazanov, eds.), pp. 283–297, Washington, DC: American Geophysical Union, 2014.

[25] "Definition of ASSIMILATE."

[26] D. R. Weimer, "An improved model of ionospheric electric potentials including substorm perturbations and application to the Geospace Environment Modeling November 24, 1996, event," *Journal of Geophysical Research*, vol. 106, no. A1, p. 407, 2001.

[27] R. E. Kalman, "A New Approach to Linear Filtering and Prediction Problems," *Journal of Basic Engineering*, vol. 82, p. 35, Mar. 1960.

[28] R. G. Brown and P. Y. C. Hwang, *Introduction to random signals and applied Kalman filtering : with MATLAB exercises.* John Wiley, 2012.

[29] G. S. Bust, G. Crowley, T. W. Garner, T. L. Gaussiran II, R. W. Meggs, C. N. Mitchell, P. S. J. Spencer, P. Yin, and B. Zapfe, "Four-dimensional GPS imaging of space weather storms," *Space Weather*, vol. 5, no. 2, p. S02003, 2007.

[30] G. U. G. Kirchengast, "The Graz Ionospheric Flux Tube Simulation Model," in *Solar-Terrestrial Energy Program: Handbook of Ionospheric Models* (R. W. U. S. U. Schunk, ed.), pp. 73–94, 1996.

[31] C. C. Finlay, S. Maus, C. D. Beggan, T. N. Bondar, A. Chambodut, T. A. Chernova, A. Chulliat, V. P. Golovkov, B. Hamilton, M. Hamoudi, R. Holme, G. Hulot, W. Kuang, B. Langlais, V. Lesur, F. J. Lowes, H. Luhr, S. Macmillan, M. Mandea, S. McLean, C. Manoj, M. Menvielle, I. Michaelis, N. Olsen, J. Rauberg, M. Rother, T. J. Sabaka, A. Tangborn, L. Toffner-Clausen, E. Thebault, A. W. P. Thomson, I. Wardinski, Z. Wei, and T. I. Zvereva, "International Geomagnetic Reference Field: The eleventh generation," *Geophysical Journal International*, vol. 183, no. 3, pp. 1216–1230, 2010.

[32] R. Daley and E. Barker, "NAVDAS: Formulation and Diagnostics," *Monthly Weather Review*, vol. 129, pp. 869–883, Apr. 2001.

[33] R. Daley and E. Barker, *NAVDAS Source Book 2000*. Monterey, CA: Naval Research Laboratory, 2000.

[34] A. Gelb, *Applied Optimal Estimation*. Cambridge, MA: MIT Press, 1974.

[35] J. Crassidis and J. Junkins, *Optimal Estimation of Dynamics Systems*. Boca Raton, FL: Chapman and Hall/CRC, 2004.

[36] R. G. Brown and P. Hwang, *Introduction to Random Signals and Applied Kalman Filtering*. New York: John Wiley and Sons, 1997.

[37] R. Daley, *Atmospheric Data Analysis*. Cambridge Atmospheric and Space Science Series, Cambridge University Press, 1993.

[38] S. Datta-Barua, T. Walter, G. S. Bust, and W. Wanner, "Effects of solar cycle 24 activity on WAAS navigation," *Space Weather*, vol. 12, pp. 46–63, Jan. 2014.

[39] S. Datta-Barua, "Ionospheric threats to space-based augmentation system development," in *Proc. ION GNSS 2004*, (Long Beach, California), pp. 21–24, Sept. 2004.

[40] S. Datta-Barua, A. J. Mannucci, T. Walter, and P. Enge, "Altitudinal variation of midlatitude localized TEC enhancement from ground- and space-based measurements," *Space Weather*, vol. 6, Oct. 2008.

[41] S. Datta-Barua, *Ionospheric Threats to the Integrity of Airborne GPS Users*. Doctor of Philosophy, Stanford University, 2008.

[42] A. J. Mannucci, S. Datta-Barua, T. Walter, A. Komjathy, L. Sparks, and B. T. Tsurutani, "Anomalous Nighttime Plasma Structure in the Recovery Phase of a Superstorm," *AGU Fall Meeting Abstracts*, 2005.

[43] "NOAA Space Weather Scales."

[44] J. J. Makela, J. W. Meriwether, A. J. Ridley, M. Ciocca, and M. W. Castellez, "Large-Scale Measurements of Thermospheric Dynamics with a Multisite Fabry-Perot Interferometer Network: Overview of Plans and Results from Midlatitude Measurements," *International Journal of Geophysics*, vol. 2012, pp. 1–10, 2012.

[45] J. J. Makela, B. J. Harding, J. W. Meriwether, R. Mesquita, S. Sanders, A. J. Ridley, M. W. Castellez, M. Ciocca, G. D. Earle, N. a. Frissell, D. L. Hampton, A. J. Gerrard, J. Noto, and C. R. Martinis, "Storm time response of the mid-latitude thermosphere: Observations from a network of Fabry-Perot interferometers," *Journal of Geophysical Research: Space Physics*, vol. 119, pp. n/a–n/a, Aug. 2014.

[46] V. J. Abreu, G. A. Schmitt, P. B. Hays, J. W. Meriwether, C. A. Tepley, and L. L. Cogger, "Atmospheric scattering effects on ground-based measurements of thermospheric winds," *Planetary and Space Science*, vol. 31, pp. 303–310, Mar. 1983.

[47] T. Adachi, M. Yamaoka, M. Yamamoto, Y. Otsuka, H. Liu, C. C. Hsiao, A. B. Chen, and R. R. Hsu, "Midnight latitude-altitude distribution of 630 nm airglow in the Asian sector measured with FORMOSAT-2/ISUAL," *Journal of Geophysical Research: Space Physics*, vol. 115, no. 9, pp. 1–11, 2010.

[48] B. G. Fejer, M. F. Larsen, and D. T. Farley, "Equatorial disturbance dynamo electric fields," *Geophysical Research Letters*, vol. 10, no. 7, pp. 537–540, 1983.

[49] M. Mendillo, "Storms in the ionosphere: Patterns and processes for total electron content," *Reviews of Geophysics*, vol. 44, Nov. 2006.

[50] B. Fejer, "Low latitude storm time ionospheric electrodynamics," *J. Atmos. Solar-Terrestrial Phys.*, vol. 64, no. 12, pp. 1401–1408, 2002.

[51] K. Shiokawa, "Thermospheric wind during a storm-time large-scale traveling ionospheric disturbance," *Journal of Geophysical Research*, vol. 108, no. A12, 2003.

[52] D. L. Carpenter and J. Lemaire, "The Plasmasphere Boundary Layer," *Annales Geophysicae*, vol. 22, pp. 4291–4298, Dec. 2004.

[53] H. Wang, H. Lühr, K. Häusler, and P. Ritter, "Effect of subauroral polarization streams on the thermosphere: A statistical study: STUDY OF SAPS EFFECT ON THERMOSPHERE," *Journal of Geophysical Research: Space Physics*, vol. 116, Mar. 2011.

[54] CORS, "Data."

[55] UNAVCO, "Data."

[56] D. R. Weimer, "Improved ionospheric electrodynamic models and application to calculating joule heating rates," vol. 110.

[57] D. Bilitza, "The International Reference Ionosphere: Rawer's IRI and its status today," *Advances in Radio Science*, vol. 12, pp. 231–236, Nov. 2014.

[58] J. M. Picone, A. E. Hedin, D. P. Drob, and A. C. Aikin, "NRLMSISE-00 empirical model of the atmosphere: Statistical comparisons and scientific issues: TECHNIQUES," *Journal of Geophysical Research: Space Physics*, vol. 107, pp. SIA 15–1–SIA 15–16, Dec. 2002.

[59] A. Ben-Israel and T. N. E. Greville, *Generalized Inverses: Theory and Applications.* New York: Springer-Verlag New York, 2 ed., 2003.